Dissertation

submitted to the
Combined Faculties for the Natural Sciences and for Mathematics
of the Ruperto-Carola University of Heidelberg, Germany
for the degree of

Doctor of Natural Sciences

presented by

M.Sc.
Markus Janson

born in Sävedalen, Sweden

Oral examination: April 30, 2008

Direct imaging searches for substellar companions to nearby stars

Referees: Prof. Dr. Thomas Henning

Prof. Dr. Joachim Wambsganss

Abstract

Ever since the first detections of extrasolar planet candidates in the early 1990s, our knowledge of such objects has drastically increased, and exoplanet science today constitutes a major branch of astrophysics, with a few hundred individual detections. Our physical understanding is however limited by the fact that the planets are generally only detected indirectly, with just a few constraints on its orbital and physical parameters. Direct imaging of exoplanets, where the planet can be spatially resolved from the star, opens up for a much broader understanding of these objects, with the opportunity to study their spectral characteristics. Alternatively, eclipse spectroscopy, where the planetary signal can be temporally resolved in systems where the orbital plane of the planet happens to align with the line of sight of an observer, can be used for the same purpose. In this thesis, we study various approaches for direct imaging and spectroscopy of exoplanets from the ground, using combinations of adaptive optics and differential methods, in particular spectral and angular differential imaging. The possibility of using an external occulter for the purpose of decreasing the star-planet contrast is studied. We also investigate the possibility to calibrate theoretical mass-luminosity relationships in order to improve detection predictions and the interpretations of null-detection surveys. Scientific results include an improved age range of the AB Dor system thanks to the spatial distinguishing of AB Dor B as a close binary, and the best constrained upper limit to the H-band brightness of any known exoplanet ever achieved, from a deep imaging search for ϵ Eri b.

Zusammenfassung

Ausgehend von den ersten Entdeckungen von Kandidaten für extrasolare Planeten zu Beginn der 1990er Jahre wuchs unser Wissen über derartige Objekte rasant an. Mit mehreren 100 bekannten Exoplaneten stellt ihre Untersuchung heute einen Hauptzweig der Astrophysik dar. Allerdings beschränkt der im allgemeinen indirekte Nachweis der Exoplaneten unser Wissen über Umlaufbahnen und physikalische Eigenschaften. Erst die direkte Abbildung der Exoplaneten, d.h. die räumliche aufgelöste Trennung von Stern und Exoplanet ermöglicht eine umfassendere Untersuchung ihrer spektralen Eigenschaften. Eine weitere Möglichkeit ist Bedeckungsspektroskopie. Hierbei wird in Systemen, in denen die Sichtlinie des Beobachters in der Umlaufebene des Planeten liegt, das Planetensignal zeitlich aufgelöst. In der vorliegenden Doktorarbeit werden unterschiedliche Ansätze zur direkten Abbildung und Spektroskopie der Exoplaneten vom Erdboden aus unter Verwendung von adaptiver Optik und differentiellen Methoden, die auf spektralen Eigenschaften oder Drehungen beruhen, untersucht. Es wird die Machbarkeit eines externen, freifliegenden Bedeckers mit dem Ziel, den Kontrast zwischen Planet und Stern zu minimieren, studiert. Weiterhin wird mit dem Ziel, Vorhersagen zur Entdeckung von Exoplaneten und die Interpretation von Nullergebnissen in breitangelegenten Suchprogrammen zu verbesseren untersucht, wie sich theoretische Masse-Leuchtkraft-Beziehungen eichen lassen. Zu den wissenschaftlichen Ergebnissen zählen eine verbesserte Altersbestimmung des AB Dor-Systems, aufbauend auf den Eigenschaften des engen visuellen Doppelsterns AB Dor B, und im Rahmen von tiefen Aufnahmen die beste bisher erreichte Obergrenze für die H-Bandhelligkeit eines bekannten Exoplaneten im Falle von Eps Eri b.

PREFACE

This thesis work was performed at the Max-Planck-Institut für Astronomie in the period between August 2005 and early 2008 under the supervision of Dr. Wolfgang Brandner and Prof. Dr. Thomas Henning. The main content of the thesis has been published in five peer-reviewed journals. An article reference is given in the beginning of each chapter, showing which article the chapter corresponds to. One chapter, 'A double-differential scheme for spectroscopy of transiting planets from the ground', is based on as-of-yet unpublished research. The research of that chapter was performed in collaboration with Mark Swain (JPL, Pasadena), Christina Afonso and Thomas Henning (MPIA, Heidelberg), and Daniel Angerhausen, Christof Iserlohe and Alfred Krabbe (Univ. of Cologne).

Acknowledgements

I am particularly grateful to my thesis supervisors, Wolfgang Brandner and Thomas Henning, for their help and the useful discussions. During my PhD work, I have received financial support via IMPRS Heidelberg, for which I am naturally also very thankful. Kudos to Christian Fendt for a job well done in administrating this program.

Several free online services exist that hugely simplify life for an astrophysicist. I have made extensive use of VIZIER, SIMBAD, NASA ADS, and obviously the Extrasolar planets encyclopedia as part of my scientific work. Astronomical catalogues such as 2MASS and Hipparcos have been particularly useful for my purposes.

Thanks to the computer department at MPIA for keeping a system up that hardly crashed at all during my whole time at the institute – a feat far from accomplished at previous workplaces I've encountered. General thanks also to all the administrative and servicing personnel at MPIA, as well as Paranal and Calar Alto, for keeping things running without noticeable problems.

To all collaborators I've had during my PhD studies, and my colleagues at MPIA for the interesting scientific discussions – many thanks. The positive and creative spirit of the workplace, and the scientific environment in general, is a joy to experience. I wish I could list you all individually, but it would make a long list, and inevitably I would forget someone. A specific sentence of thanks, however, is well spent indeed on the other members of Wolfgang's research group – Felix, Mica, Boyke, Kerstin, and Sebastian. Thanks also to the people I have already thanked in the acknowledgments of my individual articles for various reasons,

but have so far not been specifically mentioned here – Ben Zuckerman, Stan Metchev, Andrea Stolte, Alessandro Berton, Webster Cash, Stefan Hippler, and all the anonymous referees.

Thanks to Anders Johansen for the thesis macro – if you, the reader, find the general structure of this thesis to be aesthetically pleasing, the cred goes his way. Whenever I've had questions about everyday problems with tax returns, insurance issues, or Linux shortcuts, my office mates have always been eager to help. Many thanks to Michael, Marie-Helene, Jan, and Sebastian for that.

Finally, great thanks to my family and friends for all the obvious reasons.

CONTENTS

INTRODUCTION

The easiest way to detect an Earth-like planet is to look downwards. Finding a few other planets is also easy enough, as Mars, Venus, Jupiter and Saturn are all readily visible in the night sky, even when competing with the glow of city lights. In fact, all planets (that are still planets) were detectable with 17th century technology (although Neptune was not identified as a planet until 1846). However, the step from observing our own planets to observing planets in other solar systems is abysmal. The most nearby extrasolar planet must be at least on the order of 10^5 times farther away from us than Mars is, and separated by at most a few arcseconds from a much brighter star. If, furthermore, we should wish to detect a sizable amount of Earth-like planets in the habitable zone of solar-type stars, we would have to go out to a distance of at least 10 pc, meaning we have to provide a dynamic range of 10^{10} (at visible wavelengths) at an angular separation of only 100 mas! While achieving such a goal takes significant investment in terms of hard work and money, it is essential for understanding our place in the universe.

High-contrast imaging instruments and methods are presently at a stage where thermal emission of giant exoplanets should be detectable in favourable cases. Two main aspects determine the merit of a circumstellar system for planet detection purposes. One is, obviously, the proximity of the star. The closer the system, the larger the angular separation corresponding to a given physical separation, and the more photons are received from a planet of a given brightness. The other aspect is youth of the system. The reason for this is that the brightness contrast between the star and planet is smallest at young ages. Over time, the planet cools down from its initial contraction, whereas the star burns hydrogen and maintains an approximately constant brightness. Unfortunately, the number of targets that are both very young and very nearby is very small.

For achieving a sufficient PSF stability and spatial resolution from the ground, it is necessary to use adaptive optics. This is a real-time correction of wavefront distortions imposed by the atmosphere, by means of a deformable mirror that counteracts measured deviations from an expected (flat) wavefront. To reach the contrasts necessary, it is also required to use differential imaging as a means of highlighting features that occur in the planet but not the star, or vice versa. The difference can be one of spectral energy distribution, polarization, rotation symmetry, temporal evolution, or a combination of these, as well as possibly other features. Differential methods are efficient at reducing residual PSF errors from non-perfect wavefront correction – so called speckle noise, a spatially correlated noise that is otherwise difficult to distinguish from physical companions.

Since we haven't detected any young planets similar to those in our own system, and since no young planetary mass objects with dynamically determined masses are known altogether, our limits for what we can expect to detect have to rely entirely on theoretical mass-luminosity models. These models are poorly calibrated, and at young ages, a substellar object still 'remembers' its initial conditions, making such models highly uncertain. In order to make better predictions, and in order to better understand the physics of the planets that will eventually be detected, it is necessary to calibrate the models with solid calibration points where both the mass, brightness and age can be well determined.

In this thesis, we approach these issues from different angles. A short outline of the thesis is as follows:

In Chap. 1, we give a brief summary of exoplanets, in terms of their formation, and methods to detect and characterize them. Chap. 2 deals with a low-mass companion to the young T Tauri star GQ Lup, presenting an a posteriori analysis of first-generation AO data for the object, thus demonstrating the difficulties related to speckle noise, as well as discussing the characteristics of the companion. Chap. 3 represents an attempt to calibrate theoretical models by use of the highly interesting AB Dor system, particularly by taking advantage of the detected binarity of AB Dor B. In Chap. 4, the highest contrast images within an arcsecond ever taken are presented, acquired during the search for the most nearby known exoplanet, ϵ Eri b. The SDI and ADI techniques are described, and various tests are performed to explore these methods. Chap. 5 details a comparison of SDI at two different types of instruments, one simultaneous imager and one integral field spectrograph. In Chap. 6, the possibility of combining ground-based imaging with a space-based occulter is examined. In Chap. 7 we discuss how a spectral- and time-differential approach can be applied to overcome atmospheric limitations to eclipse spectroscopy from the ground, and finally, in Chap. 8 we summarize the results and outline future work to be done in this area.

Chapter 1

Extrasolar planets

1.1 Planet formation

Conventionally, there have been mainly two theories of giant planet formation discussed in the moderately recent scientific literature – core accretion (e.g. Pollack et al. 1996; Bodenheimer et al. 2000), and disc instability (e.g. Boss 1998). Essentially, they correspond to a bottom-up versus top-down formation scenario. The core accretion scenario starts from the bottom, with small dust grains in a protoplanetary disk sticking together, accumulating into increasingly larger structures, eventually becoming gravitationally interacting planetesimals that can continue to grow through inelastic collisions. In this way, planets of the same order of mass as the Earth can form close to the star, whereas beyond the ice-line, where water is frozen out and increases the surface density of solids, objects can continue to grow even further. Once a critical mass of $\sim 10\ M_{\mathrm{Earth}}$ is reached, runaway gas accretion occurs, leading to a rapid increase of mass, thus creating giant planets. The disc instability scenario starts from the top – the gaseous protoplanetary disk simply cools until it fragments and collapses, creating giant gas planets.

While the debate on which of these scenarios is the general source of giant planets does not appear to have entirely settled, a growing amount of evidence points to core accretion as being the dominant process. One of the reasons for this is the fact that theoretical work has shown it to be virtually impossible for the disc to cool sufficiently fast to fragment within at least 10 AU (see e.g. Rafikov 2005). From the observational side, the observed correlation between massive planet occurrence and host star metallicity (see Fischer & Valenti 2005) is a strong piece of evidence for core accretion, as it follows naturally from that planets can grow bigger faster if a larger mass of solids is present in the disk, whereas there is no reason to expect such a correlation for disc instability. Meanwhile, the main traditional problems of core accretion have been solved theoretically. In particular, the timescale of core accretion formation was long considered a problem, since a static core at some separation in the protoplanetary disk will deplete the material close to its own orbit, leading to a very slow growth, and hence a formation timescale longer than the ~5-10 Myr in which the disk is known to dissipate (see e.g. Haisch et al. 2003). However, the inclusion of semi-major axis migration of the core in the disk (see e.g. Alibert et al. 2005) allows it to accumulate mass over a much larger range of separations, thereby avoiding depletion, which in turn allows planet formation in a few Myrs.

Perhaps most importantly, core accretion can be used for population synthesis, i.e. simulations of the end products of core accretion formation, wherein the resulting distributions in, e.g., mass and semi-major axis can be matched with the observed planetary population (see e.g. Ida & Lin, 2008). Since agreement is reached for the presently observable parameter space, and since specific predictions can be made for future observations, this speaks greatly in favour for the core accretion scenario.

1.2 Brown dwarf formation

Brown dwarfs cannot form in a traditional star formation framework, because their masses are too far below the Jeans mass in molecular clouds, which is the classical limit for when a cloud can become gravitationally unstable and collapse, eventually forming a stellar-type object. Yet, they exist, and constitute a smooth continuation of the initial mass function (IMF) towards low stellar masses, indicating a similar formation mechanism.

Several different scenarios have been suggested to explain the existence of brown dwarfs. Two that receive particular attention are formation by turbulent fragmentation (e.g. Padoan & Nordlund 2004), and formation by embryo ejection (e.g. Reipurth 2000). In the former case, turbulence in a molecular cloud causes strong density contrasts, with local over-densities that can collapse to form a compact object. In this sense, brown dwarfs are simply the low-mass tail of regular star formation. In the latter case, an object with stellar mass starts to form in a cluster of forming objects, but the protostellar core is ejected through dynamical interactions before it can accrete its circumstellar material. Hence, in this case, brown dwarfs are 'would-be' stars whose growth were restricted halfway through formation.

Each of the scenarios have had arguments put forth for and against them in the recent literature. For instance, Thies & Kroupa (2007) argue that the binary distribution of brown dwarfs is very different from stars, in terms of mass ratio and semi-major axes distribution, and also that taking this into account, a small discontinuity can be traced in the IMF around the star/brown dwarf border. This would speak in favour of embryo ejection relative to turbulent fragmentation, in which the IMF should be expected to be continuous. On the other hand, the presence of large disks around brown dwarfs (e.g. Scholz et al. 2006), and continuity in disk fraction (e.g. Caballero et al. 2007) from the stellar to the brown dwarf regime implies a star-like formation (thus favouring turbulent fragmentation), particularly because large disks are generally not expected to survive in an ejection scenario (in difference from small disks, e.g. Umbreit et al. 2005). Perhaps more importantly, the fact that a non-negligible number of young wide binary brown dwarfs exist (e.g. Close et al. 2007) is very difficult to explain in an ejection scenario, because such a constellation should be ripped apart during the event. In the end, neither of the mechanisms can be excluded as a dominant contributor to the population of brown dwarfs, based on the present data. It can therefore not be ruled out that both contribute significantly.

1.3 Planet and brown dwarf definitions

The exact definition of planets is a difficult and controversial issue. A recent manifestation of this that received much attention was the re-classification of Pluto from planet to dwarf planet following a vote at the IAU general assembly of 2006 in Prague, which enforced a formal definitional difference between planets and smaller objects in the solar system. By this new definition, a planet not only has to be massive enough to attain hydrostatic equilibrium, but also needs to be dominant enough to clear its own orbit, a condition which Pluto fails to fulfill. This issue, however, concerns the lower limit on what constitutes a planet, which is so far not a concern in the context of exoplanets – nor, by extension, of this thesis. In our case, the limit of interest is the *upper* limit of what constitutes a planet, in contrast to what constitutes a brown dwarf.

The present IAU definition of a planet at the upper limit (which is wisely recognized as being entirely preliminary; see e.g. the statement of the IAU WGESP at `http://www.dtm.ciw.edu/boss/definition.html`), is an object with a mass less than 13 $M_{\rm jup}$ in orbit around a star. If the object instead has a mass above this limit, then by this definition, it is a brown dwarf. The formal reason for this limit is that it corresponds to the mass required for the object to burn deuterium in its core. As argued in e.g. Chabrier et al. (2007), this limit is physically arbitrary, because whether an object burns deuterium or not has virtually no impact on its physical properties or evolution over time (with the exception of a short-lived deuterium 'main-sequence' phase). By contrast, hydrogen burning versus a lack thereof has fundamental implications for the evolution of a (sub-)stellar object, hence the definitional difference between brown dwarfs and stars is physically sound. As we have seen in previous sections, planets as (e.g.) those in our solar system and brown dwarfs as seen in the field obviously formed by different mechanisms. If all objects that formed like Jupiter were neatly below 13 $M_{\rm jup}$ in mass, and all objects that formed like, e.g., GJ 229 B (Oppenheimer et al. 1995) were likewise above this limit, the physical basis for setting this limit would be a moot point. Unfortunately, this is not the case. Observations of young stellar clusters have shown that the brown dwarf mass function continues well below the deuterium burning limit (see e.g. Caballero et al. 2007; note, however, that this conclusion depends on rather uncertain evolutionary mass-luminosity models). Likewise, the mass distribution of detected exoplanets (see Fig. 1.1) indicates that planets above said limit should be able to form, if only in very rare cases around solar-type stars (but possibly more frequently in massive systems, see e.g. Kennedy & Kenyon, 2008).

Hence, there is very likely a significant mass overlap for the different formation mechanisms around 13 $M_{\rm jup}$. Consequently, depending on whether the definition of a planet is based on mass or on formation, different objects will be classified as planets (see Fig. 1.2). It is hardly controversial to claim, based on the discussion performed so far, that a definition based on formation would be more physically relevant that a definition based on mass. A common objection to the former definition is that the formation scenario of an already formed object is difficult to determine. There are several comments that can be made in this regard. Firstly, we note that it turns out that mass is also very difficult to determine for many of these objects. For objects that are unbound to a system, or reside at large separations (∼100 AU), no dynamical mass can be determined within a reasonable time-frame. Instead, a mass must

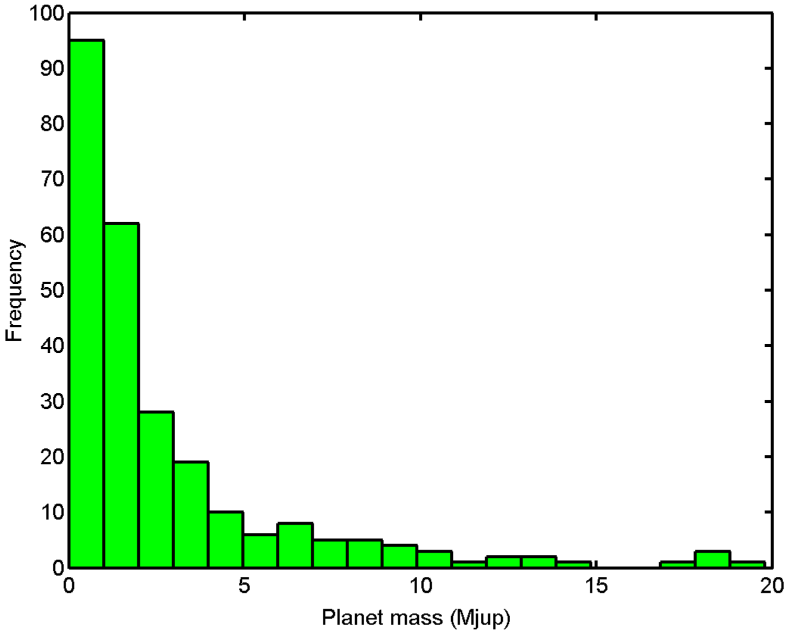

Fig. 1.1: Mass histogram (projected masses) for planet candidates detected by radial velocity from Schneider (2008).

be inferred using insufficiently calibrated evolutionary or spectral models, leading to very large uncertainties. In fact, one might claim that for a lot of the limit-case systems discovered so far, it is easier to observationally constrain their formation scenario than their mass, to the extent that they can be classified. Objects such as 2M1207 B, SCR 1845 B, and GQ Lup B represent a group of objects in the mass range of high-mass planets or low-mass brown dwarfs (~5-50 $M_{\rm jup}$), in systems with relatively large separations ($\sim 10-100$ AU) where the mass is difficult to determine. For instance, the best current estimates for the mass of GQ Lup B is 10-40 $M_{\rm jup}$ (McElwain et al. 2007, Seifahrt et al. 2007), hence both non-deuterium burning and deuterium burning masses are within the uncertainties. On the other hand, it seems quite clear that objects of this type, irrespective of their exact formation mechanism, did not form in the same way as the planets of our own solar system, at the very least not by core accretion. The most clear example of this is 2M1207 B, which is most likely a non-deuterium burning object (most recent mass estimate is 8 ± 2 $M_{\rm jup}$, Mohanty et al. 2007), but where the primary is a brown dwarf with mass 24 ± 6 $M_{\rm jup}$, giving a secondary-to-primary mass ratio of 0.3, which is orders of magnitude larger than for giant planets in general, and the separation is 50 AU. Both observations (e.g. Butler et al. 2006b) and theory (e.g. Kennedy & Kenyon 2008) indicate that gas giants are increasingly rare around lower-mass primaries. Meanwhile, there are brown dwarf binaries with similar properties (e.g. Jayawardhana et al. 2006).

A common suggestion that attempts to take both formation and mass into account is to refer to all objects below 13 $M_{\rm jup}$ as planetary mass objects, or planemos for short, whereas planemos that formed by core accretion are called planets. We note that this is a problematic definition, in that planets may well exceed 13 $M_{\rm jup}$ as mentioned earlier, leading to the paradoxical situation of planets that do not have planetary mass.

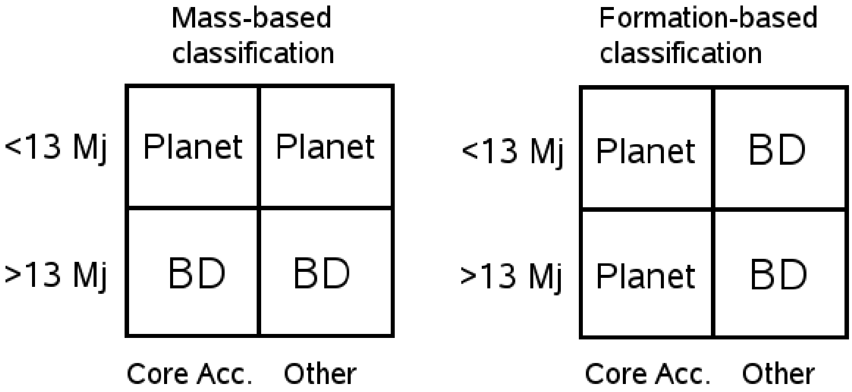

Fig. 1.2: Two different schemes for how to classify planets and brown dwarfs. Controversy arises where different formation mechanisms overlap in mass.

In any case, while we have argued here that formation would be a more reasonable basis for definition than mass, we will generally use terms such as 'planetary mass' to denote masses below 13 $M_{\rm jup}$, since this is more or less the convention at present.

1.4 Planet detection

The question of whether other worlds exist beyond our own has caught the attention of mankind since at least ancient times, discussed as it was by the likes of Plato and Aristotle. Since the birth of 'modern' astronomy in the 16th century, with the dawning understanding of the concept of our world as a planet among others, revolving around a star among others (e.g. Bruno 1584), we have been able to formulate this as a falsifiable question – i.e., ‘do planets exist around other stars? ’. However, due to the extreme contrast in both brightness and mass between stars and planets, it took the whole technological development of the 20th century to finally start detecting them, thus providing a means of actually addressing the question. Planet detections are now being made on several fronts, each with increasing accuracy as time goes on. In the following, we will describe some of the most successful or promising methods to detect extrasolar planets, and what we can learn from each method. Some methods are closely related in terms of their principle, we have clustered these into the groups 'Dynamical methods', 'Eclipse methods' and 'Imaging methods'. Other methods, such as the successful gravitational microlensing approach, which are very distinguished from all other methods in some sense, are grouped as 'Other methods'.

1.4.1 Dynamical methods

In this section, we describe the indirect detection of planets from their dynamical influence on a parent star or stellar remnant. Observable influence from the planet on a circumstellar disks are technically also dynamical, but since the principle is different in that case, we place it under 'Other methods' in Sect. 1.4.4.

Two bodies in a Keplerian system exhibit orbital motion around their common center of mass. For a star-planet system, the high mass contrast leads to that the center of mass is much closer to the star than to the planet – generally, even well inside of the stellar radius. Hence, the orbital motion of the star is obviously much smaller than that of the planet – but nonetheless, the motion is there, and is occasionally (and increasingly often) measurable with present high-precision instruments.

Radial velocity

The radial velocity (RV) signal of a star corresponds to its motion along the observer's line of sight. This is measured through the Doppler shift of the spectral lines of the star relative to spectral lines from a light source that is static with respect to the observer. If the star has a planet, it will exhibit a periodic Doppler shift with the same period P as the planetary orbit, and a velocity amplitude K, which under the assumption of $M_\star >> M_\mathrm{p}$ given by:

$$K = \left(\frac{2\pi G}{P}\right)^{1/3} \frac{M_\mathrm{p} \sin i}{M_\star^{2/3}} \frac{1}{(1-e^2)^{1/2}} \tag{1.1}$$

where $M_\star$ is the mass of the star and M_p the mass of the planet. Thus, by estimating $M_\star$ from stellar models along with the observed periodicity P and eccentricity e from the shape of the RV curve, we can determine a and $M_\mathrm{p} \sin i$. The shape of the curve also gives us some additional orbital parameters – argument of periapsis ω, and time of periastron t_p. The uncertainty factor $\sin i$ arises from the fact that we can't know which fraction of the stellar motion is hidden in the plane perpendicular to the line of sight from radial velocity measurements alone. If the orbital plane is seen exactly edge-on, then $\sin i = 1$ such that the projected mass that we measure is exactly equal to the real mass. However, if $\sin i < 1$, then M_p must obviously be larger. Hence, radial velocity alone can only give us a lower limit for the mass of the companion. This may intuitively seem like a very serious limitation. For instance, if a low-mass star orbits the primary at an inclination very close to face-on, it can be interpreted as a planetary companion close to edge-on. However, such an event is very unlikely. Under the reasonable assumption that orbital orientations are random, the most probable observable inclination is edge-on, and the average inclination is 30°, hence for a sample of RV planets with an average projected mass of 1.0 M_jup, the real average mass is 1.15 M_jup. The probability that a planet with $M_\mathrm{p} \sin i = 1\ M_\mathrm{jup}$ has $M_\mathrm{p} \geq 10\ M_\mathrm{jup}$ is only 0.5 %.

The RV technique has the advantage of being very weakly dependent on distance – the planetary signature is entirely independent of this factor, the only impact of distance is the decreasing apparent brightness of the host star, leading to a lower SNR for the spectra. It is strongly biased to small orbits, and large masses, hence why 'hot Jupiters' are so easily detected with this method. It has a preferred spectral type range around F, G and K. Later-type stars are often too faint to get adequate SNR in the spectra, though this can be mitigated by using larger telescopes or NIR wavelengths. A more serious limitation is reached for earlier-type stars, which are much more active (thus broadening the spectral lines, decreasing the line positioning accuracy), and have much fewer spectral lines, making high-precision RV

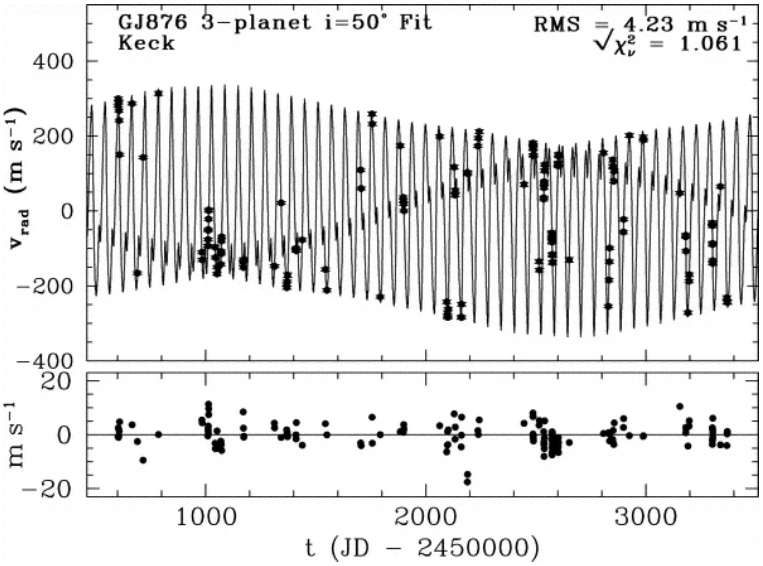

Fig. 1.3: A radial velocity curve with a 3-planet fit for the system GJ 876 (see Rivera et al. 2005). The smallest planet candidate has a projected mass of about 5.9 M_{Earth}, dynamical arguments for the inclination of the system point to an actual mass of about 7.5 M_{Earth}.

impossible. The decreased RV sensitivity around active stars also impacts the sensitivity for young stars of all spectral types. In terms of the number of planet candidates detected, RV is by far the most successful method so far, with about 85 % of the primary detections, and 95 % including follow-up detections, at the time of writing.

The first generally acknowledged planet candidate around a main-sequence star was detected around 51 Peg using RV by Mayor & Queloz (1995). Most of the large surveys have traditionally targeted non-active main-sequence solar-type stars (e.g. Tinney et al. 2001; Queloz et al. 2000b), but efforts have also been made to survey M-stars (e.g. Bonfils et al. 2007), giant stars (e.g. Reffert et al. 2006a) and young stars (Setiawan et al. 2008). The most precise instrument existing to date is HARPS (used on the ESO 3.6 m telescope at La Silla), which has a precision well below 1 m/s, allowing for the detection of planets below Neptune mass. The lowest (projected) mass planet detected so far is Gl 581 c, with about 5 M_{Earth} (Udry et al. 2007).

Astrometry

Planet search by astrometry is based on the same physical principle as radial velocity, but whereas planet searching with RV concerns the stellar motion along the line of sight, astrometry concerns the motion in the image plane. The astrometric signature is quantified by the angular semi-major axis $\alpha_\star$, which (for small angles) relates to the actual semi-major axis $a_\star$ as:

$$\alpha_\star = \frac{M_{\mathrm{p}}}{M_\star} \frac{a}{d} \tag{1.2}$$

where d is the distance to the star. With a sufficient amount of astrometric data points with adequate accuracy, all orbital parameters can be uniquely determined, meaning that with a known d and an estimated $M_\star$, the unique mass M_p can be determined. Hence qualitatively, astrometry gives more information about a detected target than does RV. However, is also offers more challenges. The star's own motion, which is observed as proper motion on the sky, as well as the parallactic effect imposed on an Earth-bound observer both must be disentangled from a planetary orbit, and the effect of multiple planets is harder to separate than in the RV case. Furthermore, the dependence on distance limits the possible sample to relatively nearby stars. Still, the method shows great promise for future exoplanetary research. For an arbitrary target, astrometry is in general the only known way of determining a unique mass (exceptions are transiting planets and planets detected in transient microlensing events). Furthermore, the astrometric signature increases with increasing semi-major axis, leading to an opposite bias compared to RV, thus complementing it very well.

Detection of the astrometric signature of an exoplanet has so far only been achieved in a few cases (Gl 876 b, Benedict et al. 2002; ϵ Eri b, Benedict et al. 2006) using HST. However, this situation will change drastically in the coming years, as astrometric instruments with microarcsecond precision come online. Interferometry makes it possible to achieve such precision from the ground, which will be taken advantage of with PRIMA at the VLT (e.g. Reffert et al. 2006b), coming online in 2009. The GAIA mission (e.g. Perryman et al. 2001), which will revolutionize many aspects of intragalactic astronomy, will also make a huge contribution with thousands of giant planets over a time-line of the mission (2012-2017). The most exciting mission, however, is SIM Planetquest (e.g. Unwin et al., PASP submitted), with an expected sensitivity even down to Earth-like masses in a few cases. At present, however, the funding situation of the project is unclear.

Timing of regular events

Since light travels at a constant velocity, the difference in time from when a photon is emitted from a light source to when it is registered by an observer depends uniquely on the distance it travels. Unfortunately, we don't know when a given photon was emitted, otherwise we could measure the distance and all its time derivatives to the emitting source with an extreme precision. However, some objects in space are known to emit light with a very regular variability. In these cases, changes in the observed temporal behaviour of the variability will correspond to accelerations of the source. Thus, if a Keplerian-type periodicity can be seen in the characteristic time of an intrinsically regular variable event, it must be due to a physical companion.

The most famous example of this is pulsars. A pulsar emits primarily radio emission in a very narrow light-cone that follows the extremely rapid rotation of the central neutron star. This gives rise to a lighthouse-equivalent pulse effect for an observer that happens to be appropriately aligned. Since only the radial motion of the pulsar can be monitored, only a projected mass can be measured, as in the case of RV. The first planet candidate detections altogether, with the smallest probable masses known even to date (2.4 and 3.4 M_Earth) were made through timing of the millisecond pulsar PSR 1257+12 (Wolszczan & Frail, 1992).

The same type of principle, but on a very different type of object, has also been applied to infer the presence of a giant planet candidate around V 391 Peg (see Silvotti et al. 2007). V 391 Peg is a hot subdwarf which exhibits seismic pulsations, leading to a very regularly periodic variability. Thus, in exactly the same way as described above, a planet signature could be detected. Note that while all stellar objects pulsate seismically to some degree, only white dwarfs and hot subdwarfs have a sufficiently regular pulsation pattern for the method to work.

1.4.2 Eclipse methods

All methods that build on the principle of comparing a stellar signal during a phase when a planet passes in front of or behind the parent star, with the signal from the same star at some other phase, are classified as 'Eclipse methods' here. Eclipses provide a unique opportunity in that they represent an almost discrete change of observable state for the planet, a 'jump' which is often relatively easy to detect, and which allows for very precise relative on/off measurements. For obvious geometrical reasons, a vast minority of planets will exhibit a transit as seen from Earth – the orbit must be very close to edge-on. This is a fundamental limit for this group of methods. Nonetheless, eclipse methods are likely to dominate the field of exoplanet research for several years to come, for reasons detailed in the following.

Transit

A transit is simply the event in which a planet happens to pass in between its parent star and an observer. This results in a dip of the lightcurve, with a fractional maximum depth δ simply given by $(R_{\mathrm{p}}/R_{\star})^2$ where R_{p} is the radius of the planet, and $R_{\star}$ is the radius of the star. In other words, by estimating $R_{\star}$, R_{p} follows directly. The periodicity of the recurring event gives P (and a if $M_{\star}$ is estimated), and the shape of the lightcurve depends on i (which, by definition, is close to 90^{o} since the transit occurs in the first place). However, detection of a periodic dip with a depth corresponding to a planetary radius is not sufficient to claim detection of a planet. The surveys done so far (see e.g. Konacki et al. 2003) have shown that a majority of periodic dips in this range are false alarms. Examples of events that can mimic a planetary transit are the eclipse of a very low-mass star, and the eclipse of a background binary, blended into the same PSF by the limited resolution of the telescope. In order to separate planetary transits from false alarms, it is generally necessary to perform follow-up observations with other methods. Fortunately, radial velocity often provides an excellent opportunity to do this, because the two methods share a bias to small orbits, such that planets that are easily detected by transits are often easy to detect also with radial velocity. In the cases of a genuine detection, the combination of transit and RV data gives a unique mass (because the inclination is given by the transit), and a unique radius. From this, the density can be determined.

Even more interestingly, transiting planets allow for transmission spectroscopy of the planet atmosphere. By comparing spectra between transit and non-transit of the planet, spectral features of the planet itself can be deduced, given enough precision. This has been done for the first transiting planet detected (HD 209458, see Charbonneau et al. 2000), see e.g.

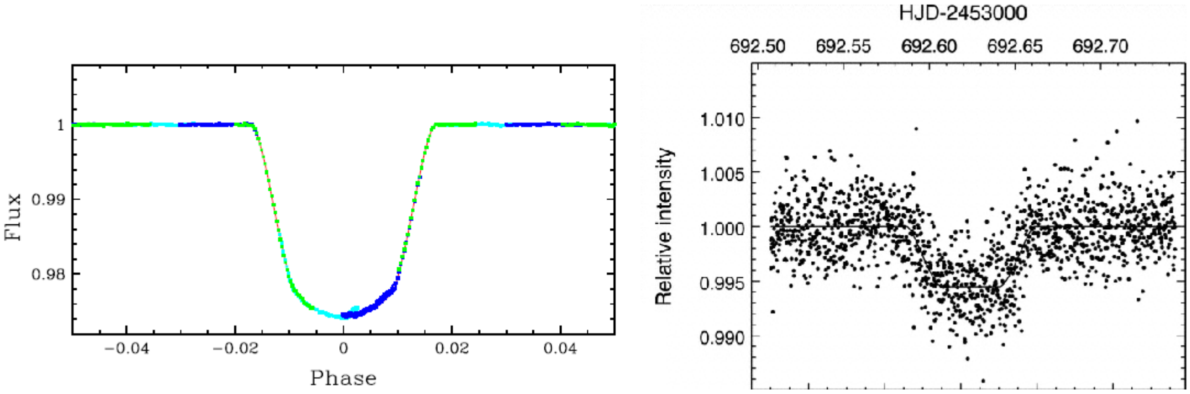

Fig. 1.4: Lightcurves for the transit and secondary eclipse of HD 189733. Right: HST coverage of the transit, yielding exquisite precision (Pont et al. 2007). Left: Spitzer coverage of the secondary eclipse, note the much smaller eclipse depth in this case (see Deming et al. 2006).

Charbonneau (2002) and Vidal-Madjar et al. (2003).

Already, the transit method is the second most successful in terms of pure numbers of candidate detections. With the COROT mission (e.g. Borde et al. 2003) already launched, and the Kepler mission (e.g. Basri et al. 2005) to follow, the number will rise drastically over the coming years, and become comparable to that of RV. Both missions are transit missions, with the projected capacity to detect small planets – 2-3 R_{Earth} in the case of COROT, even down to 1 R_{Earth} in the case of Kepler.

Secondary eclipse

The thermal brightness of a planet is very small compared to the star. For an Earth-equivalent planet, the infrared brightness ratio is on the order of 1:10^7. For a typical hot Jupiter, the ratio is on the order of 1:10^4. While this is certainly still a very significant ratio, it is detectable with present instrumentation under certain circumstances. In particular, it can be detected with the use of secondary eclipses.

A transiting hot Jupiter which is spatially unresolved from its primary normally provides a tiny excess to the infrared brightness. When the planet passes behind the star, the excess disappears. Hence, this event provides the observer with a reference point that (s)he normally would not have – the true brightness of the star without the contribution of the planet. The excess flux F_{p} is the flux of the planet, which under the assumption of blackbody radiation is governed by:

$$F_{\mathrm{p}} = 4\pi R_{\mathrm{p}}^2 \sigma T_{\mathrm{p}}^4 \tag{1.3}$$

Since the planetary radius R_{p} can be determined from the transit depth, this immediately gives the effective temperature T_{p}. The secondary eclipse also gives the opportunity to do infrared spectroscopy of the planet by comparing on/off spectral distributions. So far Spitzer has been the dominating telescope in the field of secondary eclipses, with the first detections of secondary eclipses (e.g. Charbonneau et al. 2005), and constraints on the spectral energy distribution of planets with broad-band photometry (Tinetti et al. 2007) and low-SNR spectroscopy (Richardson et al. 2007, Grillmair et al. 2007, Swain et al. 2008). The JWST, once it is launched, will be able to make great progress in this field.

Rossiter-McLaughlin effect

The simplest example of the Rossiter-McLaughlin effect is when a planet transits a star in the same plane as the stellar rotation, with the same orientation (this is normally expected for exoplanets, unless they have been dynamically redistributed from their natal orbital plane). The stellar rotation causes a differential tangential velocity distribution over the surface, as seen by an observer. The part of the surface that moves towards the observer is blueshifted, and the part that moves away is redshifted. Normally, the stellar surface is not resolved with present-day telescopes, and hence the rotation just leads to a Doppler broadening of the spectral lines. However, as a planet transits across the disk, it blocks out different parts of the stellar light. In the beginning of the transit, preferentially blueshifted light is blocked out, and in the end, the same is true for redshifted light. Hence there is a net redshift in the stellar lines during the first half of the transit and vice versa. Varying the angle between the stellar rotation and the planetary orbital plane and/or the impact parameter gives different observed results, because different fractions of the red- and blueshifted parts of the stellar surface are covered during the event. Hence, these parameters can be constrained in this manner.

The Rossiter-McLaughlin effect has been observed in a few cases (e.g. Queloz et al. 2000a, Narita et al. 2007). It is not well suited for primary detections due to its transient nature combined with its demand for high spectral resolution. However, while the amplitude of the effect is mostly smaller than the RV amplitude for Jupiter-like planets, it can start to dominate towards Earth-like planets. Hence, it may be a highly valuable method to follow up small planet candidates detected in the COROT and Kepler surveys.

1.4.3 Imaging methods

The arguably most exciting method to detect exoplanets, as well as the primary concern of this thesis, is through the actual imaging of the planet itself. Once a sufficiently large contrast is reached, entire planetary systems can be studied at once, and characterized spectroscopically, giving information about a wide range of physical parameters, including the capacity to search for biomarkers. The great challenge for direct imaging is to overcome the huge brightness contrast and small angular separation characteristic of extrasolar planetary systems. Continuous progress is made in this field, as will be seen below. We will sort these methods into wavelength ranges, since very different techniques are used (or planned) for the different ranges.

Visual range

Being cool objects with temperatures generally in the range of a few 100 K, the thermal brightness of planets in the visual range is entirely negligible. Like the solar system planets that we can observe in the night sky, all light in this range from exoplanets will be reflected starlight. For an Earth-like planet, the planet-to-star flux ratio $F_\mathrm{p}/F_\star$ is a few times 10^{-10}. No astronomical instrument currently in use can come remotely close to this contrast at typical (nearby) star-planet angular separations of 0.1-1". However, steady progress is being made in this area. A primary idea is to use a coronograph to suppress the light from the star whilst conserving the flux of the companion. This can only be done from space, since a flat wavefront is necessary to distinguish the flux of the two sources. On the ground, the wavefront is distorted by the atmosphere, such that an almost perfect wavefront correction (with, e.g. adaptive optics) would be required prior to applying coronography. Many different forms of coronography have been suggested (e.g. four-quadrant phase mask, Rouan et al. 2000; phase-induced amplitude apodization, Guyon 2003). Lab experiments have demonstrated the capacity to reach the required contrast of 10^{-10} at a single wavelength (Trauger & Traub 2007). This work is very promising, but needs to be extended to wide wavelength bands before it can be practically applied.

An alternative method is to use free-flying occulters in the line of sight between a telescope and an observed star, which is discussed in Chap. 6. The main advantage of this method is that it requires less engineering precision than coronography, whereas the main disadvantage is the issue of moving the occulter from one target to the next. Occulter concepts are discussed in e.g. Cash (2006) and Vanderbei et al. (2007). The occulter concept also opens the possibility of using a space-based occulter in combination with ground-based telescopes, which is the theme of Chap. 6.

Near-infrared (NIR) range

While Earth-like planets, and many giant planets, only start to radiate thermally in the mid-infrared, young giant planets and hot Jupiters have high enough temperatures (several 100 K or above) that their thermal radiation dominates the reflected emission already in the NIR range. Meanwhile, high-contrast imaging from the ground is optimal at NIR wavelengths, since present adaptive optics (AO) systems can achieve good wavefront correction with high Strehl ratios in this range, an acceptable spatial resolution can be achieved with large telescopes, and the atmosphere is sufficiently transmissive. Differential methods can be applied to correct for residual wavefront aberrations, and distinguish physical companions from speckle noise. Indeed, these methods are central to this thesis, and will be discussed in Chapters 4 and 5.

For these reasons, the best telescopes on the ground have the capacity to detect giant planets at $\sim$ 10 AU and outwards in nearby young systems. Several high-contrast surveys have been performed to look for such objects, e.g. Masciadri et al. (2005), Biller et al. (2007), Kasper et al. (2007) and Apai et al. (2008). The results of these surveys have shown that massive planets ($\sim$5-10 M_jup) must be rare at large separations ($\sim$20 AU and outwards) from low-mass (< 1 M_sun) stars. Note, however, that this conclusion is based on theoretical mass-luminosity relationships that have been poorly calibrated. The most sensitive measurement in this context, the imaging of ϵ Eri, will be discussed at length in Chap. 4. While no planets (in the formation-based sense) have been imaged so far, several brown dwarf companions have been detected (e.g. Chauvin et al. 2005, Biller et al. 2006, Jayawardhana & Ivanov 2006), some of which may be of planetary mass.

Improved AO capacity and specialized instruments will lead to strong enhancement of NIR planet detection from the ground within a few years, with instruments such as SPHERE (e.g. Dohlen et al. 2006) for the VLT and GPI (e.g. Macintosh et al. 2006) for Gemini.

Mid-infrared (MIR) range

The thermal emission of temperate planets peaks in the mid-infrared. For instance, the emission of Earth peaks at about 10 μm. This leads to an Earth-sun brightness contrast of 1:10^7, rather than 1:10^{10} as is the case with reflected light, which is an attractive argument of exoplanet studies in the MIR range. However, the spatial resolution is worse at longer wavelengths, and achieving high contrast ratios with coronography or occultation is much more challenging than at visual wavelengths. On the other hand, interferometry is easier at longer wavelengths. An obvious advantage of interferometry is that it offers improved spatial resolution, given that the resolution is effectively set by the projected baseline between the involved telescopes, rather than the individual aperture sizes. In addition, it allows for the use of nulling interferometry. A setup of nulling interferometry, in its simplest application, involves usage of two telescope units. In a normal interferometry application with a star centered on the optical axis, the interferometric combination of the two telescopes would yield constructive interference on-axis, thus passing through the light of the star. In the nulling case, a phase shift of $\lambda/2$ is imposed on the light recorded at one on the telescopes, before combining the beams. This yields destructive interference on-axis, thus acting essentially like a coronograph, canceling out ideally all light at zero phase, whilst conserving flux at other phases.

Nulling interferometry is the main concept behind planned projects such as Darwin (e.g. Fridlund 2000) and the TPF-I (e.g. Beichman et al. 2006), which will hopefully overcome the present funding difficulties, as they would have an unmatchable impact in the field of terrestrial extrasolar planet detection and characterization.

Low-frequency radio (LFR) range

Interactions between the solar wind and magnetosphere of magnetized planets in our solar system are known to generate low-frequency radio signals. In some extrasolar planetary systems, this radiation may well be so strong that it significantly outshines the star in this range, such that finding the emission becomes a sensitivity problem rather than a contrast problem. The observable range of such emission is between about 10 and 100 MHz (the peak emission is very generally below 100 MHz, whereas no observations can be made from the ground below 10 MHz, due to ionospheric effects). In Zarka (2007), different kinds of interactions between a planet and the stellar wind were examined theoretically, considering four main cases – all combinations of a magnetized or non-magnetized stellar wind interacting with a magnetized or non-magnetized planet – and it was found that as long as either the wind or planet is strongly magnetized, LFR emission will occur. Grießmeier et al. (2007) apply the theory to known exoplanetary systems, and find that in some cases, the LFR emission could be detected with present instruments, depending on the exact mechanisms at play in each respective system.

Attempts have been made with e.g. VLA (Bastian et al. 2000) and the GMRT (George & Stevens 2007) to detect LFR radiation around some of the most promising systems, but no detections have been made so far. A promising facility for the future is the LOFAR, which is projected to significantly increase both the sensitivity and resolution in the 10-100 MHz range.

1.4.4 Other methods

Here we discuss the methods that are particular enough that they cannot easily be grouped in with other methods.

Gravitational microlensing

Due to the fact that a light path is bent in the presence of a gravitational field, any massive object can effectively act as a lens, magnifying luminous objects in its immediate background. Such gravitational lensing can be readily observed on a galactic scale, where, e.g., a foreground galactic cluster maps background galaxies onto arcs or multiple ghost images on the sky. The lensing also takes place on a stellar scale, but due to the low spatial density of stars in the galaxy, it is extremely rare for a given star at any given time to happen to pass closely enough to the line of sight between an observer and a background star to have a noticeable effect. However, towards the galactic center, the projected number density of background stars is large enough as seen from Earth that a significant number of observable magnification events occur every year (several hundreds at the present instrumentation capabilities). Typically in those cases, the background star is a giant or bright main-sequence star in the galactic bulge, and the foreground object is a low-mass star anywhere in the line between the background object and Earth. The lens star is not seen during the event (nor for a certain period afterwards), as it is blended with the background star (also called source star) as well as many other stars at the typical resolution of ground-based telescopes.

At a perfect alignment, the lens would cause the background star to appear as a ring with angular radius

$$\theta_{\mathrm{E}} = \sqrt{\frac{4GM_{\star}D_{\mathrm{LS}}}{c^2 D_{\mathrm{L}} D_{\mathrm{S}}}} \tag{1.4}$$

where D_{L} is the distance to the lens star, D_{S} the distance to the background star, and D_{LS} the distance between the lens and background stars. θ_{E} is the Einstein ring radius, a fundamental parameter in gravitational lensing. For the case of a close but non-perfect alignment, the background star gets two images, aligned along the extended line between the lens and the actual position of the star – one image is outside of the Einstein ring radius, on the same side of the star as the real position, and the other is inside the ring radius, on the opposite side of the star. With present instruments, we are far off from spatially resolving the effect. However, the images are also magnified by a total factor A that depends directly on the projected separation between the lens and background object u:

$$A = \frac{u^2 + 2}{u\sqrt{u^2 + 4}} \tag{1.5}$$

As the lens moves along its trajectory with respect to the background, A develops over time during the lensing event, so that measuring the lightcurve of the background star gives information about the lens (though as long as the lens is unidentified, there is a degeneracy between its proper motion and its Einstein ring radius).

So, how does this relate to planet detection? The answer to this well justified question is that if the lens star has a planet, and during the lensing event an already magnified image of the background star comes close to the position of the planet, it will be further magnified, causing a sharp peak in the measured lightcurve. This signature can be detected even for quite small planetary masses, as long as the temporal sampling is sufficiently dense. It may seem like a small chance that during any given lensing event, an image should happen to pass close to a planet. However, in the special case of a high-magnification event, where the background star passes well within θ_{E}, it is almost inevitable to detect planets that have a projected separation close to θ_{E}. The reason for this is that the lensed images are highly magnified and close to the Einstein ring, covering practically every part of it at some point during the lensing event.

Gravitational microlensing for exoplanet searches was suggested early on (e.g. Gould & Loeb 1992). The present strategy for detecting planets with gravitational microlensing is based on a worldwide network of telescopes and an alarm system, such that as soon as the start of a magnification event is recorded (in particular high-magnification events), an alert is issued, and every collaborating telescope that has the possibility to observe the target does so. This enables a high temporal sampling, and mutually corroborating data of these non-repeatable events. This has resulted in a successful survey with FILL detected planet candidates (see e.g. Bond et al. 2004, Beaulieu et al. 2006). For the future, a space-based dedicated telescope would provide very significantly improved sensitivity to microlensing events, enabling detections of hundreds of planets all the way down to about 0.1 M_{Earth} (e.g. Bennett et al. 2007), thus providing a statistical census of terrestrial and giant planet companions to low-mass stars in the galaxy.

Planet-disk interactions

In previous sections, it was discussed how planets can be detected indirectly through gravitational interaction with their parent star. The planet will also interact with any circumstellar material in its vicinity, sometimes causing observable signatures. There have been a variety of

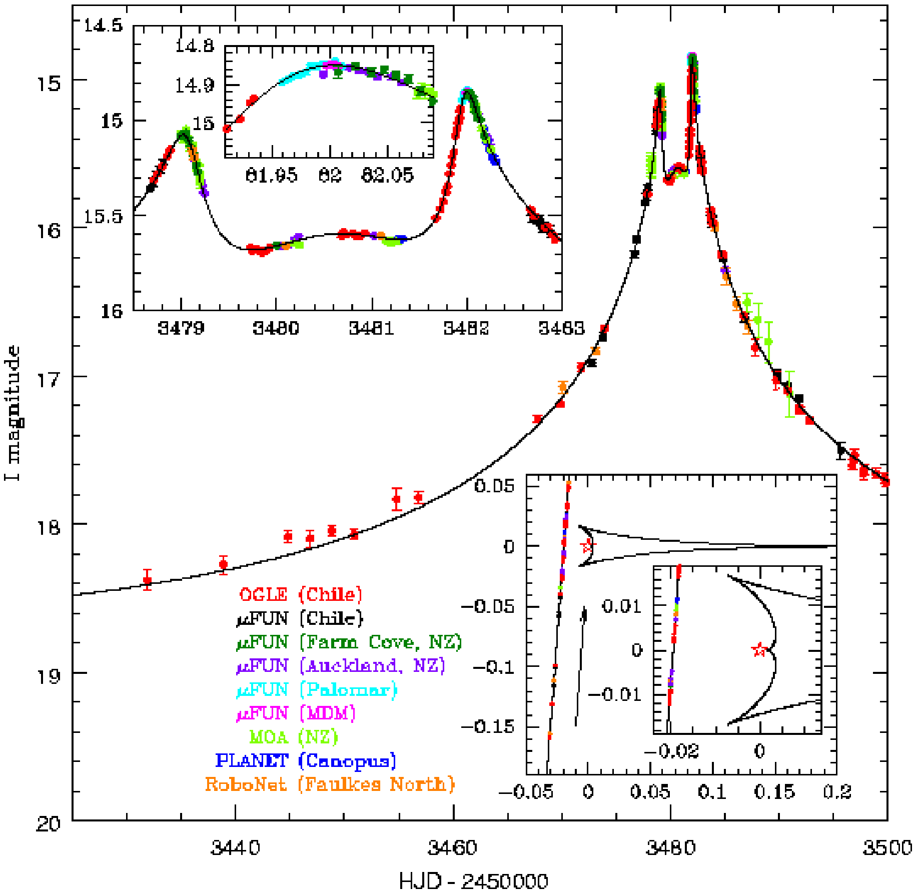

Fig. 1.5: A microlensing event where the lens has a planetary companion (Udalski et al. 2005). Inset on the upper left are details of the lightcurve. Inset on the lower right is the corresponding best-fit caustic pattern on the sky relative to the source-lens motion.

suggestions for such interactions in the scientific literature, with varying degrees of ambiguity. For spatially unresolved debris disks that are observed through the infrared excess of the parent star, the lack of warm excess but presence of cold excess implies an inner clearing of the disk. Such a clearing could be due to the presence of a giant planet in some cases, but could also be due to other effects (e.g. Takeuchi & Artymowicz 2001). The planet hypothesis was tested for a number of targets in Apai et al. (2008), and although it could not be excluded for those cases, it was found unlikely. In the cases where a debris disk can be spatially resolved, more detailed predictions can be made, since the structure and sub-structure (to some extent) can be observed. Specific predictions of planetary companions have already been made in some cases, such as for the disk around Fomalhaut (see Quillen 2006). The debris disks observed so far are on the extreme upper end of disk masses – smaller disks (such as the one represented by the asteroid and Kuiper belts in the case of our solar system) are undetectable due to the high star-to-disk contrast. Once planet-search mission such as those discussed in Sect. 1.4.3 are in place to defeat such contrasts, disks can as a consequence be studied in more detail as well. This could be used to infer the presence of unseen companions, as well as constrain masses for seen companions.

In the evolutionary earlier stage of protoplanetary disks, planets may cause observable signatures in the disk as part of their formation process. Such effects have been studied by Wolf et al. (2007), finding that gaps created by a forming giant planet, as well as the accretion region surrounding the planet itself, could be observable with potent sub-millimeter arrays such as the developing ALMA project.

Chapter 2

Early ComeOn+ adaptive optics observation of GQ Lup

From Janson et al. (2006): A&A 453, 609

2.1 Abstract

We present an analysis of adaptive optics K-band imaging data of GQ Lup acquired in 1994 by the first generation adaptive optics system ComeOn+ at the ESO 3.6m optical telescope in La Silla. The data reveal a likely candidate for the low-mass companion recently reported in the literature. An a posteriori detection in the 11-year old data would provide a useful astrometric data point for the very long-period ($\sim$ 1000 yr) orbit of the GQ Lup system. However, the data is severely contaminated by speckle noise at the given projected separation, which decreases the confidence of the detection. Still, from the data we can conclude that GQ Lup B is not an unrelated background source, but instead a physical companion to GQ Lup A. We present here the reduction and analysis of the ComeOn+ images, as well as the results. We also discuss the nature of the companion based on data and models available in the scientific literature and examine claims made regarding the classification of the object as a planet.

2.2 Introduction

Due to advances mainly in the field of adaptive optics (AO), it has been possible over the past few years to detect substellar-mass companions to stars at increasingly small separations and at higher contrast. We are presently at a point where planetary mass companions can be detected in young systems, if they are at a sufficiently large projected separation. However, due to uncertainties in theoretical models and age estimates, large ambiguities can easily occur in the estimated mass and thus in the classification of an object.

The first confirmed detection of a planetary mass object orbiting the brown dwarf 2MASS J1207334-393254 was reported by Chauvin et al. (2004, 2005). Neuhäuser et al. (2005a, henceforth referred to as N1 thorughout the chapter) report on the confirmed detection of a companion to the young K-star GQ Lup. The mass estimate given for this companion in N1 was 1 to 40 $M_{\rm jup}$ (subsequent, more detailed analysis in McElwain et al. 2007 and Seifahrt et al. 2007 gives a range of 10 to 40 $M_{\rm jup}$). Since planets are usually defined as having masses lower than the deuterium-burning limit of about 13 $M_{\rm jup}$ (sub-stellar objects above this mass are defined as brown dwarfs), the classification of the object was left an open issue by the authors. In a subsequent publication (see Mugrauer & Neuhäuser, 2005) and in conference proceedings (see Neuhäuser et al. 2005b, henceforth N2), they have argued for the interpretation of the object as a planet rather than a brown dwarf.

Since 1994, we have been carrying out high-angular resolution, ground-based adaptive optics (AO), and HST observations of young stars with the aim of searching for close stellar and substellar companions (e.g. Brandner et al. 1995, 1997, 2000 and Masciadri et al., 2005). As part of this campaign, GQ Lup was observed in 1994 using the ComeOn+ adaptive optics system. Given the brightness and large separation from its stellar companion, GQ Lup B should be detectable a posteriori upon re-examination of the ComeOn+ data. Here we present the result of such an examination. We also examine the nature of the source, using known measurements and data from literature, and discuss the results.

2.3 Observations and data analysis

The observations of GQ Lup were obtained on April 2, 1994 with the adaptive optics (AO) system ComeOn+ and the near-infrared camera Sharp2 at the ESO 3.6m telescope in La Silla, Chile. The image scale was 0.05 arcsec/pixel, and observations were obtained with a K-band filter in order to benefit best from the AO correction. For sky subtraction, GQ Lup was alternatively observed in the lower left and upper right quadrant of the detector. Individual exposure times were 1 s, and a total of 80 frames were obtained.

Astrometric calibrations were achieved through observations of the astrometric binary IDS 17430S6022 (van Dessel & Sinachopoulos 1993). The observations yield an image scale of 50.15±0.10 mas/pixel and show that the detector y-axis was aligned with the North direction to within ±0.20 deg. The first step in the data reduction consisted of using eclipse tasks (Devillard, 2001) to slice the data cubes into individual 2-dimensional fits-frames, and to apply background subtraction and flat field corrections.

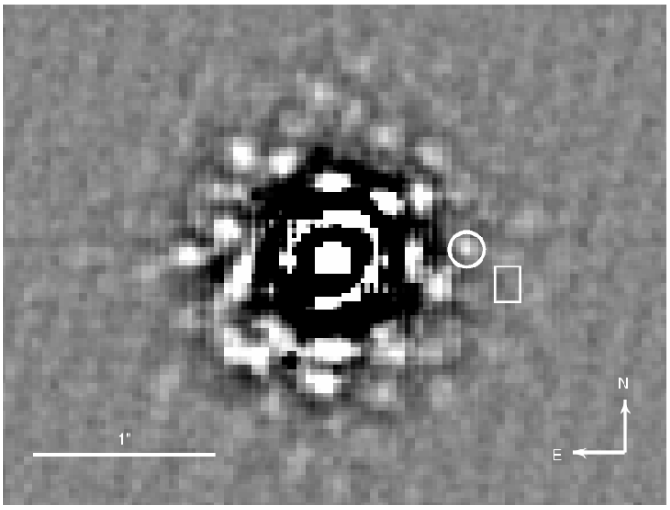

Fig. 2.1: K-band image of GQ Lup after low-frequency filtering was applied. The circle marks the location of a possible companion (the brightness contrast is $\Delta K = 6.24 \pm 0.13$ mag). The square marks where the object would be expected if it had been a background source. The image was taken with the ComeOn+ instrument.

While the AO correction in general was good and stable, not all frames have the same Strehl ratio (SR). The average SR was 0.21, while the single best SR achieved was 0.33. In order to optimize the signal-to-noise for faint sources located in the point-spread-function (PSF) wings of GQ Lup, we applied an image selection, selecting a subset of 20 frames with good SR. More details on the rationale behind the image selection of ComeOn+ and other AO data can be found, e.g., in Tessier et al. (1994) and Brandner et al. (1995).

The selected frames were then registered (in order to remove residual tip-tilt errors) and combined with the drizzle task in IRAF, selecting a 2-times oversampling of the data. In order to further facilitate the detection of faint companions, a high-pass filter was applied to the data, effectively removing the smooth, sloping background in the PSF wings and revealing potential companions. Figure 2.1 shows the resulting image. Using a priori knowledge of roughly where GQ Lup B should be located with respect to GQ Lup A from N1, we found one unique candidate for the object among the many object-like features (due to speckle noise) in the data.

2.3.1 Analysis of the suspected companion

We calculated separation, position angle, and magnitude difference between the companion and the primary by fitting Gaussians and background to both objects using the imexamine task in IRAF. The properties of the primary were obviously measured in the non-filtered counterpart to the image shown as they are affected by the high-pass filtering. The flux of the secondary was also calculated in the non-filtered frame, as it will also be affected to a limited extent by the filtering, which would influence the relative photometry.

Error estimations based on results from individual frames are particularly difficult when a strong impact of speckle noise is present. This is in part due to the fact that a noise speckle, in contrast to e.g. photon noise, forms a coherent structure in space during its lifetime (for an extensive analysis of speckle noise, see Racine et al., 1999). This means, e.g., that if a noise speckle ends up close to the source in a frame or series of frames, the centroiding procedure will be skewed due to the slope introduced from the speckle in a way that cannot be seen as random noise with a Gaussian distribution. In addition, the centroiding will fail altogether in a case where e.g. the source coincides with a local minimum in the speckle pattern. This means that the frame in question cannot be used in the calculations, which in turn means that the estimations will be biased towards certain realizations of the speckle pattern.

In order to avoid bias to the greatest possible extent, we do not calculate the errors based on centroiding for each frame, but instead divide the frames into two groups of the first and last ten frames in the set, respectively. We estimate the error from the difference between the averaged frames of the two groups. The frames for this estimation were high-pass filtered. Obviously, an error estimate based on statistics from two data points is largely statistically uncertain in itself. This is still preferable to the biased estimates from centroiding in each frame (which for this case give lower statistical errors).

Using this method, we get a separation of 713.8 ± 35.5 mas, a position angle of 275.5 ± 1.1 deg and a magnitude difference of ΔK= 6.24 ± 0.13 mag. In N1, the magnitude difference is ΔK= 6.1 ± 0.1 mag. The values agree within the statistical errors. It should be noted that ΔK can vary systematically, because GQ Lup A is a variable source (see Sect. 2.4.2).

The statistical error is not the greatest danger in interpreting the data. Since some speckle features are fairly persistent in the data (present during a wide range of frames), they also form coherent structures in the averaged data. Misclassification of any given remaining speckle as an object is not a problem as such, since we have a priori information about the vicinity of the companion, which only leaves one reasonable candidate in this case. Rather, the problem is that interference between the source and the remaining speckle pattern could in principle cause severely biased measurements.

To test the extent of this effect we introduced three artificial structures (Gaussians) in the data with the same expected flux and separation from the star as the real source. For two of these cases, the fake source happened to be positioned near local maxima in the speckle pattern. This led to a brightness that was 2-3 times too high. For the third case, the measured brightness matched the expectation from the known properties of the fake source. All sources had large variations in the measured flux between different frames, showing that they continuously interfere with a dynamical speckle structure.

For the real source, positive interference with a speckle is obviously not a problem, because no such overly bright feature is present where the source should be. However, it cannot be entirely excluded that the real source happens to coincide with a local minimum in the speckle pattern, such that it is hidden in the final data. In this scenario, we would be measuring on a neighbouring local maximum of the speckle pattern, which would essentially mean a non-detection of the source itself. For this reason, rather than claiming a detection of the source in the ComeOn+ data, we postulate that the observed structure is the most probable candidate for GQ Lup B.

2.3.2 Examination of the background hypothesis

Another interesting investigation that can be performed in the ComeOn+ data is to examine the point (relative to GQ Lup A) where GQ Lup B would be expected to appear if it had been a background source. A null detection at this position would further reinforce the (already very solid) conclusion in N1 that GQ Lup B shares a common proper motion with GQ Lup A, and would thus also strengthen our a priori assumption of where GQ Lup B should be positioned. Such an examination can be made with much higher confidence than in the common proper motion case, because the hypothetical non-common proper motion case leads to a significantly greater separation at the epoch of the ComeOn+ data aquisition (see Figs 2.1 and 2.2). At the separation of a non-common proper motion case, the impact of speckle noise, and thus potential bias, is much smaller. In addition, the position is further out in the PSF wings of the primary, making background estimation and subtraction less cumbersome.

For this purpose we used the weighted mean of several measured proper motions given in Mugrauer & Neuhäuser (2005). This gives $\mu_\alpha \cos(\delta) = -19.15 \pm 1.67$ and $\mu_\delta = -21.06 \pm 1.69$. It is clear that there are discrepancies between many of the measurements beyond their statistical error bars. A null detection in our data is however quite insensitive to the detailed accuracy of these measurements, because the remaining speckles at the greater separation of a background equivalent to GQ Lup B are too dim (by a factor of at least 2) to constitute false positives.

A search in the area where a non-common proper-motion equivalent to GQ Lup B would be expected indeed yields no realistic candidates in the final averaged frame. In order to further test whether this is a strong conclusion, we placed another artificial source in the data with the expected properties of GQ Lup B, at the same separation as a hypothetical background object. The measured flux of the artificial source is in excellent agreement with expectations and with much smaller variations between frames than in the less separated cases. This leads us to conclude that the hypothesis that GQ Lup B is a background object can be safely excluded from the ComeOn+ data.

2.4 Discussion

2.4.1 The data

It is important to stress the fact that a detection of GQ Lup B in the ComeOn+ data can only be made a posteriori. This is due both to how the speckle features in the data mimic companion signatures, as well as how the speckle pattern varies at and around the position of the companion, making its features uncertain. These uncertainties are partly reflected in the rather large error bars of the measurements presented. It is, however, theoretically possible that bias from speckle influence gives a systematic error beyond the error bars. As mentioned above, the positions of the primary and companion in our data give a separation of 713.8 ± 35.5 mas and a position angle of 275.5 ± 1.1 deg. The separation is included in a reconstructed diagram from N1 in Fig. 2.2. A similar diagram has been constructed for the position angle, shown in Fig. 2.3.

As previously mentioned, we can exclude that the source is a background object. While it should be possible for the sources to share a common proper motion without being physically bound (as independent members of the Lupus association), it is shown in Mugrauer & Neuhäuser (2005) that this possibility can be rejected with high confidence for the case of GQ Lup. Thus it can be safely assumed that GQ Lup A and B are indeed physically bound.

Due to the large uncertainties in the data and short observational baseline relative to the orbital period of the system, not much can be said about the specific properties of the orbit. However, it can already be seen from the 1999 epoch data and onwards that the position angle changes considerably more slowly than what would be expected if the orbit was circular and face-on. This implies that the orbit is either elliptical and currently near apastron, has a significant inclination, or both.

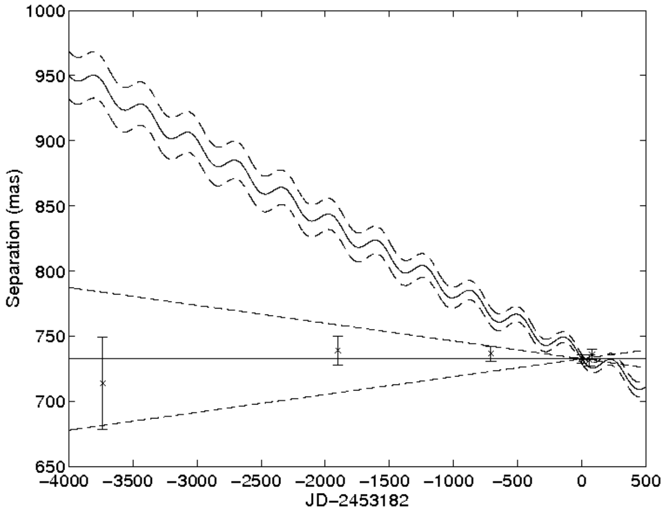

Fig. 2.2: A recreated figure from N1 with inclusion of the data from the most probable candidate in the ComeOn+ image. Straight lines indicate expected parameter space for a proper motion companion to GQ Lup A assuming orbital motion of less than ±5 mas/yr (dashed lines are the upper and lower limits, full line is the mean). Wobbly lines indicate the expectation for a background source. The parallax is assumed to be 7.1 mas.

2.4.2 The GQ Lup system

It is concluded in N1 that both planetary and brown dwarf masses are included within the error bars of the mass estimation and that a classification of the object based on current knowledge is thus not possible. In N2 instead it is concluded that the object is 'almost certainly a planet', based mainly on a different emphasis on which models to use. Using measurements and models from the scientific literature, investigated the nature of the source in order to add to the discussion on whether or not the companion is a planet.

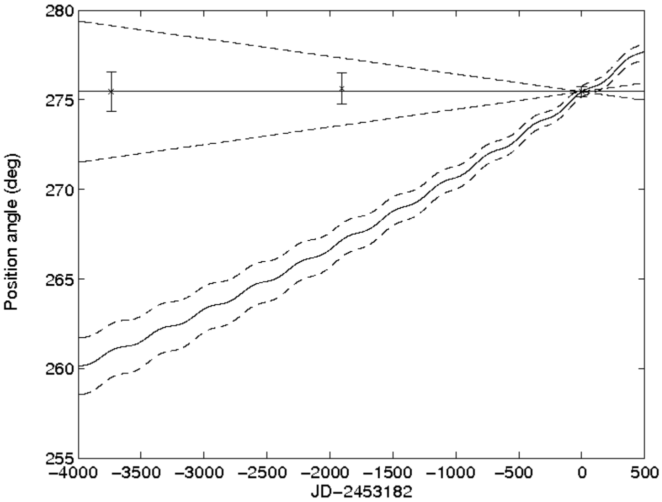

Fig. 2.3: Same as Fig. 2.2 but for position angle instead of separation. The dashed straight lines indicate the expected movement of a companion on a circular, face-on orbit of 1000 years. The considerably smaller movement implied by the data may indicate an inclined orbit, or an elliptical orbit near apastron.

Distance

It is important to begin with a discussion of the distance to GQ Lup. The star has no parallax measured, so any distance estimation has to be made through its highly probable association with the Lupus I molecular cloud. Distance estimates to the Lupus clouds have varied quite a lot historically, but more recently applied methods such as ubvyβ photometry (see Franco, 1990) and projection of the cloud complex on its background (see Murphy et al., 1986) give a fairly consistent result of 150 ± 20 pc. Based on extinction jumps among sources in the direction of the Lupus clouds with known distances, Knude & Hog (1998) estimate a distance of about 100 pc to the Lupus clouds. However, due to the inconsistency with other results, and since the effect could either way not be shown for the Lupus I cloud, we disregard this result and use 150 ± 20 pc as mentioned above. This range is a bit more restrictive than the 140 ± 50 pc distance estimate used in N1. Eventually, a parallax measurement will have to be performed in order to get an entirely reliable distance to GQ Lup.

Brightness and extinction

GQ Lup is a highly variable source. Since the brightness varies, it is difficult to find the ‘true’ brightness of the system, i.e. the brightness that corresponds to the actual radius of the star. This is the brightness that is relevant when placing the star in an HR diagram to deduce its age and mass from modelled evolutionary tracks. Herbst et al. (1999) mention that GQ Lup varies in visual brightness by more than two magnitudes. This is based on measurements (available from `ftp://www.astro.wesleyan.edu/pub/TTauri/WTTS/`) over three different epochs, giving $V_{\rm min} = 11.33$ mag and $V_{\rm max} = 13.36$ mag. However, we disregard the first epoch, since those measurements give no colour index in the ranges that interest us (this has a minimal effect on the brightness estimation). We also disregard the third epoch, where all values with $V \geq 12$ mag are present. This is because those values represent a minority of the data and values from other sources at other epochs (e.g. Bastian & Mundt, 1979 and Mundt & Bastian, 1980) are all within $V = 11$ to 12 mag, implying that the epoch 3 data represents an extreme rather than the normal behaviour of the source. We will, however, mention in Sect. 2.4.2 what including these values would lead to.

For T Tauri stars, it is risky to calculate the interstellar extinction based on the colour excess in $B-V$. This is because accretion of material from the disk onto the star causes a UV excess that can have a significant effect on the B-band. Instead, we can use colours $V-R$ and $R-I$ (given along with the brightness at the mentioned website) independently to check whether the results are consistent. We find that $A_{\rm R} = -0.062 \pm 0.19$ mag and $A_{\rm I} = -0.031 \pm 0.19$ mag. Since a negative extinction value is obviously impossible, we set the extinction to zero with an upper limit of $A_{\rm R,max} = 0.13$ and $A_{\rm I,max} = 0.16$. Is zero extinction a reasonable result? For GQ Lup, the answer is yes. Over a distance of only about 150 pc, interstellar extinction has a low impact if no dense regions occur between the source and observer. The Lupus I molecular cloud, of which GQ Lup is a member, is not expected to contribute to the extinction either, for two reasons. First, faint sources in a molecular cloud are more easily detected if they are on the near side of the cluster than on the far side, and thus a certain detected T Tauri star is obviously more likely to be on the near side. Second, and more important, it is clear from CO maps of the Lupus clouds (see Tachihara et al., 1996) that GQ Lup is at the very edge of the Lupus I cloud, and will therefore not experience much extinction from the cloud regardless of depth. In addition, GQ Lup is a weak-line T Tauri star with a $W_{\rm H\alpha}$ of only 2.8 Å. Thus, the circumstellar disk will also not contribute largely to the extinction.

Age and mass estimation

Using these values for distance, apparent magnitude and extinction, we derive absolute magnitudes of $M_{\rm R} = 4.92^{+0.40}_{-0.73}$ mag and $M_{\rm I} = 4.16^{+0.60}_{-0.67}$ mag. Using known relations between luminosities and magnitudes in the respective photometric bands for a K7 star (equivalent to applying a bolometric correction), we get nicely consistent values of $L(R) = 0.87^{+0.83}_{-0.37} L_{\rm sun}$ and $L(I) = 0.86^{+0.74}_{-0.36} L_{\rm sun}$. We henceforth use the slightly less restrictive luminosity measure derived from the R-band photometry.

From the spectral type of GQ Lup, we get $\log(T_{\rm eff}) = 3.61 \pm 0.01$. Knowing both the temperature and luminosity, we can place the source in an HR diagram, and from theoretical evolutionary tracks for PMS stars get an estimate for the mass and age of GQ Lup. We use two different models for this purpose: Siess et al. (2000) and D'Antona et al. (1997). The Siess et al. (2000) model gives a rough age range of $7 * 10^5$ to $5 * 10^6$ years, whereas the D'Antona et al. (1997) model gives $3 * 10^5$ to $2 * 10^6$ years. Given the uncertainty of the models at such low ages, the consistency between the results is reasonable. Compared to the age range suggested in N1 of 0.1 to 2 Myrs, the D'Antona et al. (1997) model gives a consistent age, whereas the age estimated from Siess et al. (2000) is somewhat higher. For mass estimations, the Siess et al. (2000) model gives a range of 0.6 to 0.8 $M_{\rm sun}$, and the D'Antona et al. (1997) model gives 0.4 to 0.6 $M_{\rm sun}$. For both mass and age, we adopt the full range given by the extremes of the two models. It should be pointed out for completeness

Tab. 2.1: Physical properties of GQ Lup A & B

Properties	A	B
Distance (pc)	130-170	same
$A_{\mathrm{R}}(mag)$	0-0.13	same
Spectral type	K7Ve	M9-L4
$L_{\mathrm{bol}}/L_{\mathrm{sun}}$	0.50-1.71	0.0025-0.01
Age (Myr) [a]	0.3-5	same
Mass [a]	0.4-0.8 M_{sun}	3-50 M_{jup}

[a] Model-dependent estimations. The lower and upper values do not correspond to the overlapping regime of the models, but to the extremes of the combined ranges.

that if the full range of photometric values measured is taken into account (see the discussion on variablilty in Sect. 2.4.2), the upper limit of the age is extended to the point where every age up to the ZAMS is possible. Some D'Antona et al. (1997) evolutionary tracks along with GQ Lup A are shown in Fig. 2.4.

The nature of GQ Lup B

Having calculated some of the fundamental properties of the GQ Lup system using the A component, we can attempt to establish the nature of GQ Lup B/b. Using the photometric data given in N1, and the distance and extinction values used in this thesis, using the same procedure as above, we get a logarithmic luminosity of about $\log(L/L_{\mathrm{sun}}) = -2.3 \pm 0.3$. We adopt the same broad temperature range as N1 of 1200 to 2500 K.

Using the luminosity and temperature given, along with the age calculated for the primary (assuming an equal age of the components in the system), we can estimate the mass with theoretical models, though it is highly unclear to what extent present models can be applied to such a low-mass object, and in particular for such a young age range. From Fig. 1 in Baraffe et al. (2003) and the corresponding table at perso.ens-lyon.fr/isabelle.baraffe, using luminosity and age we get masses from $\sim 12\ M_{\mathrm{jup}}$ to $\sim 40\ M_{\mathrm{jup}}$. Using temperature and age we get masses from $\sim 3\ M_{\mathrm{jup}}$ to $\sim 20\ M_{\mathrm{jup}}$. The results leave both a planetary and a brown dwarf interpretation of the object open. We thus conclude that with the data present it is not possible to determine the classification of GQ Lup B and that improvements must be made in both measurements and models for such a step to be taken. This conclusion is very similar to the one drawn in N1, except that they also present results from an extension of a model of Wuchterl et al. (2003) that gives masses all well below the planetary limit.

In N2 there is instead much stronger emphasis on the classification of GQ Lup B/b as a planetary object, and it is eventually claimed that the object is almost certainly a planet. This statement is based mainly on arguments regarding which models are the most appropriate. The Wuchterl et al. (2003) model is preferred to the Burrows et al. (1997) and Baraffe et al. (2002) models, since it takes physical consideration to the initial cloud collapse. However, as is rightly implied in N1, neither of the models have been properly calibrated for such young, low-mass objects. Even though Wuchterl et al. (2003) give a seemingly more complete physical picture of the evolution of PMS stars by including the protostellar collapse, this is certainly not a guarantee that the results will necessarily be better. This must be tested against, e.g., dynamical observations of bodies in the relevant mass and age range. We discuss some further aspects of the issue of evolutionary models for the case of GQ Lup B in Sect. 2.4.2.

Other arguments in N2 concern results reached by comparison of the measured spectra of the companion with artificial spectra generated by the GAIA-dusty model and results presented in Mohanty et al. (2004). The latter results are also based on spectral models. Both these models are extensions of the Allard et al. (2001) model, but neither of the two has been published in a refereed context. The Allard et al. (2001) models had severe problems in some cases for young low-mass objects (see Burgasser et al., 2004). Even though the updated models contain more detailed physics, such as updated (but still incomplete) line lists to account for these problems, this fact serves as a caution that it is dangerous to apply such models in ranges for which they have not been tested. Again, dynamical observations are needed to calibrate the models.

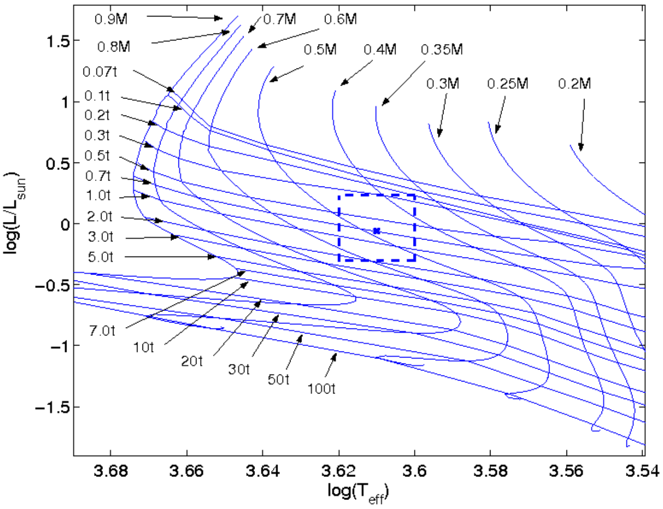

Fig. 2.4: Evolutionary mass tracks from D'Antona et al. (1997). Tracks labelled 'M' are mass tracks in units of $M_{\rm sun}$. Tracks labelled 't' are isochrones in units of Myr. The dashed square indicates the range of luminosities and effective temperatures of GQ Lup A as given in the text.

In N2 a statement is made that can be easily interpreted as meaning that, according to both Mohanty et al. (2004) and Close et al. (2005), the models of Baraffe et al. (2002) underestimate the masses of objects with actual masses $> 40 M_{\rm jup}$ but overestimate them for objects $< 30 M_{\rm jup}$. While Mohanty et al. (2004) do indeed state this, it is important to note that Close et al. (2005) make the opposite assumption (based on extrapolation of the observed trend) about masses below that of their object of study, AB Dor (about 90 $M_{\rm jup}$). This is an important distinction, since the mass of AB Dor is determined dynamically. It is found that theoretical mass tracks underestimate the mass of AB Dor by a factor of about 2.5 (but see also e.g. Luhman et al. 2005 and Nielsen et al. 2005 for further discussions). Another survey of dynamical masses versus evolutionary tracks of young, low-mass stars (down to 300 $M_{\rm jup}$) performed by Hillenbrand and White (2004) shows a similar trend, namely that the masses tend to be underestimated by theoretical tracks. Whether this trend can be extrapolated to even lower-mass objects such as GQ Lup B/b or whether there is an opposite trend as suggested by Mohanty et al. (2004) is still very much an open issue from a dynamical point of view. Suitable sources for such comparisons, which can be observed both photometrically and dynamically, are still lacking.

Another point needs to be mentioned regarding the presentation of results from Mohanty et al. (2004) in N2. It is claimed that the faintest object from Mohanty et al. (2004) is about 9 $M_{\rm jup}$ and that since GQ Lup B/b is both colder and fainter, it must be lower in mass, giving a mass estimate of ≤ 8 $M_{\rm jup}$. However, it is clear from Mohanty et al. that the errors are within a factor of two. Thus the upper limit is 18 $M_{\rm jup}$, meaning the mass estimate of GQ Lup based on this would be ≤ 17 $M_{\rm jup}$, which includes super-planetary masses.

As a final comment on the issue of the physical nature of GQ Lup B, it should be noted that the object does not seem to constitute a new class of its own. Several detected objects exist with observed properties similar to those of GQ Lup B, for instance HR 7329 B, GG Tau B, and AB Pic B. If GQ Lup B is to be classified as a planet, then it is possible that several of these objects are planets as well. This abundance of possible borderline cases further underlines the fact that it is important to validate the theoretical models before making a definite statement about the nature of these objects.

The history of the system

In Fortney et al. (2005), a model is presented for the formation of $2M_{\rm jup}$ planets based on the core accretion scenario (subsequently extended by Marley et al. 2007). It is found that the planets become fainter with this model than what the model of e.g. Baraffe et al. (2003) gives for the same mass at young ages. This means that according to the Fortney et al. (2005) model, the Baraffe et al. (2003) model underestimates the masses of young, low-mass objects, which is opposite to the conclusion of Wuchterl et al. (2003). It is worth noting that, for masses below $13M_{\rm jup}$, N1 use a modified version of Wuchterl et al. (2003) that is based on nucleated instability, since the object cannot collapse by itself for such low masses in this model. In other words, the modified model assumes a core accretion formation scenario, just like the model of Fortney et al. (2005). However, Fortney et al. (2005) specifically treat the runaway accretion of gas onto the core in the context of the solar nebula, whereas the modified Wuchterl et al. (2003) model in N1 treats the gas collapse onto the core with the same boundary conditions as for a regular protostellar cloud collapse (or so we interpret the description in N1). Thus the Fortney et al. (2005) model is possibly more appropriate for objects that form in a circumstellar disk. Of course, the Fortney et al. (2005) and Wuchterl et al. (2003) models both suffer from the same lack of dynamical calibration as was already mentioned.

This discussion inevitably brings to light the issue of how and where GQ Lup B was formed. Giant planets are highly unlikely to form at a separation of about 100 AU, since the disk is not sufficiency dense so far out. It is possible that GQ Lup B formed in the disk of GQ Lup A at a smaller separation and was subsequently thrown outwards through e.g. a planet-planet interaction. On the other hand, theoretical star formation models based on turbulent fragmentation (see e.g. Padoan & Nordlund 2002) indicate that objects far below the stellar mass limit can form independently in the same way as ordinary stars. It is hardly relevant to refer to objects formed in such a way as planets, regardless of their final mass. Thus if such a formation scenario is applicable down to a few Jupiter masses (some arguments for this case are presented in Chabrier et al. 2005), this may affect also the appropriate classification of GQ Lup B, given its peculiar orbit. In addition, assumption of co-evality would not necessarily hold in such a scenario, making the age of GQ Lup B unknown.

There is also a timescale issue. As we have seen, the N1 variant of the Wuchterl et al. (2003) model presumes that GQ Lup B formed by the core accretion-gas capture scenario. However, such a scenario most likely takes place over a timescale of the order of at least 10^6 yrs. It is not obvious whether such a timescale is compatible with the low estimated age of the GQ Lup system. It should be mentioned in this context that if GQ Lup B did form in the disk of GQ Lup A through core accretion despite the timescale and orbital problems, then it is considerably younger than GQ Lup A, rather than co-eval. In such a case, an otherwise accurate model would overestimate the mass of GQ Lup B under the assumption of co-evality.

2.5 Conclusions

The strong impact of speckle noise in our eleven-year old data leads to a weak conclusion about the detection and properties of GQ Lup B. The only candidate object in the data has reasonable flux and position values. It cannot, however, be entirely excluded that the detection is due to a persistent bias in the data.

A stronger conclusion based on the ComeOn+ data is that GQ Lup B is not a background object, since no matching object can be found near the position relative to GQ Lup A, where such an object would be expected. The impact of speckle noise is considerably lower at this position, which means that if there was a source there with the brightness of GQ Lup B, we could indeed expect to see it.

Based on huge uncertainties in both currently available data and models, we conclude that it is impossible to classify GQ Lup B exclusively as a planetary mass object or a brown dwarf. Efforts that could eventually help resolve this ambiguity include dynamical measurements of the GQ Lup system, a parallax measurement of the system, an extensive study of the variability of GQ Lup A, and dynamical calibrations of evolutionary and spectral models from other similar objects.

Tab. 2.2: Observing log of high-angular resolution imaging observations of GQ Lup

Date	MJD	Telescope/Instrument	Filter	sep [mas]	PA [deg]	ΔK [mag]	Reference
2. April 1994	49445	ESO 3.6m/ComeOn+	K	713.8 ± 35.5 [a]	275.5 ± 1.1 [a]	6.24 ± 0.13	Janson et al. (2006)
10. April 1999	51279	HST/WFPC2	F606W/F814W	739 ± 11	275.62 ± 0.86	not given	N1
17. July 2002	52473	Subaru/CIAO	K & L'	736.5 ± 5.7	not given	not given	N1
25. June 2004	53182	VLT/NACO	K	732.5 ± 3.4	275.45 ± 0.30	6.1 ± 0.1	N1
25. Aug. 2004	53243	VLT/NACO	K	731.4 ± 4.2	not given	not given	N1
14. Sept. 2004	53263	VLT/NACO	K	735.8 ± 3.7	not given	not given	N1

[a] Error bars refer to statistical error. See the text for discussion of possible biases.

CHAPTER 3

IMPROVED AGE CONSTRAINTS FOR THE AB DOR QUADRUPLE SYSTEM

From Janson et al. (2007c): A&A 462, 615

3.1 Abstract

We present resolved NACO photometry of the close binary AB Dor B in H- and Ks-band. AB Dor B is itself known to be a wide binary companion to AB Dor A, which in turn has a very low-mass close companion named AB Dor C. These four known components make up the young and dynamically interesting system AB Dor, which will likely become a benchmark system for calibrating theoretical pre-main sequence evolutionary mass tracks for low-mass stars. However, for this purpose the actual age has to be known, and this subject has been a matter of discussion in the recent scientific literature. We compare our resolved photometry of AB Dor Ba and Bb with theoretical and empirical isochrones in order to constrain the age of the system. This leads to an age estimate of about 50 to 100 Myr. We discuss the implications of such an age range for the case of AB Dor C, and compare with other results in the literature.

3.2 Introduction

AB Dor A is one of the most active late-type stars in the solar neighbourhood. Because of its short rotational period of approximately 0.514 days (Pakull 1981, Innis et al. 1998), resulting in a high level of activity and variability in X-rays (e.g. Kürster et al. 1997, Schmitt et al. 1998, Sanz-Forcada et al. 2003), and at optical (e.g. Collier Cameron et al. 1999, Cutispoto et al. 2001) and radio wavelengths (e.g. Lim et al. 1994), it was initially classified as an evolved star, possibly a RS CVn or BY Dra type variable (e.g. Pakull 1981). Its high Lithium abundance, however, soon led to the suggestion that AB Dor is not an evolved star, but still in its post-T Tauri evolutionary phase (e.g. Rucinski 1983, Vilhu et al. 1987). Based on the Hipparcos parallax measurements for AB Dor (HIC 25647) of $\pi(\mathrm{abs}) = 66.92 \pm 0.54$ mas, corresponding to a distance of 14.94 ± 0.12 pc (Perryman et al. 1997), Wichmann et al. (1998) concluded that AB Dor is a zero-age-main-sequence star of spectral type K1.

AB Dor is listed in the Index catalogue of visual Double Stars (IDS, Jeffers et al. 1963) as a binary star with a separation of about $10''$. The visual companion Rst 137B (Rossiter 1955) is of spectral type M5 (Martín & Brandner 1995). Radial velocity measurements (Innis et al. 1986) and relative astrometry combined with proper motion measurements (Innis et al. 1986, Martín & Brandner 1995) confirm that Rst 137B and AB Dor form a physical binary, hence Rst 137B can be referred to as AB Dor B.

Due to the presence of AB Dor C, which is a close, low-mass companion to AB Dor A that was detected dynamically by Guirado et al. (1997), and recently resolved by Close et al. (2005), the AB Dor system is interesting in terms of calibrating theoretical models for young, low-mass objects. Since the mass of AB Dor C is known from the dynamical measurements, and the brightness is known from the resolved imaging, mass-luminosity relationships can be calibrated if the age of the system is known. This is however not a trivial issue, as is evident by the recent discussion in the scientific literature (see e.g. Close et al. 2005 – hereafter C05, Luhman et al. 2005 – hereafter L05, Nielsen et al. 2005, López-Santiago et al. 2006).

As suggested by Pakull (1981) and Rucinski (1985), precise age-dating of AB Dor B will yield a good determination of the evolutionary status of the AB Dor system as a whole. Here we present resolved NACO photometry of the two components of AB Dor B, allowing for placement of the individual objects in a color-magnitude diagram for comparison with theoretical and empirical isochrones. We use this to estimate an age range for the AB Dor system and apply it to AB Dor C. We compare our results to L05, in which a similar analysis was performed.

3.3 Observations and Data Analysis

Observations of AB Dor and its wide companion AB Dor B were obtained on Feb 05, 2004 with the adaptive optics instrument NACO at the ESO VLT UT4. The primary scope of the observations was a search for substellar companions, taking advantage of the newly implemented spectral Simultaneous Differential Imager (SDI, Lenzen et al. 2004). AB Dor B was also observed in direct imaging mode through broad-band H and Ks filters, and the

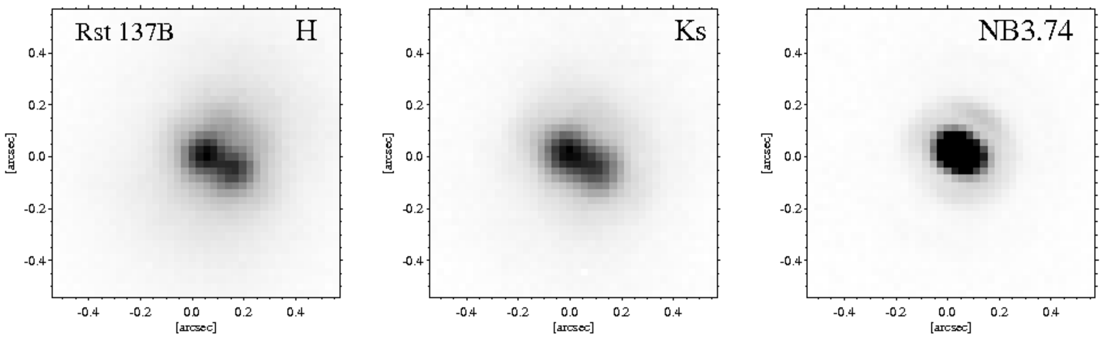

Fig. 3.1: NACO observations of AB Dor B in H and Ks broad-band and the NB3.74 narrow-band filter. The components of this close binary are resolved in H and Ks. North is up, east is to the left.

narrow-band NB3.74 filter, and clearly resolved as a close binary (see Fig. 3.1).

The binary parameters were obtained by an iterative fitting programme (see Bouy et al. 2003), using non-saturated exposures of AB Dor itself as a reference Point Spread Function (PSF).

Tab. 3.1: Relative astrometric measurements and brightness ratios Q for the Ab Dor B binary. Separation (Sep) and Position Angle (P.A.) were derived from fits to the resolved H- and Ks-band data.

Epoch	Sep. [mas]	P.A. [deg]	Q_{H}	Q_{Ks}	$Q_{\mathrm{NB3.74}}$
2004.098	66.1±1.1 [a]	238.5±1.3	0.79±0.01	0.78±0.01	0.79±0.02

[a] This corresponds to a projected separation of 0.99 AU for a distance of 14.94 pc.

3.4 Results and discussion

3.4.1 NACO data

The parameters of the resolved components of AB Dor B from the NACO observations are compiled in Table 3.1. The position angle and separation are based on a weighted mean of the parameters from each H- and Ks-band image where the weights were determined by the signal-to-noise ratio of each binary fit. Even though the H-band image is better resolved than the Ks-band image, the considerably worse Strehl ratio at H-band leads to a somewhat larger error in the brightness ratio Q than at Ks-band. At NB3.74, the binary is not entirely resolved. Thus for this case, we use the separation and position angle from H- and Ks-band as fixed parameters, and fit only for Q_{NB374}. A residual-weighted mean and error for Q_{NB374} was acquired by using the mean and extreme values respectively of the H- and Ks-band separation and position angle as input.

Note that the Ks-band brightness ratio given here is different from the one published in C05. This is likely due to the fact that Q does not always fully converge towards minimum residuals in the Bouy et al. (2003) code, if the input (first guess) Q_{in} is too far from the actual Q. In our case, for each image to be fitted, we have first tested a range of input values, and then manually fitted the image with a parameter range around the best-fit solution given by the automatic procedure, to ensure that it is indeed the actual minimum-residual solution. This mitigates the systematic errors of the Bouy et al. (2003) code, but it might be the case that some systematic errors remain due to errors in our reference PSF with regards to the 'true' PSF, in addition to the error bars given here.

3.4.2 Isochronal age

Due to the larger displacement of M-stars from the ZAMS than of higher-mass stars, and the better known age-luminosity relationship than for lower-mass objects, the AB Dor B binary components constitute the best candidates for isochronally dating the whole AB Dor system, especially with regards to theoretical isochrones. L05 did this by comparing AB Dor Ba and Bb to a sample of stars from the Pleiades in a $V - Ks$ versus M_{Ks} diagram. Since V is only measured for the unresolved binary, L05 inferred individual V-band magnitudes by assuming coevality and the same relation between ΔV and ΔKs as that of the empirical isochrone defined by the Pleiades sequence. While this analysis is in principle sound, a weakness of is obviously that it makes assumptions about a quantity that is not actually measured. In addition, the K-band brightness ratio in L05 is based on the value quoted in C05, which as we have mentioned is not the minimum-residual solution. Since we have presented here the brightness ratio also in H-band, we can improve on the analysis in L05. We use unresolved photometry in H- and Ks-band from 2MASS along with our brightness ratios to get individual H- and Ks-band magnitudes. We then compare the results to a Pleiades sample in a $H - Ks$ versus M_{Ks} diagram. Aside from the fact that all quantities are measured, there are several advantages of using colours $H - Ks$ over $V - Ks$: Both unresolved quantities were measured in the same survey, at almost the same time, and in addition, we can reliably compare the result with theoretical isochrones as well as empirical ones. While the models of Baraffe et al. (1998, commonly abbreviated as BCAH 98) give V-band magnitudes, they are known to correspond poorly to the actual values of these kinds of objects, whereas H- and Ks-band magnitudes are expected to be better suited (see e.g. Allard et al., 1997).

To represent the Pleiades, we use a sample of 33 M-type stars from Steele & Jameson (1995). The reason for this choice of sample is that well-constrained spectral types are given for all these stars in Steele & Jameson (1995), which is useful for further analysis as we will see below. 2MASS provides H- and Ks-band photometry for each of the targets. In addition, we include a low-mass sample from Barrado y Navascués (2004) to represent the young ($\sim$ 50 Myr) cluster IC2391, which is also used as an age reference in L05. A plot of these samples, AB Dor Ba, AB Dor Bb and the 50 Myr and 100 Myr isochrones from BCAH 98 are shown in Fig. 3.2. AB Dor Ba and Bb appear to be closer in age to IC2391 than to the Pleiades, though the scatters are large, and they are closer to the 50 Myr than the 100 Myr isochrone, though of course a whole range of ages is possible within the error bars, including equal age to the Pleiades. The theoretical isochrones do not seem to fit the lower-mass end of the empirical samples, but this is to be expected. Though AB Dor Bb appears to be bluer than AB Dor Ba, in contrast with expectation from the isochrones, this is well within the error bars, and so the assumption of coevality within the AB Dor B system appears to hold.

The sizes of the error bars and large scatter of the cluster samples evidently lead to an age that is poorly constrained. The reason that the errors are so large is that the brightness difference between H and Ks for low-mass stars is small compared to the photometric accuracy. Unresolved photometry in more separate wavelength bands would improve the accuracy of the result. Another factor that contributes to the uncertainty is the fact that the theoretical isochrones in $H - Ks$ are somewhat jagged, which creates a small uncertainty space around each age (as is clearly evident in Fig. 3.2). Also, the colors of K-stars in the Pleiades have been shown to be affected by effects such as rotation and activity (see Stauffer et al., 2003). While this issue has not been studied for M-stars, it is plausible that similar effects take place in that domain. Clearly, it would be favourable to introduce additional constraints. Thus, we use the spectral type as another measured quantity to further constrain the age of the AB Dor system. Since AB Dor Ba is brighter than AB Dor Bb, we assume that its spectral type corresponds closely to the spectral type of the unresolved AB Dor B. In Vilhu et al. (1991), a spectral type range for AB Dor B of M3 to M5 is given, but Martin & Brandner (1995) give a more well-constrained spectral type of M5 with errors of half a spectral type, and so we use the latter. Adopting this spectral type for AB Dor Ba, and using the same temperature scale as in Kenyon & Hartman (1995), we get a temperature range of 3145 to 3305 K (see the discussion related to this in the next paragraph). By translating the known Ks-band absolute magnitude of AB Dor Ba into a bolometric magnitude using the bolometric corrections for different spectral types given in Walkowicz et al. (2004) and matching to the temperature, we can constrain the age to a range where these quantities overlap. This gives an age range of $\log(t) = 7.5$ to almost 8.0, where t is the age in years, i.e. about 30 to 100 Myrs. The corresponding mass range is 0.13 to 0.2 M_{sun}. Assuming coevality and using the known Ks-band magnitude for AB Dor Bb, we get a mass range of 0.11 to 0.18 M_{sun} and a temperature range of 3080 to 3240 K, corresponding to spectral types M5 to M6. Note that it follows from this reasoning that the maximal sum of the component masses is 0.38 M_{sun}. This is consistent with the upper bound of 0.4 M_{sun} given in Guirado et al. (2006). Once the astrometry of all components of the AB Dor system initiated by that paper has proceeded far enough that the masses of all individual components are known, we can constrain the age even further. In this context, note that the astrometry point of the AB Dor Ba/Bb system in the Guirado et al. (2006) paper actually refers to Janson et al. (2007a), and that the astrometric fit has been improved since then (i.e., the values quoted here and in Janson et al. (2007a) should replace the corresponding values in the Guirado et al. (2006) paper).

A plot corresponding to the above reasoning is shown in Fig. 3.3. In addition, we include three additional stars (spectral type M3) from the AB Dor moving group (Zuckerman et al., 2004), as well as our empirical cluster samples in the same figure, after using the same procedure for finding the temperatures and bolometric luminosities. Comparing the samples, we see that AB Dor seems to be closer to the age of the IC2391 sample than the Pleiades sample, which is consistent with (and more secure than) the result of the color-magnitude diagram analysis. We also see that around the temperature range of AB Dor Ba and Bb, the means of the cluster samples seem to correspond fairly well to the expected isochrones – about 50-60 Myr for IC2391, and more than 100 Myr for the Pleiades. Note that the earlier-type stars seem to be significantly over-luminous, which is quite unexpected. The relative positions of the three groups in the diagram are however consistent for the entire range. As mentioned, we used the temperature scale of Kenyon & Hartman (1995). If we instead use e.g. the temperature scale of Leggett et al. (1996), the results are significantly different, since the Leggett et al. (1996) models predict a lower temperature for a given spectral type. Note that adopting such a temperature scale would lead to a significantly worse fit to the isochrones everywhere. In any case, regardless of what temperature scale is used, the relative positions of AB Dor, IC2391 and the Pleiades are the same, since the same scaling has been used for all the targets.

Finally, we plot the equivalent width of Hα against the $H-Ks$ color for AB Dor B, the three M3-stars in the AB Dor moving group, and the IC2391 sample in Fig. 3.4. L05 do this analysis for the Pleiades, and conclude that the AB Dor moving group can not be distinguished from the Pleiades in this regard. We find that the same can be said with respect to IC2391 – while the M3-stars of the AB Dor moving group do seem to lie near the lower edge of the IC2391 sample, AB Dor B itself is rather towards the upper edge. Hence, the overall view that AB Dor has a similar or somewhat older age than IC2391 holds also for this case.

In summary, our analysis indicates that the age of AB Dor lies between that of IC2391 and the Pleiades. As an upper limit on the age, we set the isochronal age of close to 100 Myr based on the Kenyon & Hartman (1995) temperature scale (if the Leggett et al. (1996) scale would be used, this upper limit would be lower). A meaningful lower limit can not be set by the theoretical isochrones due to the temperature scale issue, but since we have shown that AB Dor is not younger than IC2391, we set the lower age limit of AB Dor to be the same as the age of IC2391, which according to Barrado y Navascués (2004) is about 50 Myr. Hence, we end up with an age range of 50 to 100 Myr for AB Dor.

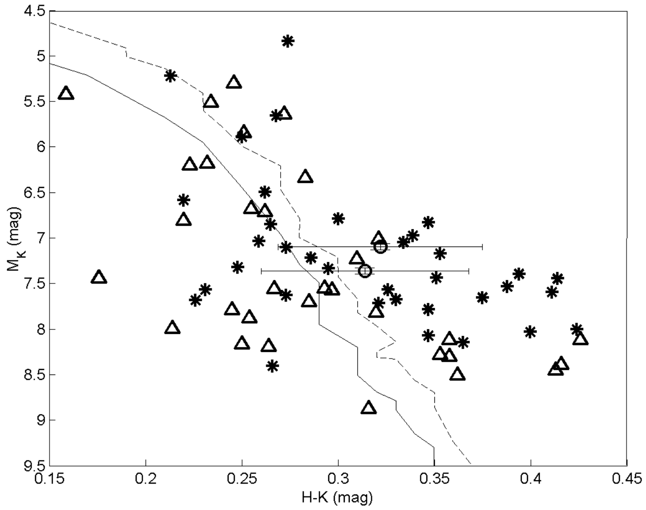

Fig. 3.2: Color-magnitude diagram with AB Dor Ba (upper circle) and AB Dor Bb (lower circle), a Pleiades sample from Steele & Jameson, 1995 (triangles), and an IC2391 sample from Barrado y Navascués, 2004 (asterisks). Two isochrones from BCAH 98 are also plotted – 50 Myr (dashed line), and 100 Myr (solid line).

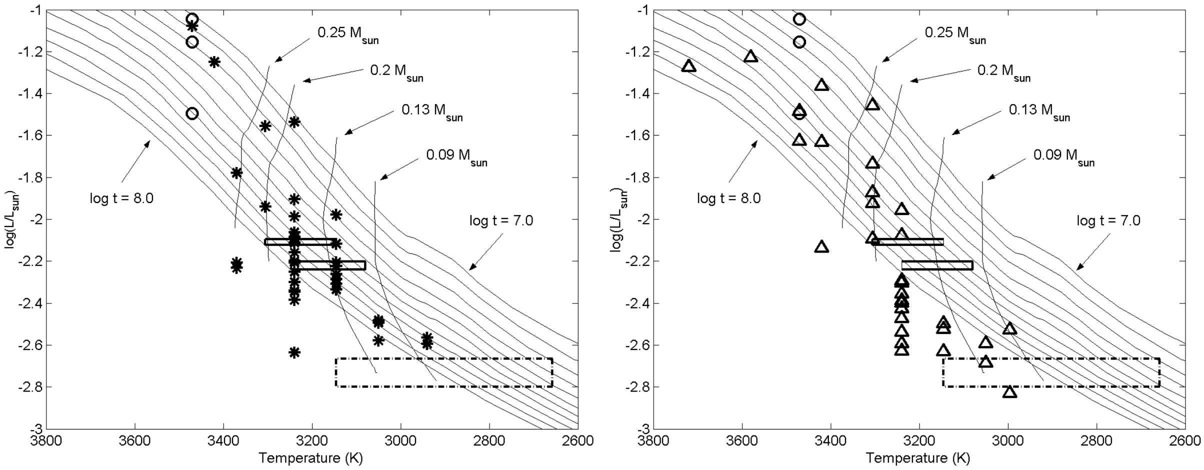

Fig. 3.3: Luminosity versus temperature for AB Dor Ba and AB Dor Bb (solid boxes). and the three M3-stars from the AB Dor moving group (circles). Left: Comparison with the IC2391 sample (asterisks). Right: Comparison with the Pleiades sample (triangles). Also plotted in both panels are mass tracks (units of $M_{\rm sun}$) and isochrones ($\log(t)$ changes by 0.1 per isochrone, t is in units of yr) from BCAH 98. For reference, AB Dor C is also plotted (dash-dotted box), but recall that the BCAH 98 models are not expected to apply to that kind of object. Note that the temperature of AB Dor Bb is not a measured quantity, but inferred from the assumed coevality with AB Dor Ba.

Tab. 3.2: Summary of photometry and derived physical parameters for AB Dor Ba and Bb.

Component	H [mag]	K [mag]	SpT	age [Myr]	mass [$M_{\rm sun}$]
Ba	8.29±0.04	7.97±0.03	M5	32-79	0.13-0.2
Bb	8.55±0.04	8.23±0.03	M5-M6	32-79	0.11-0.18

3.4.3 Kinematical group membership

L05 point out that the space motion of the Pleiades and AB Dor are remarkably similar – AB Dor and its moving group are among the $\sim$ 0.3% of the stars in the Nordström et al. (2004) catalog that are closest to the mean space motion of the Pleiades. From this, L05 draw the conclusion that the AB Dor moving group and the Pleiades were part of the same star formation event, and that they should therefore be roughly coeval. However, the relative spatial positions of AB Dor and the Pleiades are of course also of importance, since if two objects share a common spatial motion, but are too far separated to have originated from the same molecular cloud, their dynamical similarities are coincidental, or at the very least insufficient for assuming coevality. From the galactic coordinates (given by SIMBAD) and using the same distances as L05, we calculate the spatial positions relative to the sun and find that the Pleiades and AB Dor are separated by about 146 pc, whereas a giant molecular cloud is typically 50 pc across. However, if the small differential velocity vector points in the right direction, the objects might converge backwards in time to a common origin at a

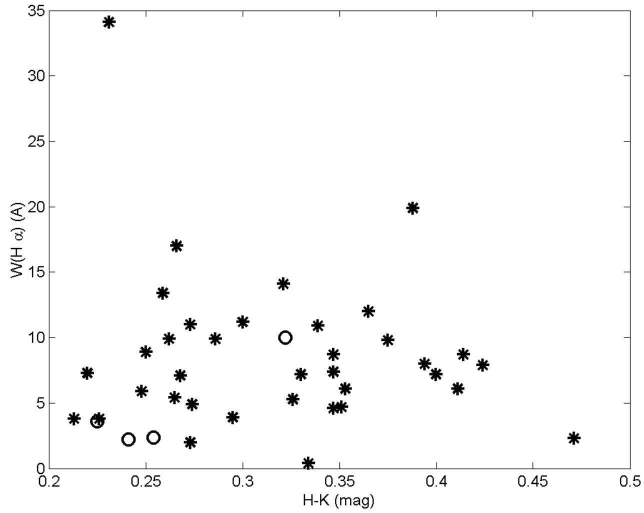

Fig. 3.4: Equivalent width of the Hα emission of AB Dor B (top circle), three M3-stars from the AB Dor moving group (circles), and the IC2391 sample (asterisks). Emission is represented by positive quantites in this case.

time corresponding to the birth of the Pleiades. To check whether this is the case, we use the same galactic space motion as L05 ($U = -7.7 \pm 0.4$ km/s, $V = -26.0 \pm 0.4$ km/s and $W = -13.6 \pm 0.3$ km/s for AB Dor and $U = -6.6 \pm 0.4$ km/s, $V = -27.6 \pm 0.3$ km/s and $W = -14.5 \pm 0.3$ km/s for the Pleiades), and calculate the positions at any given time from the present epoch positions, assuming constant velocities. We find that in fact, the objects diverge backwards in time from 30 Myrs ago such that at 125 Myrs ago, the separation was 260 ± 53 pc. In other words, if we assume the giant molecular cloud from which both objects hypothetically formed to be 50 pc across, we can seemingly exclude the hypothesis that they did form in the same cloud. However, note again that this assumes constant velocities over ~ 100 Myrs, which can by no means be guaranteed to have been the case (though note that if velocities are allowed to change over time, nothing can be strictly said about a common origin based on kinematics altogether).

In order to be more robust against changing velocities, it may be argued that using the AB Dor moving group as a whole rather than the AB Dor system alone is more relevant in the above argument. In this way, random accelerations of single objects are canceled out in a big enough sample with a common average motion. On the other hand, such an approach is risky, because misidentification of objects within the group may seriously affect the outcome. In particular, if AB Dor itself should happen not to be part of the AB Dor moving group, such an analysis would be completely irrelevant. Still, we perform this analysis in the same way as described above, adopting the same AB Dor moving group members as given in López-Santiago et al. (2006), with the same galactic space velocities. The result is that the distance between the center of the AB Dor moving group and the Pleiades is 129 pc today, and was 180 ± 58 pc at 125 Myrs ago. Thus the hypothesis that the two groups have separate origin is less secure in this case, but still the most plausible conclusion.

A surprising outcome of the analysis of space motion of AB Dor moving group members is that the differential motion of the individual systems with respect to the mean motion is in fact seemingly randomly distributed, rather than diverging from the center of the group as would be expected. This means that for instance, the mean separation between nearest neighbours is 17 pc at present, but would have been about 83 pc at 50 Myrs ago assuming constant velocities. Possible reasons for this behaviour are beyond the scope of this thesis; we simply note that if we trust the AB Dor moving group members to have a common origin, this speaks against using a single object (AB Dor) in a differential motion analysis, as in our first example.

The inevitable conclusion of this reasoning is nonetheless that, in particular for objects of larger separation than about 50 pc at present, common origin based on common motion is insufficient by itself, but has to be coupled with other criteria such as Hα emission or other common age indicators. In this context, we note that in contrast to L05, López-Santiago et al. (2006) confirm the conclusion of Zuckerman et al. (2004) that the AB Dor moving group is a distinct group with an age of 50 Myr, rather than being directly associated with the Pleiades (though Fig. 3 in their paper does seem to suggest that coevality could be possible).

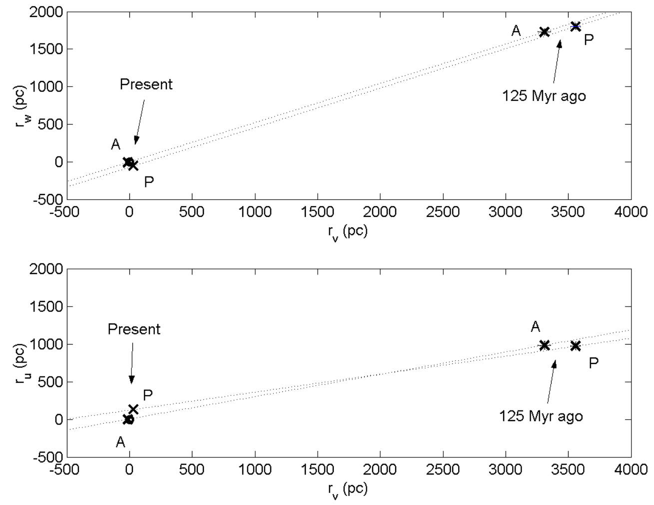

Fig. 3.5: Motions of AB Dor and the Pleiades (mean motion) assuming constant velocities. AB Dor is denoted by 'A', and the Pleiades are denoted by 'P'. r_{u}, r_{v} and r_{w} are the coordinates corresponding to U, V and W. The dotted lines are the spatial tracks relative to the sun over time. The circle at origin is the sun.

3.4.4 Consequences for AB Dor C

For comparing AB Dor C with theoretical models, we adopt the age range of 50 to 100 Myrs, and check independently the Ks-band absolute magnitude ranges given by C05 and Luhman & Potter (2006), i.e. $9.45^{+0.06}_{-0.075}$ mag and $9.79^{+0.25}_{-0.33}$ mag, respectively. For easy comparison with previous work, we use the evolutionary model of Chabrier et al. (2000). The result can be seen in Fig. 3.6. It is easily seen that while the C05 brightness range implies a possible overlap with the models for the higher part of the age range, only a very small part of the Luhman & Potter (2006) range is consistent with the models. In total, a minority of the parameter space is consistent with the models.

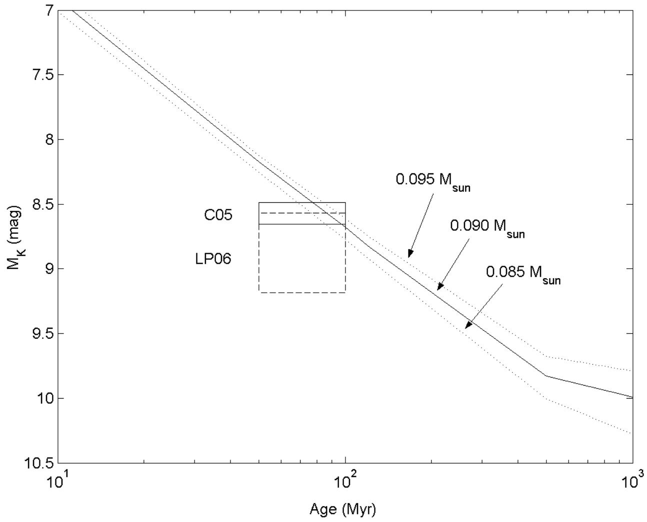

Fig. 3.6: Comparison of the measured and estimated quantities of AB Dor C to the Chabrier et al. (2000) model predictions. While there is an overlap between the measured brightness and the mass tracks for the given age, most of the parameter space implies that AB Dor C is fainter than what is predicted by the models. The solid box corresponds to the M_{Ks} measurements in C05, and the dashed box to Luhman & Potter (2006).

3.5 Conclusions

The age of the AB Dor system is fundamental for using AB Dor C as a calibration point for theoretical evolutionary models for young, low-mass stars. L05 use comparison of AB Dor B with empirical isochrones and kinematic analysis to determine that AB Dor is roughly coeval with the Pleiades, and has an age of 75 to 150 Myrs. With such an age range, AB Dor C has a mass-luminosity relationship which is consistent to what is predicted by the Chabrier et al. (2000) model. We conclude that the kinematic similarities between the Pleiades and AB Dor are insufficient to infer a common origin, and our comparisons with both theoretical and empirical isochrones imply a younger age range. A detailed comparison gives ages of 50 to 100 Myrs. Applying this age range to the case of AB Dor C, we find that while consistency with theoretical models is possible, the object more likely has a lower brightness than predicted by the models, if it is a single object. It has on the other hand been suggested that AB Dor C could be an unresolved binary (see Marois et al., 2005). If this turns out to be the case, AB Dor C may still be entirely consistent with the models.

The case of AB Dor and its role as a data point for calibrating the mass-luminosity relationship as a function of age for young, low-mass stars can be further constrained with additional measurements. Future work will include spatially resolved spectroscopy of the AB Dor B binary in order to better constrain the individual spectral types, and monitoring of the orbital motion in order to constrain the individual masses. Assuming a semi-major axis of ~1 AU and a system mass of ~0.375 M_{sun}, the orbital period is ~1.6 years, meaning that the orbital parameters should be readily measurable within a relatively short time-frame. Constraints can also be made with regards to AB Dor C – the photometry of AB Dor C can likely be improved, and radial velocity measurements of this component could be taken in order to determine whether or not it is in fact an unresolved binary.

CHAPTER 4

NACO-SDI DIRECT IMAGING SEARCH FOR THE EXOPLANET ϵ ERI B

From Janson et al. (2007b): AJ 133, 2442

4.1 Abstract

The active K2V star ϵ Eri hosts the most nearby known extrasolar planet. With an angular separation of about $1''$ on average, and an age of a few to several hundred Myrs, ϵ Eri b is one of the prime candidates for becoming the first definitive extrasolar planet imaged directly. We present a multi-epoch deep differential imaging survey performed with NACO-SDI at the VLT with the aim of finding the planet. The results are combined with recent astrometry in an attempt to further constrain the detection limits. No convincing candidate is found among the many coherent structures that constitute the residual speckle noise, which is the dominant noise at small angular scales. We present our detection limits, compare them with the estimated brightness of ϵ Eri b, and analyze how the limits can be improved further. It is found that integration time remains a very important parameter for achieving good results, even in the speckle-dominated regimes. The results yield new, improved upper 3σ limits on the absolute H-band (1.6 μm) brightness of the 1.55 $M_{\rm jup}$ companion of 19.1 to 19.5 mag, depending on the specific age of the system.

4.2 Introduction

As a consequence of the rapid progress in astronomical high-contrast imaging from the ground, following the development of adaptive optics (AO) along with employment of innovative differential imaging techniques, substellar companions that are cooler, less massive and at smaller separations can now be found than what was possible a few years ago. Examples of such detections are 2M 1207 B (Chauvin et al. 2005), and SCR 1845 B (Biller et al. 2006). Both of these objects in fact have planetary mass solutions within their error bars, but it should again be stressed that these error bars are based on theoretical mass-luminosity relationships that are, so far, poorly calibrated. A further discussion regarding such theoretical models in this context is performed in Sect. 4.5.2.

For a definitive detection of an extrasolar planet through direct imaging, one should preferably image an object which both has a low enough mass to be classified as such, and being close enough to its star that its actual mass can be determined by dynamical methods within a reasonable time frame. A particularly promising candidate system in this regard is ϵ Eri. A candidate planetary companion to the star ϵ Eri has been detected by radial velocity measurements (Hatzes et al. 2000). While the radial velocity signature by itself could in principle also be interpreted as being a result of the strong magnetic activity of ϵ Eri, it is important to note that if this was the case, one should also expect variations in the Ca II H&K emission with the same periodicity as the radial velocity signal (see Baliunas et al. 1995). Since no such correlation could be found, Hatzes et al. (2000) concluded that a planetary companion was the most probable cause of the observed radial velocity variations.

Subsequently, astrometry presented by Benedict et al. (2006) yielded further evidence for a planetary companion. By combining HST FGS astrometry with MAP astrometry (Gatewood 1987), and the radial velocity data from Hatzes at el. (2000) along with additional radial velocity measurements, Benedict et al. (2006) found consistent and statistically significant evidence for a planetary companion. Unfortunately, since the HST FGS astrometry has ceased operation, the astrometry does not cover the full orbit, which would further strengthen the conclusion of the existance of ϵ Eri b. Still, with the two different lines of evidence pointing to the presence of a planetary companion, ϵ Eri b is a significantly stronger candidate than the majority of extrasolar planet candidates known to date. On this note, it should also be pointed out that based on HIPPARCOS data, Wielen et al. (1999) mark ϵ Eri as a $\Delta\mu$ binary at the limit of detectability, which is consistent with a planetary mass companion around the expected separation of ϵ Eri b, yielding yet another piece of independent evidence for a planetary companion. Hence, throughout this chapter we will assume that the planet exists with the orbital configuration given in Benedict et al. (2006). In the event that ϵ Eri b, despite the evidence indicating otherwise, should not exist, the detection limits for other substellar companions around ϵ Eri as a function of separation from the primary can be read out from Figs. 4.10 and 4.11.

Benedict et al. 2006 give a mass of 1.55 $M_{\rm jup}$ for ϵ Eri b. The system is located just 3.2 pc away, making it the nearest extrasolar planetary system known to date. In addition, it has been estimated that the system is relatively young (at least within 0.1 to 1 Gyr, see Sect. 4.5.2), which is preferable from an observational point of view since at younger ages, the brightness contrast between the primary and secondary is smaller. Despite its youth, for the predicted age of this system and the measured mass of the planet, ϵ Eri b is expected to be significantly cooler than 700 K (based on the models of Baraffe et al. 2003), implying that it will exhibit strong methane absorption, which can be taken advantage of through spectral differencing. For these reasons, we have performed a multi-epoch observing campaign with state-of-the-art equipment and methods in an attempt to directly image ϵ Eri b. Very sensitive searches for planetary mass companions to ϵ Eri have been performed previously with Keck (Macintosh et al. 2003) and Spitzer (Marengo et al. 2006), but these searches aimed at the detection of more distant companions, and were sensitive only to separations of several arcseconds. Since the projected separation of ϵ Eri b as suggested by the dynamical measurements is always smaller than about 1.7", the survey presented here is the first one with a hypothetical possibility to detect this companion.

In this chapter, we present the results of these observations in combination with astrometric data, and discuss the limits this implies for the properties of ϵ Eri b. We also analyze the NACO-SDI data with the aim to find appropriate strategies for how to efficiently defeat the residual noise, which is a complex mixture of correlated and uncorrelated, dynamic and quasi-static noise contributions.

4.3 Observations

Our imaging observations of ϵ Eri were taken at four different epochs: (1) In August of 2003 during a commissioning run, (2) in September of 2004, (3) in August of 2005 and (4) in December of 2005 and January of 2006. All the images were taken with the NACO adaptive optics system at VLT (UT4) on Paranal, Chile.

At all epochs we used a combination of two differential imaging techniques: simultaneous spectral differential imaging (SDI) and angular differential imaging (ADI). For the purpose of SDI, narrow-band images were taken simultaneously in filters that we will refer to as F1, F2, and F3 which correspond to wavelengths of 1.575 μm, 1.600 μm, and 1.625 μm, respectively. For ADI, these observations were repeated at two different rotator angles (0° and 33°, respectively). The rationale behind these techniques is briefly discussed in Sect. 4.4. The epoch 4 data are spread over 3 weeks, which is a short period compared to the duration of the orbit – however, judging from the current best-fit astrometry, it appears that the companion is close enough to periastron at epoch 4 that it should be expected to move about 34 mas during this period. Hence, we should expect a slightly elongated image of the planet in the epoch 4 data due to its orbital motion in the 3 week period over which the data have been obtained.

For estimating the Strehl ratios of each of the frames, we used the coherent energy, which is a quantity that is measured automatically during all observing runs and stored in the image header. The details of conversion between coherent energy and Strehl are given in Fusco et al. (2004). For Strehl ratios higher than about 1 % in H-band (10 % in K-band), the coherent energy is a good approximation (the standard deviation is about 7.2 %) to the Strehl ratio at a wavelength of $\lambda_1 = 2.166$ μm (i.e., the measured coherent energy corresponds to the Strehl ratio at a wavelength of 2.166 μm, regardless of at which wavelength the measurements are taken). We can rescale this quantity to our working wavelength λ_2 by using the definition of coherent energy and the Maréchal equation, giving:

$$S_2^\star = \exp(\ln S_1^\star (\lambda_1/\lambda_2)^2) \tag{4.1}$$

where $S_1^\star$ and $S_2^\star$ are the coherent energies at wavelengths λ_1 and λ_2, respectively (note that coherent energies and Strehl ratios are usually given in percentages, but in this equation they must be put in as fractions of one, i.e., if the coherent energy is 30 %, the number 0.3 should be used). The average Strehl and other observation parameters are shown in Table 4.3 for all four epochs.

To enhance the detectability and strengthen the reliability of any companion that might be found in the images, we have incorporated astrometric data from mainly HST, complemented by MAP ground-based measurements. The astrometry is discussed in Benedict et al. (2006). The best-fit orbit is shown in Fig. 4.1.

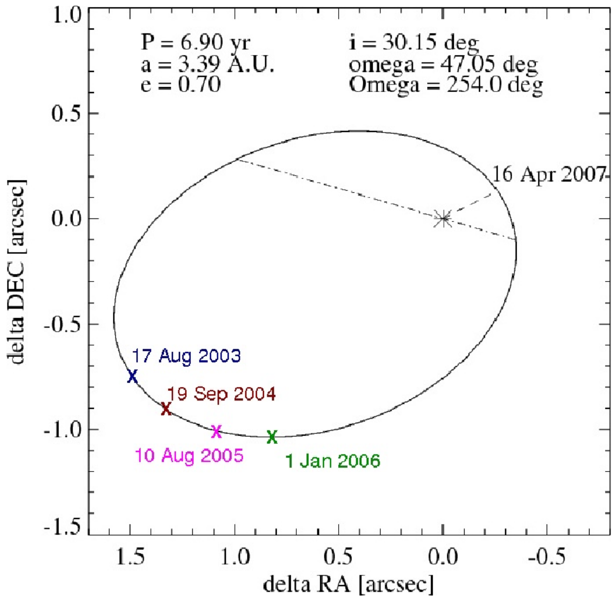

Fig. 4.1: Best-fit astrometrical orbit of ϵ Eri b around its parent star. The solid line marks the orbit, the dashed line shows the periastron, and the dash-dotted line shows the nodes. The approximate poisitions of the planet at each epoch of observation are also shown.

The specifics of the NACO system are detailed in Lenzen et al. (2003) and Rousset et al. (2003). In short, NACO is located in one of the Nasmyth foci of the VLT. It rotates around one axis to account for field rotation. The calibration of static aberrations is described in Blanc et al. (2003) and Hartung et al. (2003). No coronograph or other attenuation device was used for these observations. Flexures within the adaptive optics path of the instrument are not perfectly compensated – the rotation of the instrument causes small mis-alignments between the wavefront sensor subpupils and the deformable mirror. This leads to a Strehl ratio degradation, and most of the residual speckles, which are still present after SDI and ADI correction (see Fusco et al. 2005). Differential static aberrations, which are due to the different wavepaths at different wavelengths, are discussed in Brandner et al. (2004).

4.4 Data reduction

We primarily used a dedicated SDI/ADI data reduction pipeline (see Kellner 2005, for an extensive discussion – also, a very similar reduction scheme is detailed in Biller et al. 2004) for reducing the data. Each frame was background subtracted, flat-fielded and filtered with a bad pixel mask. The SDI was performed by subtracting F3 from F1 and F2 separately, after rescaling to a common λ/D scale. The common rationale behind SDI is that cool enough objects (T-dwarfs and giant planets) exhibit methane absorption, which results in an absorption band starting at about 1.6 μm and stretching towards longer wavelengths. For a stellar object, on the other hand, the spectral continuum is rather constant over this spectral range. Thus, in a system of a star with a substellar companion, the companion will appear much brighter in a 1.575 μm (F1) image than in a 1.625 μm (F3) image, whereas the star will be equally bright in both frames. By subtracting the latter image from the former, the companion will therefore remain largely unaffected in the difference frame, whereas the primary will be mostly canceled out. If the narrow-band images are taken simultaneously as in this case, removal of the stellar PSF includes attenuation of the halo speckle noise, which otherwise is by far the dominant noise source in high-contrast, low-separation imaging. For an object as low-mass as Eps Eri b, an additional factor plays in, in that additional absorption will start to decrease the brightness in F1 for increasing ages, such that Eps Eri b becomes equally bright in F2 as in F1, and eventually even brighter in F2 according to the Burrows et al. (2003) model (see Fig. 4.2). Hence, we use both the F1-F3 and F2-F3 difference images, so as to be optimally sensitive over a wide range of ages. We refer to Racine et al. (1999) for a more detailed discussion on speckle noise and SDI.

All SDI frames for each angle were then co-added to make use of the full integration time. Finally, the ADI was performed by subtracting the 33° data from the 0° data. The idea behind the ADI technique is that the telescope and instrumentation give rise to static aberrations in the final image – in particular, the SDI setup leads to non-common path aberrations since the light is split up for simultaneous imaging. However, when rotating the camera by e.g. 33° with all other set-ups being the same, a companion will rotate with respect to its primary by 33° in the resulting image, whereas the static aberrations should be unaffected. Thus, by subtracting two images at different angles, these aberrations will cancel out whereas the companion will remain with a very particular signature of one positive and one negative peak, at the same separation from the primary, but at a position angle differing by 33°. The principle is also known as roll deconvolution, and has been frequently used for, e.g., the HST (see Mueller & Weigelt 1987 and subsequent publications). ADI is also used by Marois et al. (2006), but with a somewhat different implementation, where images are taken at several different angles. Marois et al. (2006) get a noise reduction of about a factor of 5 for each image subtraction with such an implementation. Combining SDI and ADI with our implementation gives a noise reduction of 2 to 3 magnitudes, i.e. a factor of 6-16 improvement for each image subtraction (Kellner 2005). It would be an interesting experiment, as is suggested in Marois et al. (2006), to combine SDI with their implementation of ADI in order to possibly increase the sensitivity somewhat further.

While our three narrow-bands in principle allow for multi-wavelength image subtraction in the manner described by Marois et al. (2000), this cannot be applied in practice, due to the

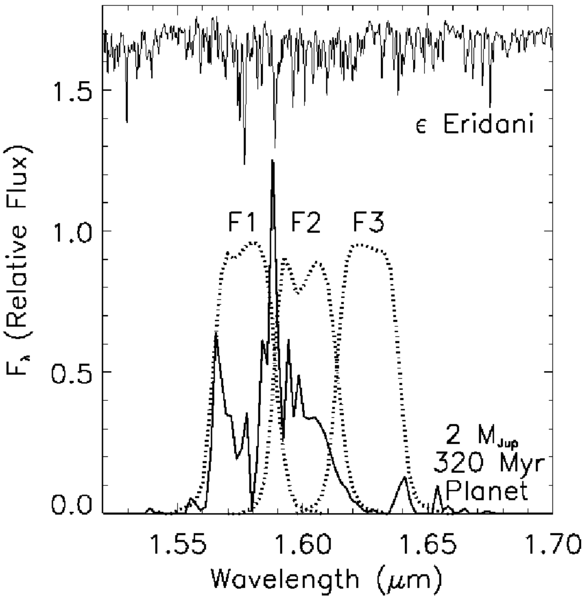

Fig. 4.2: Filter transmission curves of narrow-band filters F1, F2, and F3, along with the spectral distribution of ϵ Eri A from Meyer et al. (1998) and a theoretical spectrum from Burrows et al. (2003), similar to what would be expected from ϵ Eri b. The flux of ϵ Eri A is essentially uniform over the whole range, whereas the flux of the companion is strongly concentrated within the range of F1 and F2, according to theoretical models. The relative fluxes of the star and planet are not to scale.

fact that static or quasi-static aberrations are present in the data, which were not considered in Marois et al. (2000). The static aberrations influence the k-factor derived in Marois et al. (2000) and prevent any increase of quality from this method. For future instrumentation with possibly smaller static aberrations, this technique may be highly interesting to add to the combination of differential imaging methods.

Given that the final output is strongly affected by the Strehl ratio of individual frames, it is not a given fact that co-adding as many frames as possible will necessarily add up to the best possible result. In some cases, it is instead preferable to de-select frames with a bad Strehl ratio if they do more harm than good to the final frame. We therefore performed a number of tests to determine the optimal selection of frames. This was done by sequentially (and cumulatively) de-selecting the frames with the lowest measured Strehl ratio and checking the quality. The quality criterion was a minimization of the average error in the area between 20 and 80 pixels away from the star, divided by the average Strehl ratio of the sample in order to take into account the fact that the brightness of a hypothetical companion PSF core would be proportional to the Strehl ratio. The error was quantified by the standard deviation in a 9x9 pixel area around each pixel. For epochs 1 and 2, we found that no substantial improvement could be gained by excluding frames from the full set. For the epoch 3 data, we found that a de-selection of the four worst frames (in terms of Strehl ratio) per angle gave the best overall quality, and therefore we used the resulting set for further analysis. For the epoch 4 data, a slight error during observation led to three more frames for the 33° data set than for 0°. It is preferable that the number of frames is the same at both orientation, so that the noise impact is equal during subtraction. For this reason, we de-selected the three worst frames for 33° to begin with. Subsequent analysis in the same manner as for earlier epochs led to the conclusion that the best quality was reached by keeping all remaining frames in the final selection.

4.5 Results and discussion

4.5.1 Analyzing the images

The reduced images are shown in Fig. 4.3 for F1-F3, and Fig. 4.5 for F2-F3. To enhance the conditions for visual inspection in the interesting areas, the central areas have been set to zero. While there is meaningful information in most of these areas, the fluctuations are much larger, and detection of a planetary mass companions is therefore not possible there. Also, a few of the central pixels are normally saturated in the raw images, hence no meaningful information is available at the very center (within about 5 pixels). Zoomed-in versions of the most interesting areas from an astrometric point of view are shown in Figs. 4.4 and 4.6. The main problem of finding a faint companion in the final data is readily seen in those images: the correlated residual speckle noise forms a vast number of coherent structures in the image space, which mimic the appearance of a physical companion. The ADI is however a great help in this regard. A real companion has to leave an imprint of one positive and one negative structure in the image, where both structures are at the same separation from the center of the stellar PSF (the position of which must of course be saved during the data reduction, since the PSF is canceled out in the difference images). The negative peak has to be separated from the positive one by 33° clockwise. Still, the centers of the respective companion peaks, as well as the center of the stellar peak, can not be determined with infinite precision. Thus, there will remain several false positives in the images since the speckles are common enough that a negative speckle will, by chance, end up close enough to the right position relative to a positive speckle in several cases. 'Negative' and 'positive' speckle in this context denotes a coherent residual structure, from atmospheric or instrumental aberrations, which is brighter in one frame than the other during either of the differencing stages – i.e., in the difference image $a - b$, a speckle becomes positive if it is brighter in a than in b, and vice versa.

The 3σ narrow-band detection limits per pixel of each epoch are shown in Fig. 4.7 for F1-F3, and Fig. 4.8 for F2-F3. The limits are based on the median of the statistical errors at the various radii. We will discuss what they correspond to physically in Sect. 4.5.2. It can be seen by comparing those figures, as well as the visual quality of the images, that F1-F3 produces somewhat higher qualities than F2-F3 on average. With respect to the images, the limits are such that several candidates exist with fluxes above the 3σ limit. However, as we have already alluded to, this is not sufficient to claim a detection. The detection limits are useful as they give a general view of the sensitivity of the data, but when dealing with speckle noise, it is necessary to have additional constraints to the 3σ threshold that can be used for detection when limited by uncorrelated noise. This is due to the fact that the residual errors are not Gaussian, and hence 3σ does not correspond to the well known 99.7 % detection confidence (a discussion on the relationship between standard deviation and detection probabilities in the context of speckle noise is performed in Marois et al. 2008). One such constraint can be to demand that the candidate clearly dominates the speckle noise, i.e., to set an extremely high threshold such that no single speckle could be bright enough to mimic the appearance of such a companion. Another way to constrain the data is to incorporate a priori information about the properties of the companion that a given candidate has to match (as has, e.g., been done for GQ Lup b, see Janson et al. 2006). Since there is no candidate that dominates the flux by an extreme amount (though some candidates are of course stronger than others in this regard, see e.g. Kellner et al., in preparation), we try the latter alternative.

As we have mentioned, radial velocity and astrometry data exist that we can use to determine the orbit of ϵ Eri b, and thus its position relative to ϵ Eri at any given epoch. Using the orbital parameters, and using a mass estimate of Benedict et al. (2006) for ϵ Eri ($0.83 M_{\mathrm{sun}}$), we find separations and position angles for ϵ Eri b as compiled in Table 4.1 for each epoch at which our images were taken. The results are also overplotted in Figs. 4.3 to 4.6. Errors in separation and position angles are derived by generating 10^4 orbits with random errors for the orbital parameters set by the values given for the errors in Benedict et al. (2006), and calculating the resulting standard deviations in separation and position angle at each of the expected positions of ϵ Eri b. The error boxes can be used for excluding a large amount of false positives. Since we have multiple epoch data, we can also in principle acquire a robust detection of a real object – if a candidate shows up with its positive and negative signatures in the right places during all epochs, we can calculate the probability that this would happen by chance with speckles, which will give us a meaningful statistical basis on which to confirm (or not confirm) the detection of a companion. The statistical analysis could for instance be done in the following way: Within a circular zone with inner and outer radii set by the known separation from astrometry with error bars, a number count is done of positive and negative speckles above a certain threshold. Based on this and the area of the zone, we can calculate the probability that a positive speckle ends up within its astrometric error bars, and that a negative speckle simultaneously ends up within its corresponding error bars (which is a subzone within the circular area, limited by the error bars in position angle). This probability can be calculated for each epoch, and by multiplying these probabilities, a final probability is acquired which can be required to be, e.g., less than 1 %. In our case, the error bars are not sufficiently well-constrained that a meaningful analysis can be done in such a manner (i.e., the areas are large enough that speckles can not be excluded with sufficient confidence). This can however be significantly improved upon with further astrometric monitoring.

Tab. 4.1: Expected separation and position angle for each epoch from the astrometry of Benedict et al. (2006).

Epoch	Date	Sep. (arcsec)	P.A. (deg)
1	17 Aug. 2003	1.68 ± 0.18	114 ± 8
2	19 Sep. 2004	1.55 ± 0.18	129 ± 8
3	10 Aug. 2005	1.27 ± 0.15	144 ± 8
4	1 Jan. 2006	1.09 ± 0.13	155 ± 9

In summary, we do not detect any sufficiently significant candidates in the data to claim a detection of ϵ Eri b, though with additional dynamical data, the images may still be useful in this regard.

4.5.2 Detection limits

In the previous section, we presented the statistical errors of each epoch (Figs. 4.7 and 4.8). We can use these errors to estimate detection limits in observational terms (narrow-band brightness contrast). Then, by inferring theoretical evolutionary models, we can formulate them in more physically relevant terms. The observational narrow-band detection limits are, of course, directly available from the figures. It can be seen that overall, epoch 4 in F1-F3 provides the most sensitive data. In this case, at 0.5", a contrast of about 10.5 mag can be reached between primary and secondary, and at 1.0", a contrast of almost 12.5 mag can be reached. At about 1.5" and outwards, we reach a contrast of 13 mag. However, if we take the best-fit astrometry into account, we see that for ϵ Eri b, epoch 4 actually provides the least sensitive data point, with a contrast of about 12.4 mag. Epochs 1 and 3 are somewhat better with about 12.6 mag in both cases. The most sensitive measurement according to the astrometry is clearly the epoch 2 data, providing a contrast of $\sim$ 13.1 mag.

The astrometry provides a unique mass for ϵ Eri b of about $1.55 M_{\rm jup}$ (Benedict et al. 2006). To get a handle on whether we could expect to detect the planet in our data, we can translate the mass into a brightness using the theoretical mass-luminosity relationships of Baraffe et al. (2003) as a function of age. In this context, we wish to carefully remind the reader that such relationships are hugely uncertain for such low-mass objects, in particular for young ages. Indeed, comparison of the measured brightness and the dynamical mass of the young star-BD boundary object AB Dor C seems to imply that the theoretical models overestimate the luminosity corresponding to a given mass for such objects (see Close et al. 2005). However, this is based on an age estimate which has been questioned, and is a matter of discussion (see e.g. Luhman et al. 2005 and Janson et al. 2006). Also, there may be differences between properties of objects undergoing significant accretion, and objects which do not. Accretion is not considered in the Baraffe et al. (2003) models, but is a fundamental mechanism in the case of planet formation by core accretion. Marley et al. (2007) present models which do take this effect into account, and find that they differ drastically in predicted properties from collapse without accretion. However, for objects near $1 M_{\rm jup}$, such as ϵ Eri b, the discrepancy has vanished already at $\sim$ 10 Myr. In any case, we assume that the Baraffe et al. (2003) model applies, which gives results summarized in Table 4.2.

Tab. 4.2: Expected H-band brightness contrast between ϵ Eri A and b for different ages, from the Baraffe et al. (2003) models.

Age	Contrast	Planet temp.	Planet radius
10 Myr	12.5 mag	640 K	0.135 $R_{\rm sun}$
50 Myr	15.5 mag	430 K	0.123 $R_{\rm sun}$
120 Myr	17.4 mag	350 K	0.118 $R_{\rm sun}$
500 Myr	22.9 mag	240 K	0.111 $R_{\rm sun}$
1 Gyr	26.0 mag	190 K	0.108 $R_{\rm sun}$

For a fair comparison with our achieved contrasts, we translate the narrow-band contrasts given above into H-band contrasts. Such a procedure was first presented for T-dwarfs by Biller et al. (2006). However, since we know the mass of ϵ Eri b, we can do a much more specific analysis for this case. Using spectral models of Burrows et al. (2003), we calculate the offset $\Delta_{\rm mag}$ between F1 and H as:

$$\Delta_{\rm mag} = -2.5 \log_{10}(Q) \tag{4.2}$$

$$Q = \frac{\frac{\int f_\lambda g_{\rm F1} d\lambda}{\int F_\lambda g_{\rm F1} d\lambda}}{\frac{\int f_\lambda g_{\rm H} d\lambda}{\int F_\lambda g_{\rm H} d\lambda}} \tag{4.3}$$

where f_λ is the spectrum of the planet, F_λ is the spectrum of the star, $g_{\rm F1}$ is the filter transmission of F1, and $g_{\rm H}$ is the filter transmission of H. An equivalent equation is valid for F2. The resulting offsets are plotted in Fig. 4.9 for ages of 100 Myr to 1 Gyr. It is clear that for young ages, F1-F3 is better suited for finding an object such as ϵ Eri b, whereas for older ages, F2-F3 is more appropriate. We show the calculated H-band contrasts in F1-F3 at 100 Myr in Fig. 4.10, and in F2-F3 at 1 Gyr in Fig. 4.11. The contrasts reached at the expected separation of Eps Eri range from about 14.5 mag (epoch 4) to about 15.1 mag (epoch 2), and imply that we could expect to detect ϵ Eri b with 3σ confidence if the age is close to 50 Myr or younger, if the models are to be trusted. With an H-band brightness of 1.9 mag for the primary, and a distance modulus of about 2.5 mag, the epoch 2 data leads to a limiting absolute brightness of 19.5 mag for ϵ Eri b, though for ages between 100 Myr and 1 Gyr, the narrow-band to H-band offset is smaller, such that the minimum brightness limit is 19.1 mag for some ages in that regard.

Age estimates of ϵ Eri in the literature are quite divergent (see e.g. Song et al. 2000, Fuhrmann 2003, Decin et al. 2003, Saffe et al. 2005, and Di Folco et al. 2004), but seem to consistently yield ages larger than 100 Myr, and smaller than 1 Gyr. Thus, we conclude that we should not expect to detect the planet by 3σ in any of the images. We note, however, that there may be other aspects to the problem that are not included in the above reasoning. Aside from that the models may mis-predict the brightness by an unknown factor due to the uncertain initial conditions, the brightness could also be affected by factors that are not included in the evolutionary models of Baraffe et al. (2003). A potentially interesting factor in this regard is interaction between the planet and a remnant debris disk. A debris disk has indeed been observed around ϵ Eri (see e.g. Greaves et al. 1998). Frequent collisions between the planet and the planetesimals in the disk would heat the outer atmosphere of the planet, temporarily leading to a substantial brightening. Since the magnitude of the effect depends on the frequency of collisions, and the conditions of the disk are poorly known, the magnitude of this effect is however difficult to determine.

Finally, we note that when surveying for the planets with constrained astrometry over several epochs as described in Sect. 4.5.1, the 3σ condition of the companion flux with respect to the source becomes less meaningful. Since in that case, the probability threshold is set by number counts of speckles, a source can be detected with a sufficient confidence in total, even though it may be less bright than the threshold set for a 3σ detection for brightness within a single frame. As an example, we hypothesize that in each of four images, a 2σ signature shows up within well-constrained astrometric error bars with both a signature of positive and negative counts in the right places. In none of the single cases, a detection can be claimed with any significant probability. However, we now assume that the probability of a $\geq 2\sigma$ speckle ending up in the right places of a single image by chance is the same for all images, and can be estimated to be, say, 10 %. The events in the four different images are independent, hence the total probability that the detection is false is $0.1^4 = 10^{-4}$. Hence in such a situation, a detection could be claimed with a sufficient confidence in total.

4.5.3 Error analysis

The noise in the final images is a complex mixture of dynamic and quasi-static, correlated and uncorrelated noise, with different relative impacts in different parts of the image. Correlated noise has a greater relative impact at small angular separations from the star, whereas the opposite is true for uncorrelated noise. The relative importance of these noise sources vary with varying observing conditions, such as the seeing. An analytical description of dynamic speckle noise versus uncorrelated noise sources (photon, read, and sky noise) is given in Racine et al. (1999), but quasi-static speckle noise, which is a major contributor to the noise in real applications, is not considered there. Other approaches for dealing with speckle noise based on, e.g., Goodman (1975) exist – for instance, in Aime & Soummer (2004). A method for using such an approach in practice is detailed in Fitzgerald & Graham (2006). However, this methodology can not be well applied to NACO-SDI for atmospherical speckle noise, since it relies on getting a very large amount of very short exposures for statistical analysis. In the case of NACO-SDI it is essential to keep the integration time per exposure as large as possible, in order to minimize overhead time and read noise. For quasi-static speckle noise with timescales of a few seconds or larger, a similar technique could in principle be applied in the future, if the observing strategy is adapted appropriately. In general, the complexity of the noise makes it difficult to estimate a priori the observing conditions needed to reach a certain sensitivity for a certain source, when planning surveys for, e.g., extrasolar planets.

In three of our epochs (2, 3, 4), we observe the same source, with the same instrument, the same detector and very similar observing strategies. Thus, we have a rather large amount of data where we can empirically test the quality of our data as a function of observing conditions, where all other parameters can be kept rather constant. Here we will perform an analysis of the normalized error e as a function of Strehl ratio, and integration time: $e = \xi / S$ where ξ is the average error, and S is the Strehl ratio. The reason we divide by the Strehl ratio is the same as in Sect. 4.4: the Strehl ratio is proportional to the signal strength of a companion, and hence $e \sim SNR^{-1}$. Since the noise properties will vary with radial distance from the center of the remnant stellar PSF, we examine e in four different zones separately: zone 1 is defined as the area between 0 and 19 pixels radially from the center, zone 2 as the area between 20 and 39 pixels, zone 3 between 40 and 59 pixels, and zone 4 between 60 and 79 pixels. Since the pixel scale of the NACO-SDI is 17.32 mas/pixel (see Brandner et al. 2004 for how this is determined), this corresponds to angular separations of about 0.0-0.3 arcsec for zone 1, 0.3-0.7 arcsec for zone 2, 0.7-1.0 arcsec for zone 3, and 1.0-1.3 arcsec for zone 4.

Strehl ratio dependence

To examine e as a function of Strehl ratio, every individual 0° frame within one epoch is coupled with every 33° frame within the same epoch, and the full data reduction is performed for each pair of frames. The average e is then plotted against the average S for each pair in each zone. The plots are shown in Figs 4.12 through 4.14. The dispersion is large, but fortunately, we have a lot of data points, and so the trend is very clear: $e \sim S^{-1}$, i.e. $SNR \sim S$.

As expected, the examination shows that Strehl ratio is an important parameter for optimizing the sensitivity when searching for substellar companions. The trend of $SNR \sim S$ is consistent for all three epochs, and over all four zones. Thus, doubling S will generally lead to a doubling of the SNR, regardless of where in the image a hypothetical companion may be situated. Since our Strehl ratios are within the range of about 20 % to 40 % in H-band, it is of course not possible to predict whether this trend holds also for extremely high (or low) Strehl ratios. However, within the range of what can be reached with present instrumentation, it is clear that aiming for the highest possible Strehl ratio is indeed a good strategy.

Integration time dependence

For finding the dependence of e on the effective integration time t, each 0° frame within one epoch is paired with one 33°. The pairs are then sorted sequentially in groups of more and more pairs, and the groups are submitted to the full data reduction – i.e., first groups of one pair per group are formed and reduced, then groups of two pairs per group are formed, then three pairs per group and so on. The average e for a certain number of pairs per group is then plotted against the number of pairs per group. This is shown in Figs. 4.15 through 4.17.

To interpret the results of the examination, we need to know the behaviour of the noise sources in the data. As we have mentioned previously, the residual noise in double-differenced (SDI and ADI) data is a mixture of correlated and uncorrelated, dynamic and quasi-static noise. Photon noise and read noise are dynamic and uncorrelated noise sources whose characteristics are well known and easily estimated. They average out with time (for co-added exposures) as $e \sim t^{-1/2}$. Flat field noise is a multiplicative noise source which is static with respect to the detector, but mainly uncorrelated in space. It does not average out with the total number of exposures, but with the amount of different dither positions (five, in our case). It is also completely differenced in the ADI for the cases where the dither positions are the same at 0° as at 33° (with respect to the center of the PSF). The speckle noise is correlated, and ranges from dynamic to quasi-static. For speckle noise, $\sigma_{\mathrm{s}} \sim n_{\mathrm{s}}^{-1/2}$, where σ_{s} is the standard deviation of the speckle noise and n_{s} is the number of speckles per unit area (see Racine et al. 1999; also, see Sivaramakrishnan et al. 2002 for a specific discussion on time dependence). Thus if the speckle lifetime τ_{s} is shorter than the integration time of a single exposure (t_{exp}), averaging the exposures will yield that $\sigma_{\mathrm{s}} \sim t^{-1/2}$, i.e., the component of the speckle noise that varies on such timescales will average out according to the square root law just as for the other dynamic noise sources, because a completely new speckle pattern will be generated in each exposure, such that the number of speckles increases linearly with integration time. Note that it makes no difference that the noise is spatially correlated in this regard – on a frame-to-frame basis, it will obey Poissonian statistics and average out just like spatially uncorrelated noise. If $\tau_\mathrm{s} > t_\mathrm{exp}$, the noise impact will decrease more slowly. In the extreme case where $\tau_\mathrm{s} > t_\mathrm{tot}$ (where t_tot is the total integration time), the same speckle pattern will be generated in every exposure, hence n_s is constant, and thus σ_s is the same independently of integration time. The noise in the latter case, which represents completely static noise with respect to the observations, should in general be differenced out by SDI and ADI, but noise which is constant in time, but varies in both wavelength and rotation angle of the instrument, could in principle remain in the final data.

It is clear from the images of ϵ Eri (Fig. 4.3) that the total noise is dominated by correlated noise for most parts of the observed parameter space. This can also be seen in Figs 4.18 through 4.20, where we have computed the expected photon noise, flat field noise and read noise for each observation, and plotted along with the actual noise for epochs 2, 3, and 4. We see that indeed, the uncorrelated noise is dominated by other noise sources. The photon noise and read noise are strongly dominated in the inner parts, and start to become significant only in the outer parts. The flat field noise is dominated by about the same factor everywhere, which implies that the dominating noise has the same flux dependence as flat field noise – i.e., that the dominating noise is linearly proportional to the local flux, which indeed is the case for speckle noise (see Racine et al. 1999 and Aime & Soummer 2004 for halo-dominated images).

Returning to the analysis of the noise trend as a function of time in our real data (Figs 4.15 through 4.17), we see that the general trend is a drop which is slightly slower than $e \sim t^{-1/2}$. This is considerably better than expected, and implies that a large fraction of the residual speckle noise has a short lifetime. Obviously, since the speckle noise with the shortest lifetimes will cancel out faster than the more long-lived components, the residual noise will gradually be more and more dominated by quasi-static noise until a noise floor is hit and no further improvement can be gained in terms of integration time. Judging from the curves, that point is however still quite far off. It is particularly interesting that e still drops off close to the $t^{-1/2}$ rate in the epoch 4 data, after about 1.5 hours effective integration time per angle. This implies that a yet higher sensitivity can be reached by simply integrating for a longer time, as long as the other observing conditions are acceptable.

In reference to future strategies related to NACO-SDI imaging, it is clear that a large amount of integration time is favourable. In particular, if the position of the suspected companion is known a priori, as will henceforth be the case for ϵ Eri b, this is best done by increasing the integration time of individual exposures (DIT), since this minimizes the readout time, and is more efficient for mitigation of read noise. In the general case, where no such a priori information is available, the DIT is always conservatively set such that the primary PSF will ony saturate slightly, in order to maintain an as small inner working angle as possible. However, if the separation is known, the DIT can be set such that the primary PSF saturates over a large area, as long as this area is well within the expected separation. Of course, in such a case, considerations should also be taken about whether there may be additional interesting companions within the separation of the known companion.

4.6 Conclusions

We have performed a multi-epoch study of ϵ Eri with NACO-SDI at the VLT, and combined it with astrometry in order to try to detect its planetary companion, ϵ Eri b. Despite excellent H-band contrasts of 14.5 to 15.1 mag at the expected positions of ϵ Eri b, and limiting absolute magnitudes of 19.1 to 19.5 mag, we did not detect the companion. A theoretical assessment of the brightness based on the mass of ϵ Eri b, and the plausible age range of the ϵ Eri system, indicated that a non-detection might perhaps indeed be expected, though such an analysis is necessarily vastly uncertain. With a more well-constrained astrometry, even better detection limits may be possible to achieve from the existing data, through speckle number-count statistics over all four epochs.

In addition, the detection limits as a function of Strehl ratio and integration time have been examined. It has been found that the signal-to-noise ratio scales linearly with the Strehl ratio, which shows that it is of significant importance to maintain a high Strehl ratio during companion searches. A surprising result was reached in the case of detection limit dependence on integration time. The signal-to-noise ratio was found to scale almost according to the well-known square-root dependence for standard noise sources. This means that it may be possible to detect much fainter objects by simply increasing the integration time for a given target. Consequentially, we conclude that with a sufficient amount of effort, objects like ϵ Eri b may be detectable with the presently available telescopes and instrumentation.

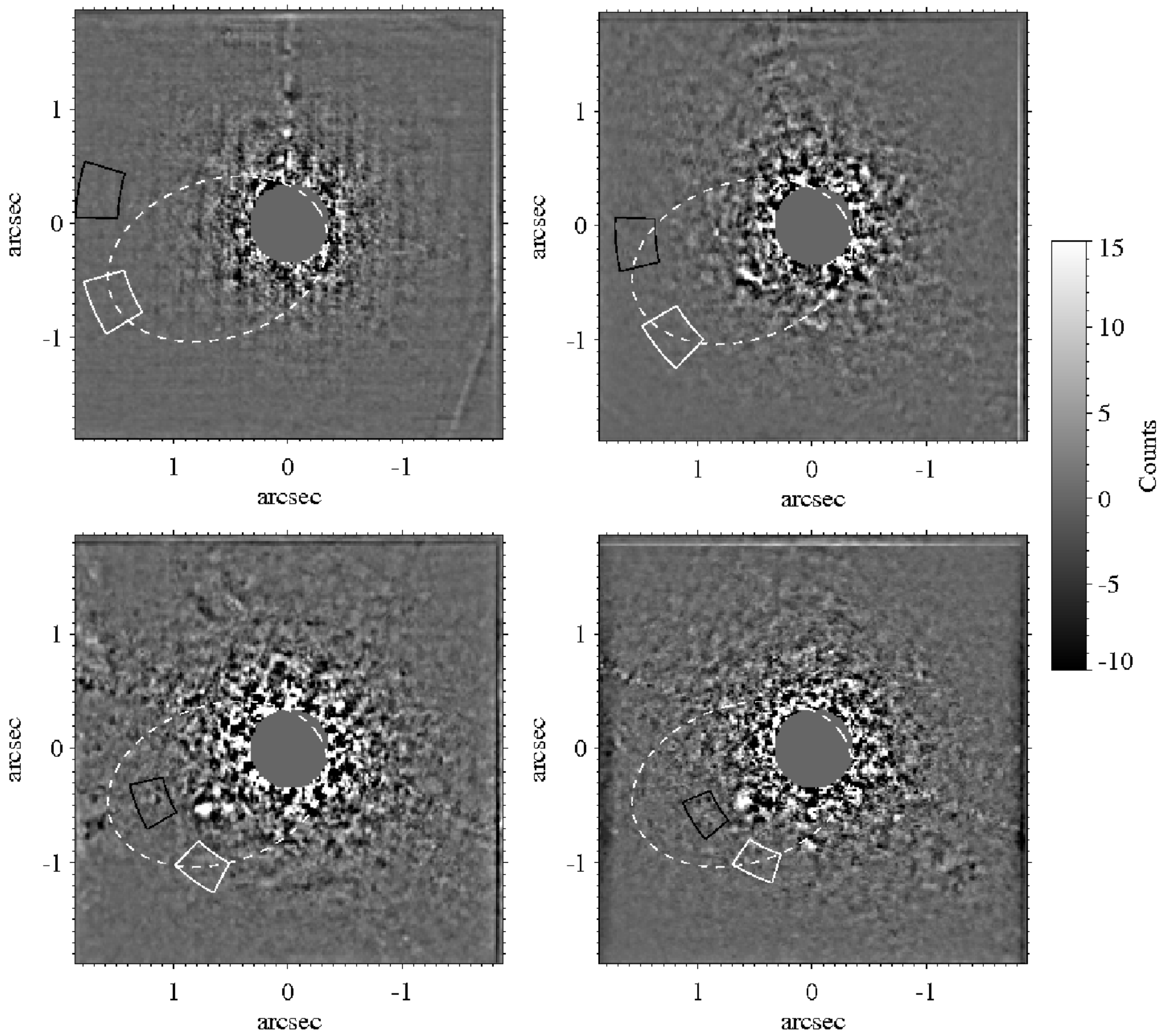

Fig. 4.3: The output F1-F3 images from each of the observations in sequence. Upper left: Epoch 1, 17 Aug 2003. Upper right: Epoch 2, 19 Sep 2004. Lower left: Epoch 3, 10 Aug 2005. Lower right: Epoch 4, 1 Jan 2006. The dotted line marks the best-fit orbit from astrometric and radial velocity data. The areas enclosed by white and black borders are error boxes for the expected positions of the bright and dark signatures of the companion, respectively. In all of the images, north is up, and east is to the left. All the counts are per pixel.

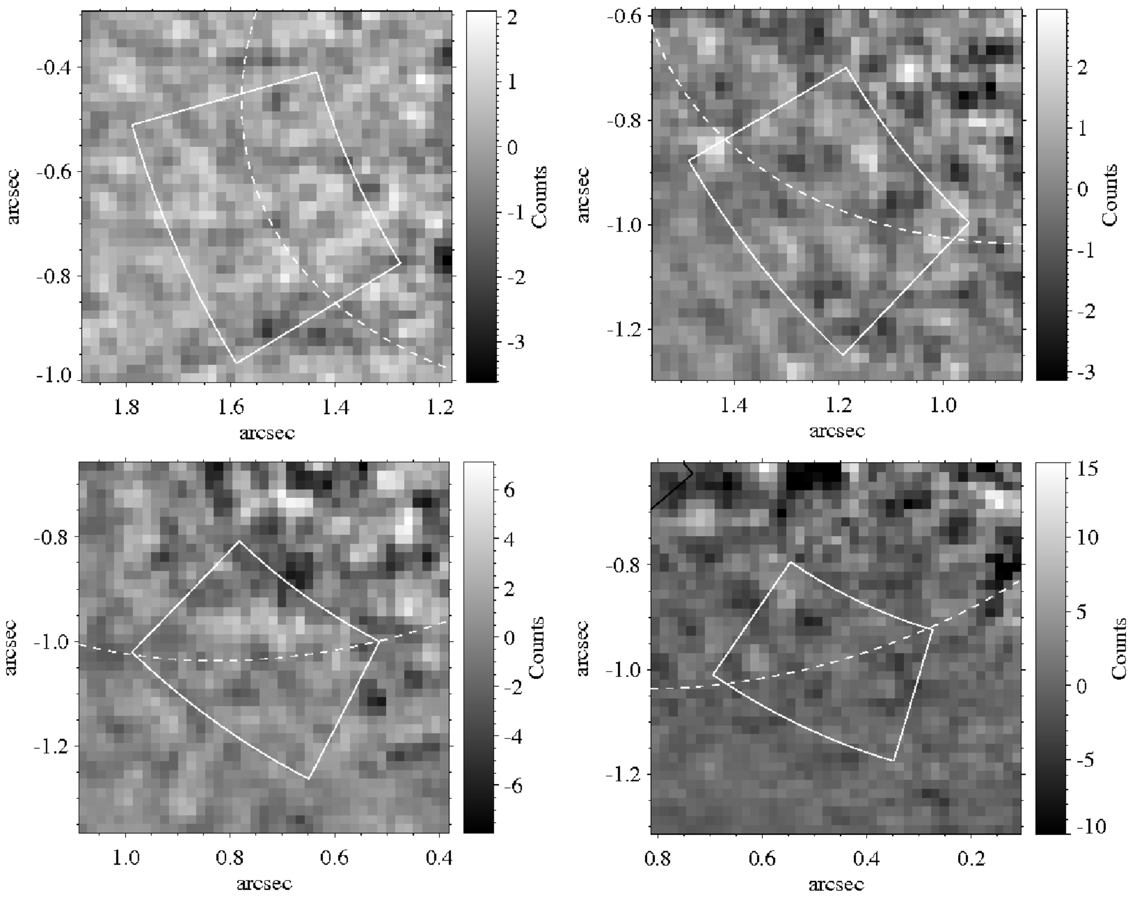

Fig. 4.4: Zoomed-in counterparts of the F1-F3 images from each epoch in Fig. 4.3. The field of view is centered on the expected position of the companion.

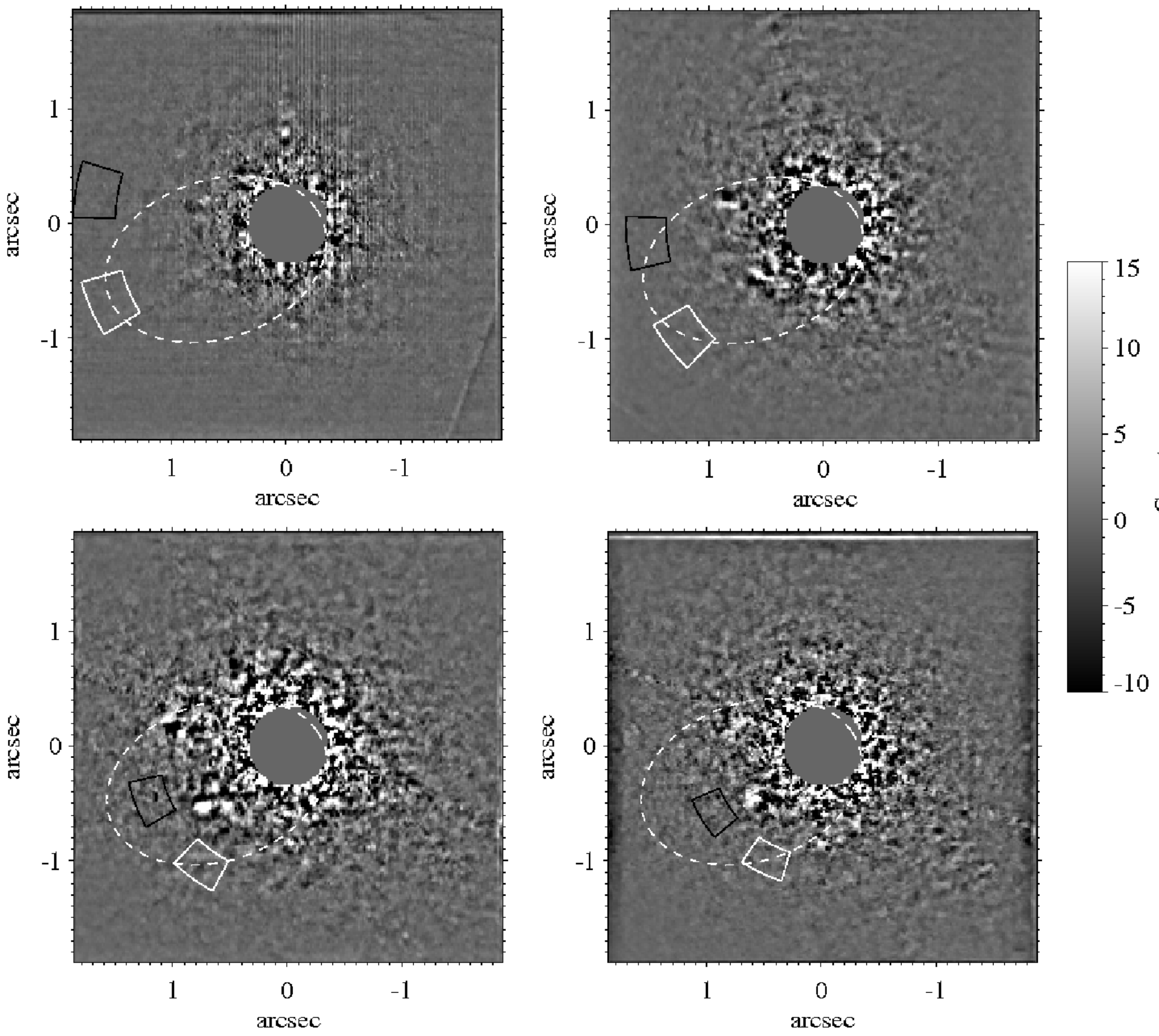

Fig. 4.5: The output F2-F3 images from each of the observations in sequence. Upper left: Epoch 1. Upper right: Epoch 2. Lower left: Epoch 3. Lower right: Epoch 4. The dotted line marks the best-fit orbit from astrometric and radial velocity data. The areas enclosed by white and black borders are error boxes for the expected positions of the bright and dark signatures of the companion, respectively. In all of the images, north is up, and east is to the left.

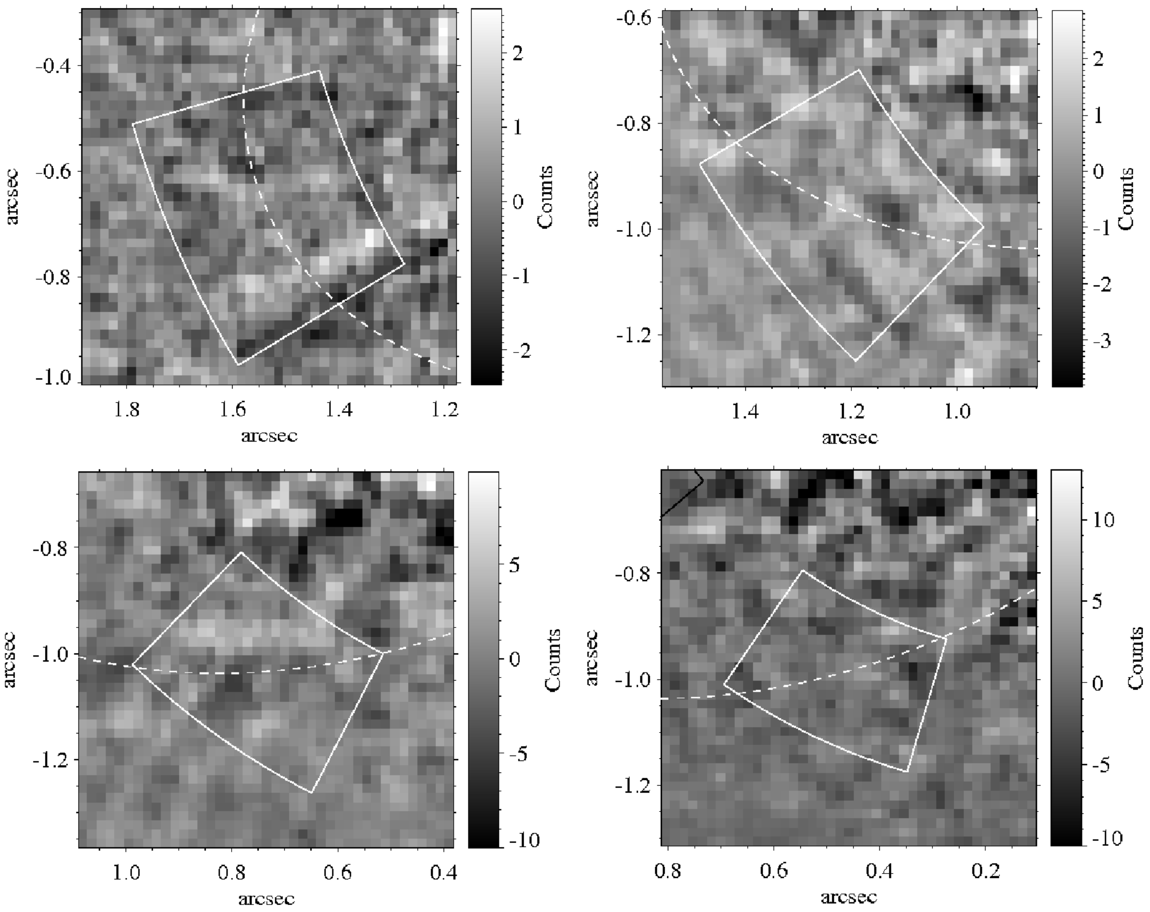

Fig. 4.6: Zoomed-in counterparts of the F2-F3 images from each epoch in Fig. 4.3. The field of view is centered on the expected position of the companion.

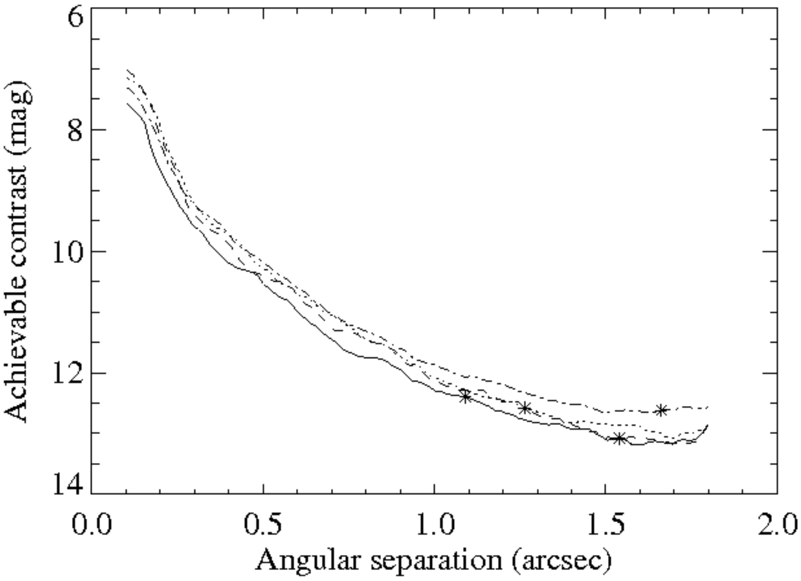

Fig. 4.7: 3σ detection limits for our images of ϵ Eri as a function of radial angular separation, based on local standard deviations. The limits are based on the narrow-band F1 brightness contrast (for H-band contrasts, see Figs 4.10 and 4.11). The dash-dotted line is the epoch 1 data, the dotted line is the epoch 2 data, the dashed line is the epoch 3 data, and the solid line is the epoch 4 data. The star on each curve represents the expected angular separation based on the dynamical measurements. It can be seen that even though the epoch 4 data has the highest overall sensitivity, the smaller expected separation of ϵ Eri b leads to a worse detection limit than for the other epochs. The range within 0.1 arcsec, where saturation occurs in some frames, has been set to zero.

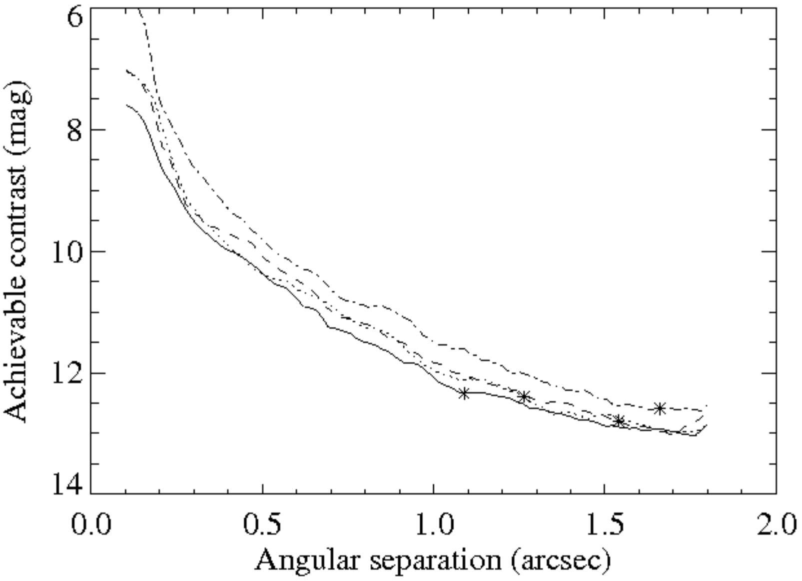

Fig. 4.8: Same as Fig. 4.7, but for F2-F3 instead of F1-F3. The sensitivity is somewhat worse (by a few tenths of a magnitude) in this case, probably due to a worse quality of the F2 sub-frame.

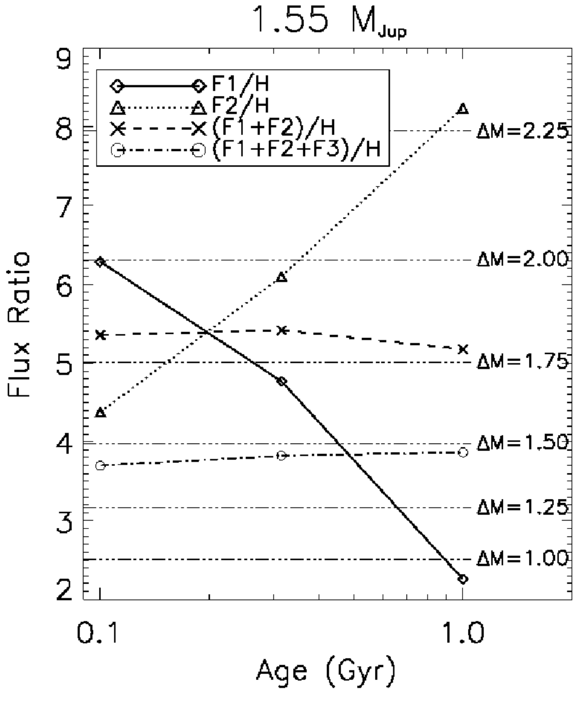

Fig. 4.9: Calculated narrow-band to H-band offsets for ϵ Eri b, based on the Burrows et al. (2003) model. Also plotted are the offsets that can be expected if the narrow-band images are averaged instead of differenced.

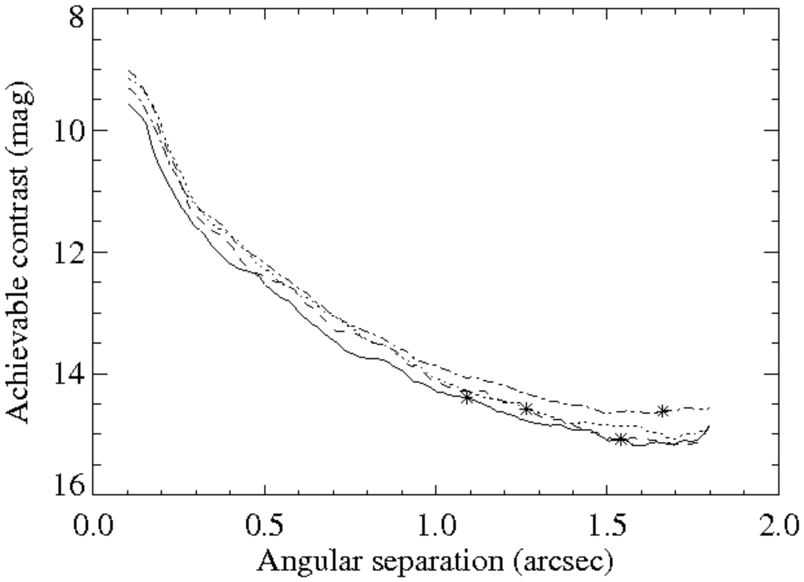

Fig. 4.10: H-band brightness contrasts for a 3σ detection, based on the calculated offsets and the F1 detection limits (see Fig. 4.7), assuming an age of 100 Myr. The stars mark the expected position, based on the current best-fit astrometry, of the companion at each epoch.

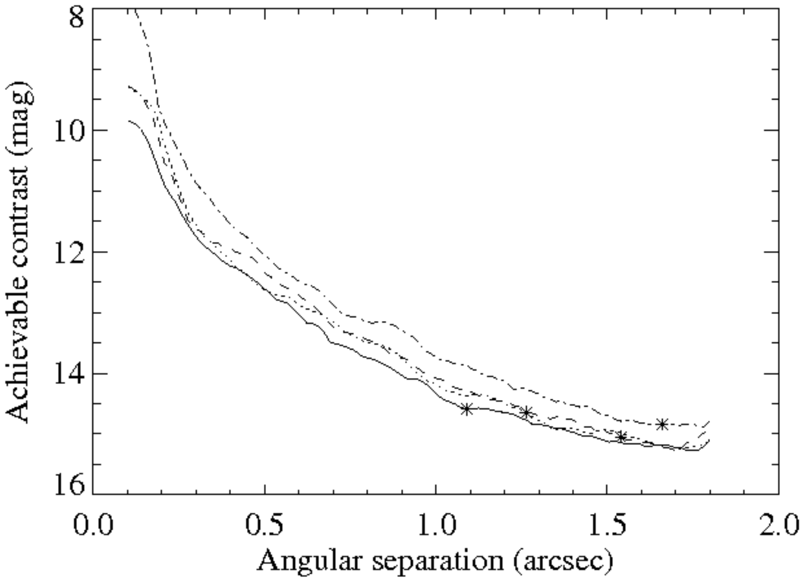

Fig. 4.11: H-band brightness contrasts for a 3σ detection, based on the calculated offsets and the F2 detection limits (see Fig. 4.7), assuming an age of 1 Gyr. The stars mark the expected position, based on the current best-fit astrometry, of the companion at each epoch.

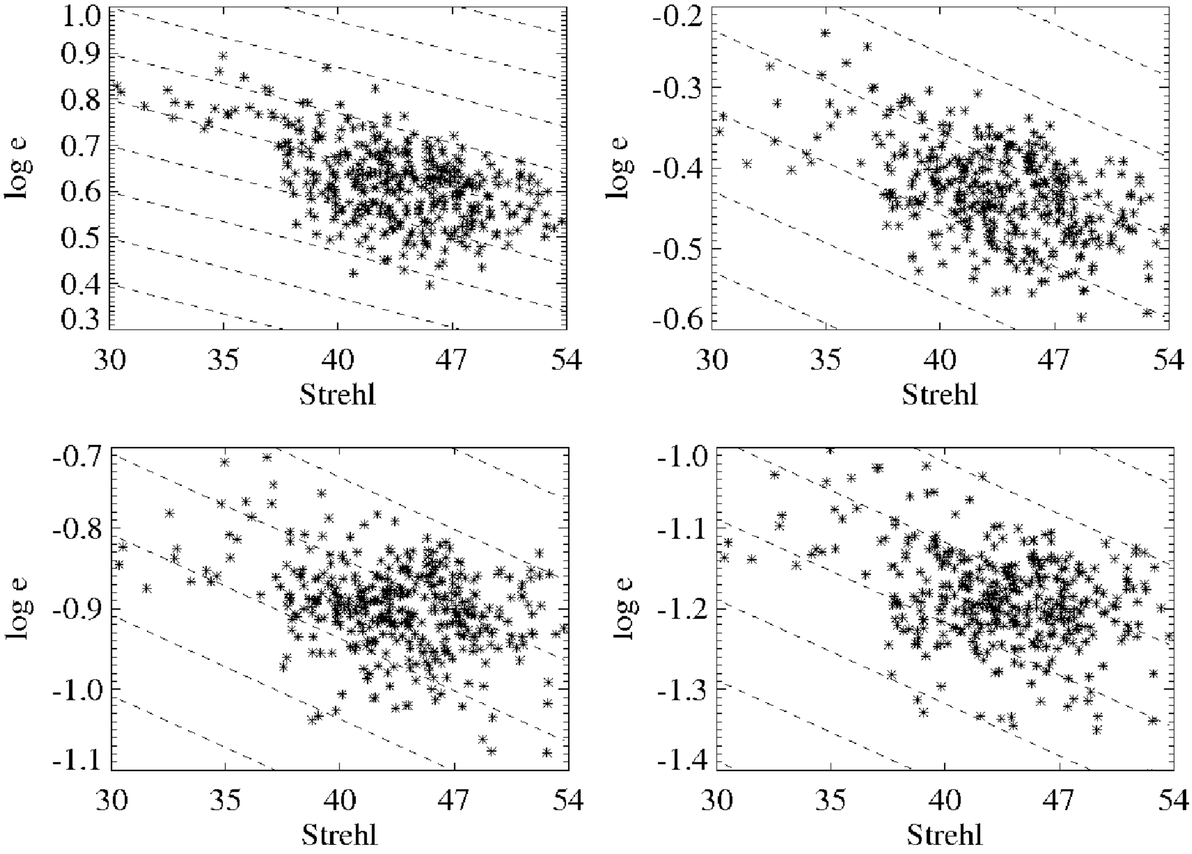

Fig. 4.12: The logarithmic Strehl-normalized error e as a function of Strehl ratio for the epoch 2 data (stars). Upper left: Zone 1 (0-19 pixels away from the center). Upper right: Zone 2 (20-39 pixels). Lower left: Zone 3 (40-59 pixels). Lower right: Zone 4 (60-79 pixels). The dashed lines indicate a reference slope corresponding to $e \sim S^{-1}$. Since the range of Strehl ratios is small for this epoch, and the dispersion is rather large, the trend is not very easily seen in this case. However, note that the result is entirely consistent with epoch 3 (see Fig. 4.13). All the four zones appear to give very similar results. Note that since the dashed lines are equally spaced regardless of epoch and zone, it is easy to compare the dispersions. Note also that the x-axis is in logarithm scale.

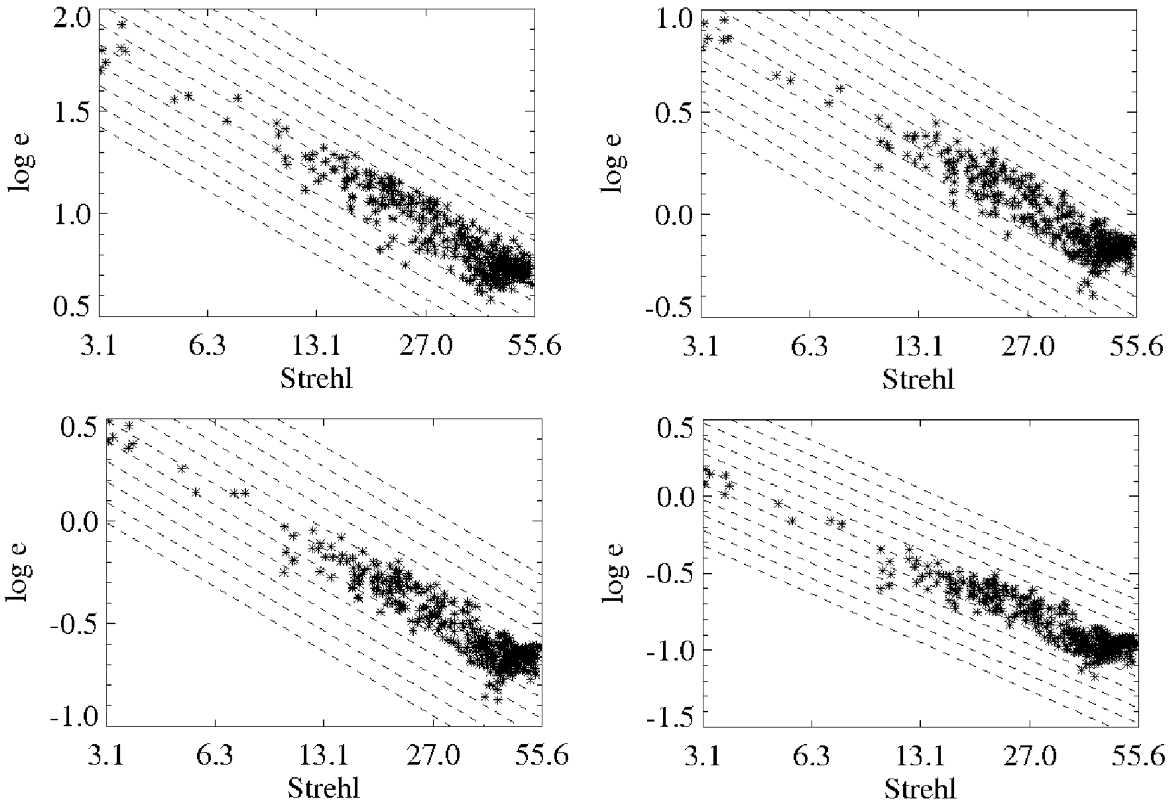

Fig. 4.13: The logarithmic Strehl-normalized error e as a function of Strehl ratio for the epoch 3 data (stars). Upper left: Zone 1 (0-19 pixels away from the center). Upper right: Zone 2 (20-39 pixels). Lower left: Zone 3 (40-59 pixels). Lower right: Zone 4 (60-79 pixels). The dashed lines indicate a reference slope corresponding to $e \sim S^{-1}$. Despite the fact that the dispersion is equally large here as for the other epochs, the trend is particularly obvious for this case, since the Strehl ratios cover such a relatively wide range. All the four zones appear to give very similar results. Note that the x-axis is in logarithm scale.

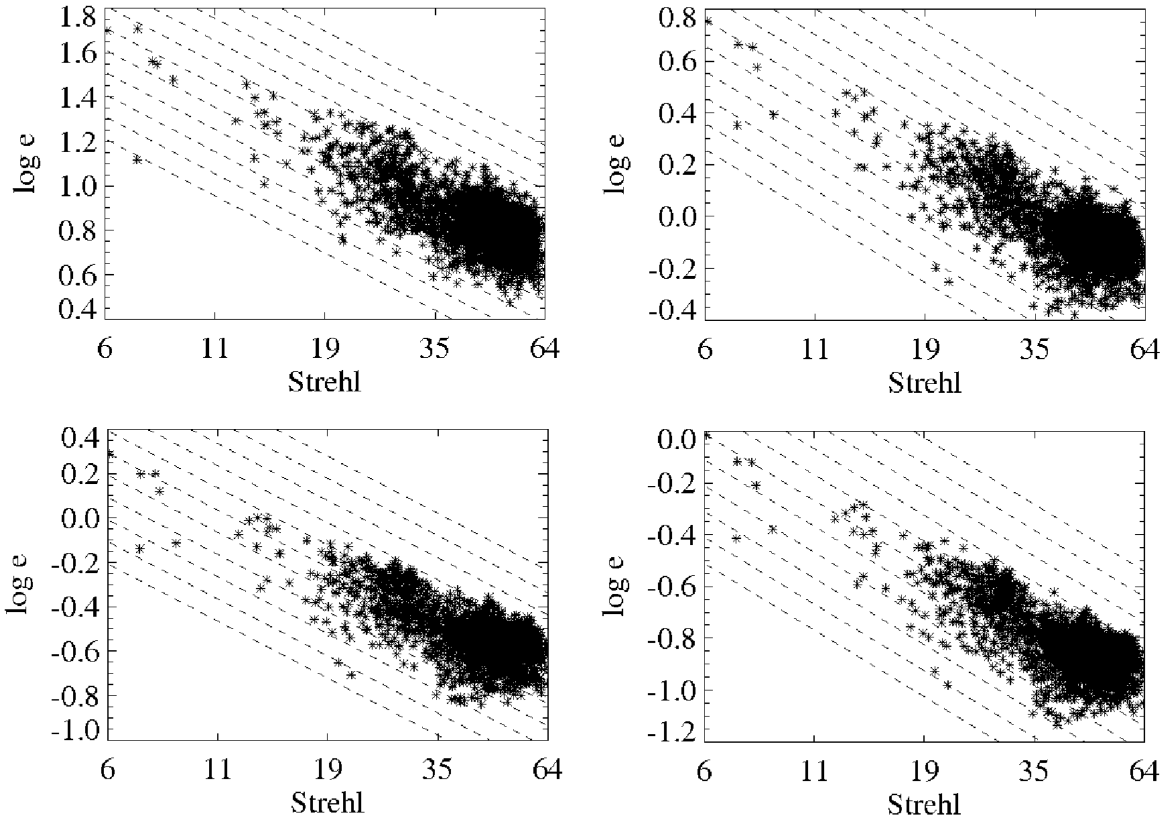

Fig. 4.14: The logarithmic Strehl-normalized error e as a function of Strehl ratio for the epoch 4 data (stars). Upper left: Zone 1 (0-19 pixels away from the center). Upper right: Zone 2 (20-39 pixels). Lower left: Zone 3 (40-59 pixels). Lower right: Zone 4 (60-79 pixels). The dashed lines indicate a reference slope corresponding to $e \sim S^{-1}$. Thanks to the very large number of data points for this epoch, it is quite clear that the data follows the expected $e \sim S^{-1}$ trend. All the four zones appear to give very similar results. Note that the x-axis is in logarithm scale.

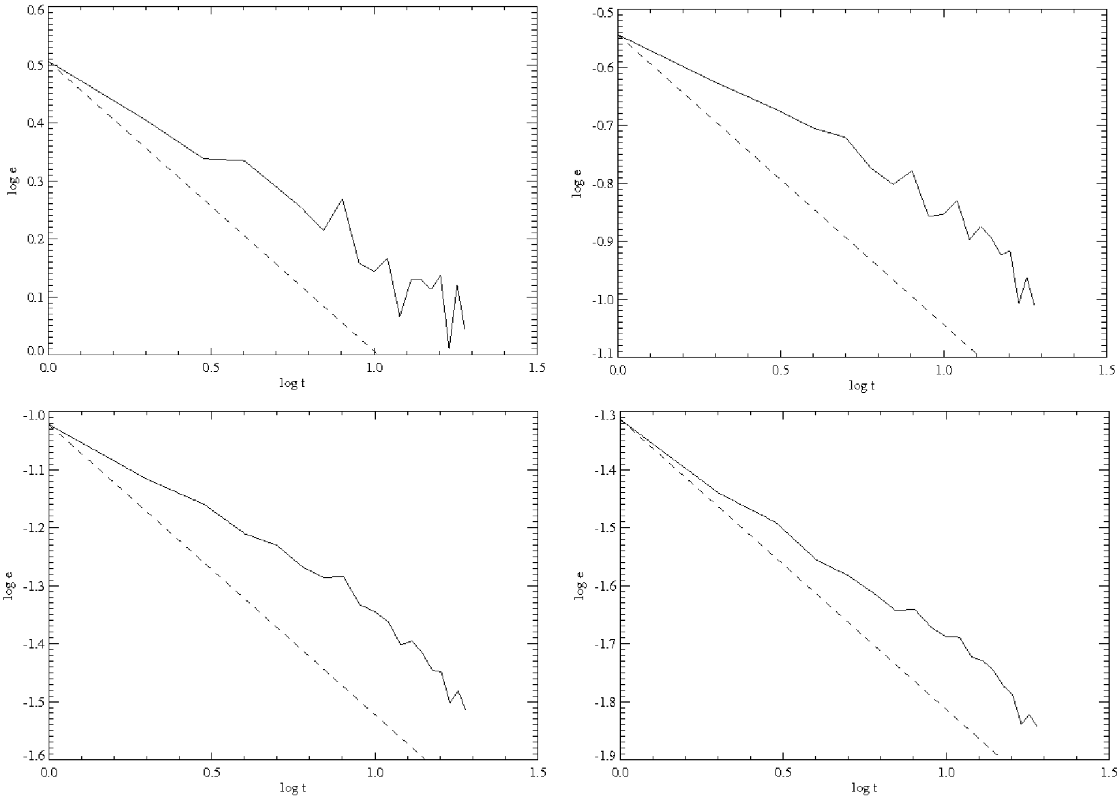

Fig. 4.15: The logarithmic Strehl-normalized error e as a function of time for the epoch 2 data (solid line). Upper left: Zone 1 (0-19 pixels away from the center). Upper right: Zone 2 (20-39 pixels). Lower left: Zone 3 (40-59 pixels). Lower right: Zone 4 (60-79 pixels). The dashed line indicates a reference slope corresponding to $e \sim t^{-1/2}$. The errors fall off slower than, but fairly close to, the $e \sim t^{-1/2}$ slope that would be expected for, e.g., photon noise dominated data. Oddly, the errors seem to drop off faster for longer integration times than for shorter times for this particular epoch, whereas the opposite would generally be expected. As would be expected, the dispersion is the largest in the innermost region, where part of the stellar PSF is saturated, and where noise variations are generally larger. Note that the x-axis is in logarithm scale.

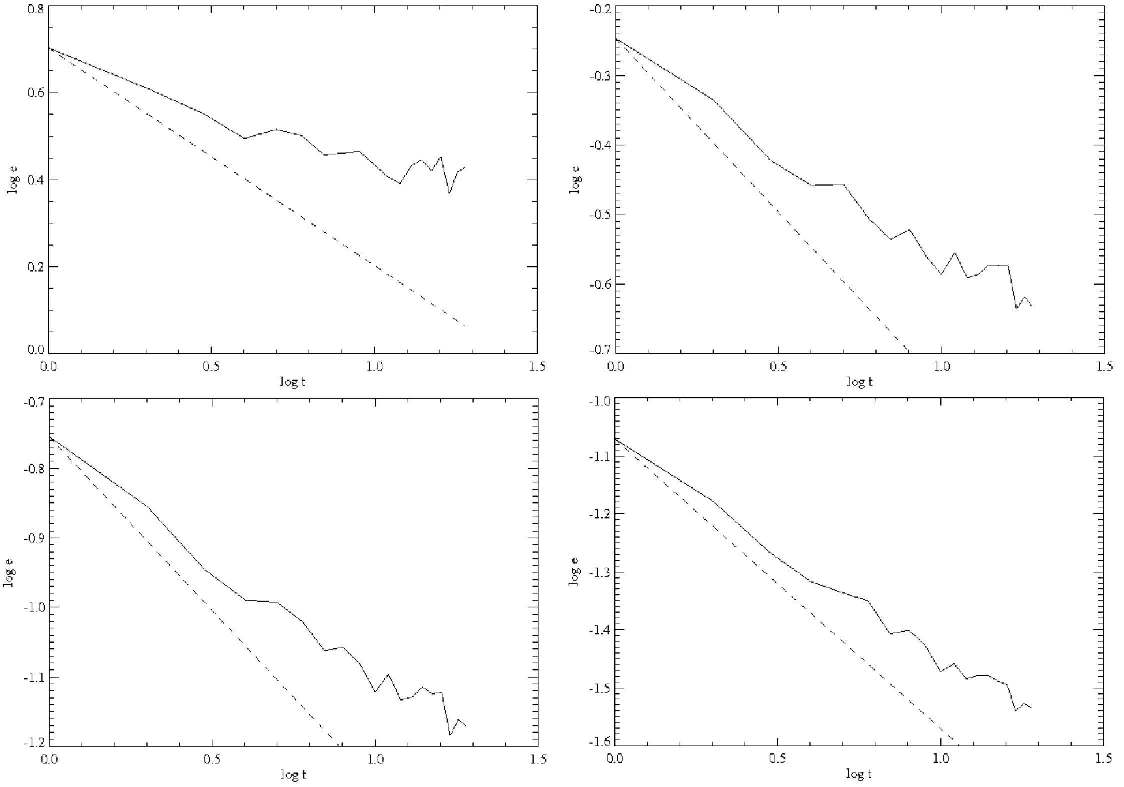

Fig. 4.16: The logarithmic Strehl-normalized error e as a function of time for the epoch 3 data (solid line). Upper left: Zone 1 (0-19 pixels away from the center). Upper right: Zone 2 (20-39 pixels). Lower left: Zone 3 (40-59 pixels). Lower right: Zone 4 (60-79 pixels). The dashed line indicates a reference slope corresponding to $e \sim t^{-1/2}$. The errors fall off slower than, but fairly close to, the $e \sim t^{-1/2}$ slope that would be expected for, e.g., photon noise dominated data. As would be expected (and in difference from epoch 2), the error falls off slower at longer integration times, as the residual noise is becoming increasingly dominated by static or quasi-static noise sources. The fall-off seems somewhat better in the outer regions than in the inner ones. Note that the x-axis is in logarithm scale.

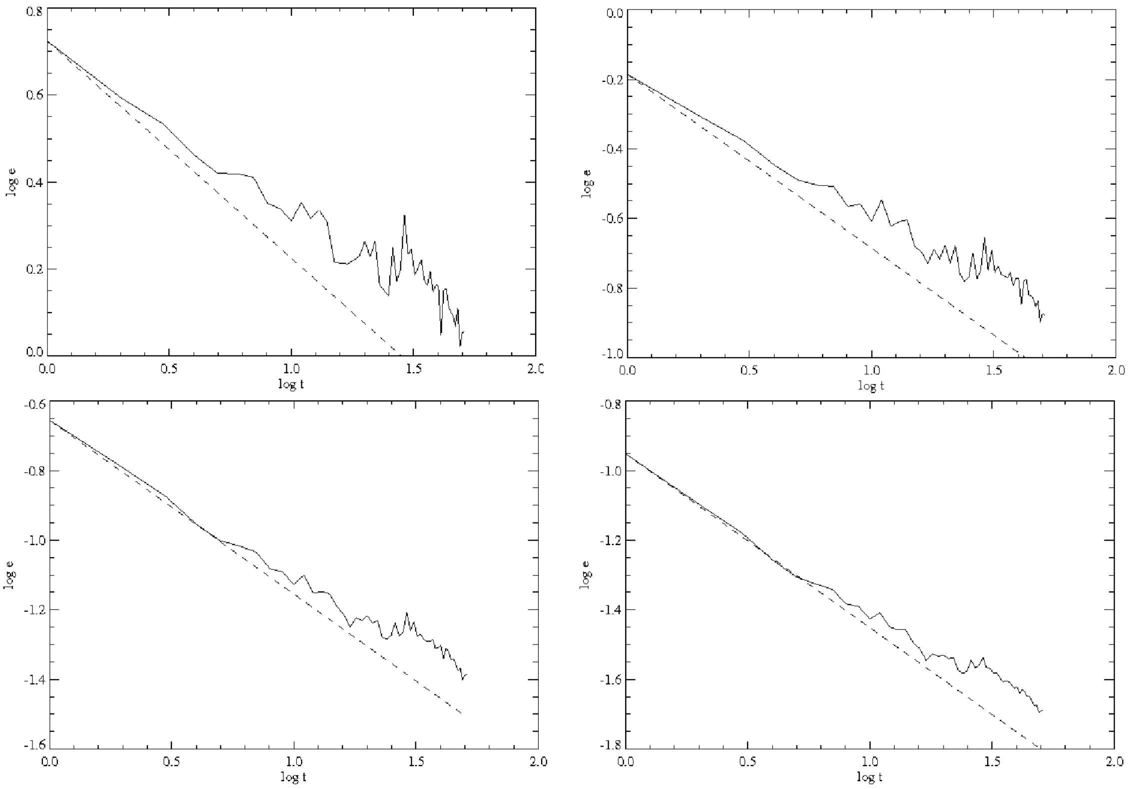

Fig. 4.17: The logarithmic Strehl-normalized error e as a function of time for the epoch 4 data (solid line). Upper left: Zone 1 (0-19 pixels away from the center). Upper right: Zone 2 (20-39 pixels). Lower left: Zone 3 (40-59 pixels). Lower right: Zone 4 (60-79 pixels). The dashed line indicates a reference slope corresponding to $e \sim t^{-1/2}$. The errors fall off slower than, but fairly close to, the $e \sim t^{-1/2}$ slope that would be expected for, e.g., photon noise dominated data. Due to the large amount of data points for this epoch, this is the most reliable data set of the three. The fall-off of the errors are slower for larger integration times, as was seen also for epoch 3. The dispersion also clearly decreases outwards from the center. Also, the fall-off seems to be the fastest in the outermost regions. It is remarkable that after 1.5 hours of effective integration time per angle, the error still drops very close to the $e \sim t^{-1/2}$ slope. Note that the x-axis is in logarithm scale.

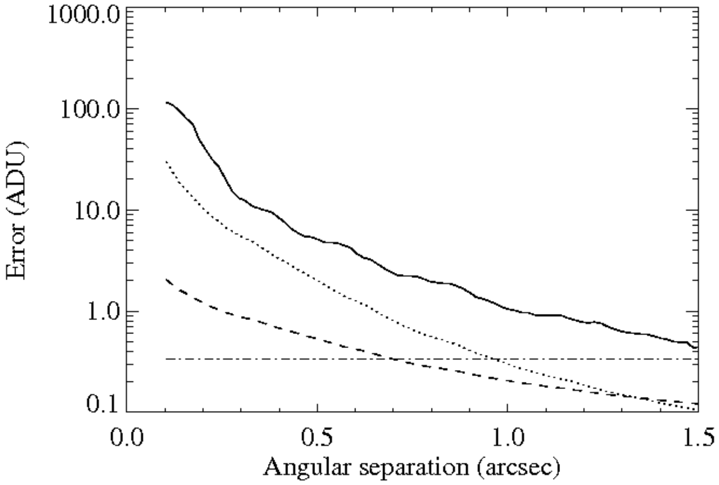

Fig. 4.18: The real error (solid line), compared to estimates of the photon noise (dashed line), read noise (dash-dotted line) and the flat field noise (dotted line) for epoch 2. The real noise is dominated by the residual speckle noise, except in the very outermost part where the read noise seems to be significant. The innermost region (within about 0.1 arcsec) is saturated, and does not provide any meaningful information about the real error.

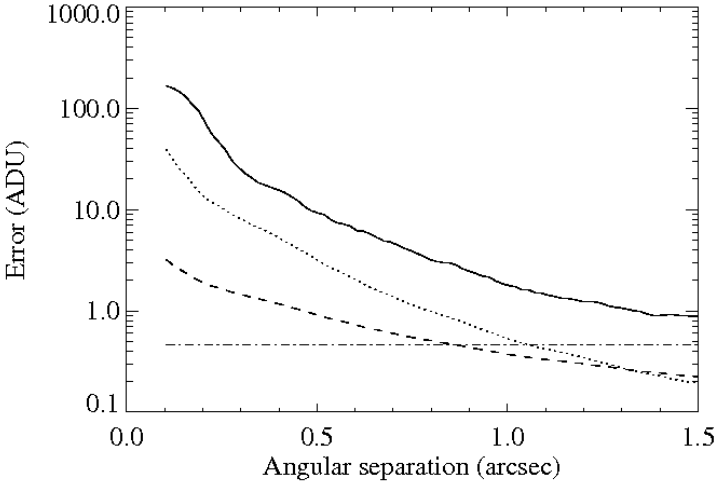

Fig. 4.19: The real error (solid line), compared to estimates of the photon noise (dashed line), read noise (dash-dotted line) and the flat field noise (dotted line) for epoch 3. The real noise is dominated by the residual speckle noise. The innermost region (within about 0.1 arcsec) is saturated, and does not provide any meaningful information about the real error.

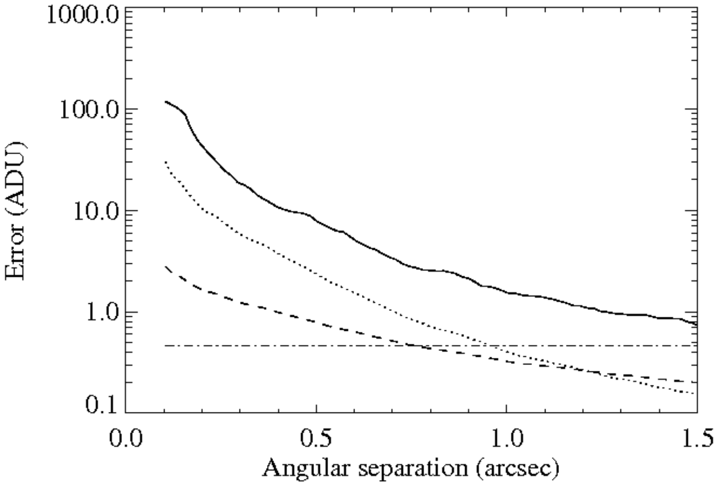

Fig. 4.20: The real error (solid line), compared to estimates of the photon noise (dashed line), read noise (dash-dotted line) and the flat field noise (dotted line) for epoch 4. The real noise is dominated by the residual speckle noise. The innermost region (within about 0.1 arcsec) is saturated, and does not provide any meaningful information about the real error.

Tab. 4.3: Observing log of NACO high-contrast imaging observations of ϵ Eri.

Epoch	Main date	MJD	Frames per angle	DIT(s)	NDIT	Tot. time per angle	Mean Strehl (1.6 μm)	Mean seeing
1	17 Aug. 2003	52868	10	0.5	60	300	11.5%	1.26
2	19 Sep. 2004	53267	20	0.6	160	1920	32.2%	0.91
3	10 Aug. 2005	53592	16	1.0	86	1376	35.7%	0.87
4	1 Jan. 2006	53736	52	1.0	86	4472	33.8%	0.82

Chapter 5

A test case for spectral differential imaging with SINFONI

From Janson et al. (2008): A&A 478, 597

5.1 Abstract

Spectral differential imaging is an increasingly used technique for ground-based direct imaging searches for brown dwarf and planetary mass companions to stars. The technique takes advantage of absorption features that exist in these cool objects, but not in stars, and is normally implemented through simultaneous narrow-band imagers in 2 to 4 adjacent channels. However, by instead using an integral field unit, different spectral features could be used depending on the actual spectrum, potentially leading to greater flexibility and stronger detection limits. In this paper, we present the results of a test of spectral differential imaging using the SINFONI integral field unit at the VLT to study the nearby active star L449-1. No convincing companion candidates are found. We find that the method provides a 3σ contrast limit of 7.5 mag at 0.35", which is about 1.5 mag lower than for NACO-SDI at the same telescope, using the same integration time. We discuss the reasons for this, and the implications. In addition, we use the SINFONI data to constrain the spectral type in the NIR for L 449-1, and find a result between M3.0 and M4.0, in close agreement with a previous classification in the visual range.

5.2 Introduction

In recent years, developments in techniques and instrumentation have led to a strongly increased capacity for high-contrast imaging of substellar companions at small angular separations to stars, from the ground. In particular, the use of high-order adaptive optics (AO) in combination with various differential imaging techniques provides a sensitivity for companions that are 10^4-10^5 times fainter than the primary at a separation of 0.5"-1" at near-infrared wavelengths (see Janson et al. 2007b and Biller et al. 2007). According to theoretical models (see e.g. Baraffe et al. 2003), this corresponds to objects of a few times the mass of Jupiter around young stars.

As shown in previous chapters, a particularly efficient technique for such observations is simultaneous spectral differential imaging (see e.g. Rosenthal et al. 1996 and Racine et al. 1999). To reiterate, for SDI the flux from a star is observed in two narrow, adjacent wavelength bands simultaneously. The bands are chosen such that one is inside and one outside of an absorption feature which arises uniquely in cool atmospheres. One example of such a feature is the methane band at 1.6 μm, which only occurs in dwarfs of spectral type T or later, whereas a stellar spectrum is flat in this range. By subtracting one image from the other, the stellar point spread function (PSF) can be largely subtracted out, since it is approximately flat around 1.6 μm. Along with the main PSF, most of the random PSF substructure (speckle noise) is subtracted out as well, since the images are simultaneous and hence the atmospheric speckle pattern is the same in both images.

As discussed in Chap. 4, NACO-SDI at the VLT is an excellent instrument for the purpose of SDI observation (see Lenzen et al. 2004). NACO-SDI images the same field in three different narrow bands around the 1.6 μm methane feature simultaneously. It is designed to minimize non-common path aberrations, and has been shown to be capable of achieving a contrast of more than 13 mag between star and companion at 1" angular separation at the 3σ level (see Janson et al. 2007b), without the use of a coronagraph. One limitation of the NACO-SDI instrument is that it can only attain information about the methane feature in question. It has been suggested (Berton et al. 2006b) that if $N > 1$ different absorption features are used at once for SDI purposes, the achievable contrast would increase by a factor $N^{1/2}$ for the same integration time, simply due to the more efficient use of photons. Hence, in principle, an instrument with the capacity to do multi-feature SDI (MSDI) would be preferable to NACO-SDI, if the instruments perform equally well in all other respects (in terms of differential aberrations, etc.).

SINFONI is an integral field spectroscopy instrument with AO capability at the VLT (see Eisenhauer et al. 2003 and Bonnet et al. 2004). It uses an image slicer to divide the FOV into pseudo-slits that are individually dispersed on a grating, hence retaining both the spatial and spectral information of the incoming light. The output data can be used to construct a data cube that stores spatial information along two axes, and spectral information along the third. In this way, SINFONI can be used as an SDI or MSDI instrument, since the cube contains simultaneous narrow-band images over a large range of wavelengths.

We have acquired SINFONI data to test its capacity for SDI. In the following sections, we describe the observations and data reduction, and compare the results with NACO-SDI. We also compare the results to a spectral deconvolution (SD) scheme applied to another set of SINFONI data by Thatte et al. (2007). We dicuss the advantages and disadvantages of using SINFONI for high-contrast imaging and characterization of exoplanet and brown dwarf companions to stars. Finally, we analyze the non-differential collapsed images, and constrain the spectral type of L 449-1 from H- and K-band spectroscopy.

5.3 Observations

The target chosen for the observation was L 449-1. This star was identified as a high proper motion star in Scholz et al. (2005), who also used spectroscopy and photometry to classify the object as an M4 star only 5.7 pc away. In addition, the star shows signs of activity, through both Hα emission and identification with a bright X-ray source, possibly indicating a young age. Hence, it is of particular interest for high-contrast imaging surveys, but since it was not properly classified prior to the publication of Scholz et al. (2005), it has not been targeted by such surveys. For this reason, L 449-1 makes an excellent test case for high-contrast imaging with SINFONI.

The data of L 449-1 were taken using SINFONI at the VLT during a visitor mode run at Paranal on the night of 26 Jan 2007. In order to get the best possible spatial sampling, the smallest available SINFONI field of view of 0.8” × 0.8” was used, yielding an effective pixel scale of 12.5 mas/pixel by 25 mas/pixel. The “H+K” setting was used, covering the spectral range of 1.4 μm to 2.5 μm at a spectral resolution of about $R = 1500$. Adaptive optics was used with the target itself as the guide star, and provided good and stable wavefront correction – the average Strehl ratio was 34 % (corresponding to a wavelength of 1.95 μm) as given by the AO system itself. The weather conditions were also good and stable, with an average seeing of 0.72” at 500 nm as given by the atmospheric seeing monitor at Paranal.

For the purpose of efficient subtraction of the stellar PSF, the data were taken at two different instrument rotations. This enables use of a data reduction scheme known as roll subtraction (see Mueller & Weigelt 1987) or angular differential imaging (ADI, see e.g. Marois et al. 2006). Our implementation of this technique is described in Kellner (2005) and Janson et al. (2007b). Five target frames and one sky frame were taken at an angle of 0°, and three target frames plus one sky frame at an angle of 90°. The effective integration time per frame was 350 seconds.

5.4 Data reduction

All the frames generated during observations were translated into equivalent data cubes, with spatial information along two of the axes, and spectral information along the third, using the standard ESO data reduction pipeline with the Gasgano GUI tool. This procedure also performed all basic data reduction steps, such as sky subtraction, flat fielding, bad pixel correction and wavelength calibration. The output data cubes were used in a number of further data reduction procedures to generate useful data products, using IDL routines that were written specifically for these purposes. The results of the basic reduction also included extracted spectra of L449-1 and the telluric standard star, that were also further processed by our IDL routines for spectral type analysis. We note that this procedure, which is detailed below, was designed to correspond as closely as possible to the equivalent procedure for NACO-SDI (see Kellner 2005 and Janson et al. 2007b) so that no difference in the final performance can be simply attributed to a difference in the implementation of the technique.

For the SDI, which was our primary purpose, different combinations of image slices were co-added to represent images of different filters. In particular, images denoted by f_1, f_2 and f_3 were created, where f_1 is an image in the wavelength range 1.5625 μm to 1.5875 μm, f_2 in 1.5875 μm to 1.6125 μm, and f_3 in 1.6125 μm to 1.6375 μm. This construct was designed in order to create, as close as possible, equivalence to the F_1, F_2 and F_3 filters of NACO-SDI (see Janson et al. 2007b). The PSF center was determined for every image slice in every data cube through gaussian centroiding, and the images were shifted to a common position based on this information. Remaining differences in photocenter positions were minimized via cross-correlation. Sub-pixel shifts were accommodated through bilinear interpolation. The data were also subsampled by a factor 2 to get the same effective sampling in the x- and y-direction, and to avoid image artefacts arising from the double representation of each sample point in the y-direction (each image slice is 64 by 64 pixels in a SINFONI data cube, but since the actual sampling is 12.5 mas/pixel in the x-direction and 25.0 mas/pixel in the y-direction, each sample point is represented twice in the y-direction). f_1, f_2 and f_3 were subsequently rescaled to a common λ/D scale and subtracted from each other to produce SDI images. Unsharp-masking was applied in order to remove the low spatial frequencies (background and halo), whilst retaining higher-frequency features (such as possible companions, but also speckles). This was done by convolving each image with a gaussian kernel with a FWHM of 140 mas, and subsequently subtracting the smooth image from the original image.

Finally, the resulting difference images at each rotation angle were co-added, after which, any co-added image corresponding to one angle was subtracted from the other. The radial profile of the error was calculated for the final image. This was done for each separation by selecting all pixels between an inner and outer radius of ± 1 pixel from the separation of interest, and taking the standard deviation of those pixels. By comparing this radial profile to the brightness of the primary star itself, the achieved contrast as a function of angular separation could be determined.

For test purposes, the same procedure as described above was also performed for three images in the K-band: g_1 at 2.095 μm to 2.120 μm, g_2 at 2.120 μm to 2.145 μm and g_3 at 2.145 μm to 2.170 μm (i.e., with the same type of configuration and the same bandwidth as f_1, f_2 and f_3). These wavelengths are arbitrary from a physical viewpoint, and are not expected to correspond to any particularly interesting spectral features. Instead, the purpose of the analysis, in this case, was to test whether the contrast performance is significantly different in the H- and K-bands. One particular reason for this was to test whether the output quality is strongly dependent on the spatial sampling (which is sub-critical in the y-direction in the H-band, but critical in the K-band).

For general (non-differential) analysis of the primary itself, as well as for detecting possible relatively low-contrast companions and measuring their spectra, it is most practical to keep all the image slices in the cube at their original λ/D scale, and simply do the spatial and spectral analysis based on the original cube. For this purpose, we generated wavelength-collapsed frames in the H- and K-bands in order to produce broadband-equivalent images for spatial analysis. Furthermore, in both H- and K-bands a spectrum integrated over the whole field of view (except for a margin of four pixels at the edges of the field) was calculated. If L 449-1 is single or significantly brighter than any of its companions, the extracted spectrum corresponds to the spectrum of L 449-1 itself. In addition, a new cube was generated by subtracting the extracted spectrum from each spatial position in the original cube, after normalizing the spectrum by the intensity of the broad-band frame at each corresponding position. The result is essentially a differential spectroscopy cube, mapping the spatial distribution of spectral deviance from the mean spectrum.

5.5 Results and discussion

5.5.1 Spectral differential imaging

The $f_1 - f_3$ image, which corresponds to the standard final output from NACO-SDI, is shown in Fig. 5.1. No interesting companion candidates can be seen in the image. The corresponding 3σ contrast map is shown in Fig. 5.2; the 3σ radial contrast curve is shown compared to NACO-SDI in Fig. 5.3, and compared to other implementations of the same data set in Fig. 5.4. It is quite clear that for the same integration time, and virtually the same filter set, and under similar weather conditions, a SINFONI-based SDI approach performs significantly worse than a NACO SDI-based one. While the Strehl ratio is better for NACO-SDI, the seeing is worse, reflecting a difference in AO performance. However, we note that the difference in Strehl ratio is only a factor 1.4, which, if we assume a linear dependence between SNR and Strehl ratio for the NACO-SDI data (see Janson et al., 2007b) corresponds to 0.4 mag in brightness contrast. The difference in Fig. 5.3 is much larger than that, hence it is not plausible that it is solely due to AO performance. Furthermore, Fig. 5.4 shows that the performance over most of the parameter range is very similar in the H- and K-bands, despite the Strehl ratio being higher in the K-band than in the H-band (and in fact, becomes higher than the Strehl ratio for the NACO-SDI data). This again demonstrates that AO performance is not the limiting factor for the achieved contrast of SINFONI SDI. Aside from the average noise impact, the spatial distribution of the noise is also different, as SINFONI SDI has a spatially constant noise floor that dominates most of the image space.

In Chap. 4, it was shown that the SNR increased with integration time t as almost SNR $\sim t^{1/2}$ for NACO-SDI, even for the deepest integrations for most of the spatial range. It is highly interesting to make a similar test for SINFONI SDI, to assess its appropriateness for high-contrast imaging. Such a task is somewhat more challenging for the SINFONI data, since the overheads and bright object constraints of SINFONI forced us to use a poor temporal resolution during the observations, with 5 individual data cubes at 0° rotation angle and 3 at 90°. To get a robust picture of how the SNR develops, we calculated every possible combination of frames for one, two and three frames per angle, and averaged the contrast curves for each case. The result is shown in Fig. 5.5. It is clear that the SNR develops considerably slower than what would be expected if the noise was dominated by temporally uncorrelated sources. This shows that increasing the integration time would not improve the results to the same degree as is the case for NACO-SDI.

The relatively poor performance and quasi-static nature of the residual noise, as well as its spatial distribution, implies that errors dominate in the SINFONI data that are not present or are well controlled for NACO-SDI. For SINFONI, the image is divided into horizontal stripes by the image slicer, after which, each slice is dispersed on a grating and subsequently registered on the detector. Hence, each spatial slice travels a slightly different optical path, and additionally, can suffer from edge effects in the interaction with the image slicer. Also, each wavelength travels a different optical path after being dispersed on the grating. These differential effects lead to quasi-static errors that may dominate the noise. The horizontal stratification that can be traced in parts of the image certainly implies that the image slicer is at least partly responsible for the final result. Path differences for light of different wavelengths also occur in NACO-SDI for the different sub-images, but in that case, a primary objective was to minimize precisely such errors (see e.g. Brandner et al. 2004). Any possible problems with the cube generation, as peformed by the ESO pipeline, could also affect the results. The similar results achieved in the H- and K-bands (Fig. 5.4) implies that spatial sampling is not a critical issue for this case.

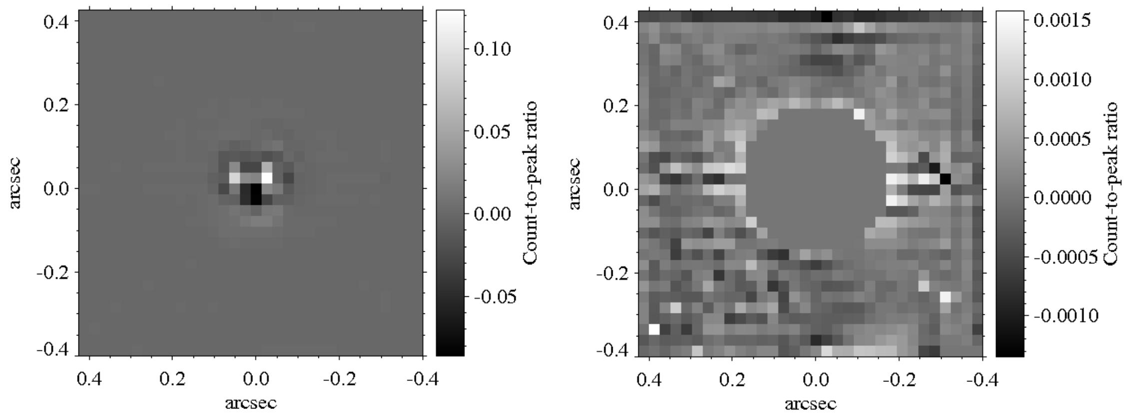

Fig. 5.1: SDI image given by $f_1 - f_3$. Left: Low-contrast version to show the central part of the image. Right: High-contrast version with an artificial mask placed over the center, to clearly illuminate the outer part. No convincing cool companion candidates can be found in the image. North is up and East is to the left.

Since the dominating error is (quasi-)static rather than dynamic, adding more spectral features will not increase the achievable contrast to the degree expected in a dynamical case. Aside from this, we note that no other feature apart from the CH_4 band in the H- or K-bands is quite as narrow, or has quite as high contrast between the continuum and the full depth of the feature. Therefore, we have to conclude that SDI with SINFONI cannot perform as well as NACO-SDI in terms of detecting previously unknown substellar companions. However, for follow-up observations of high-contrast objects detected by other means, where spectral properties need to be determined, the method has excellent prospects.

On this subject, we will briefly discuss the spectral deconvolution (SD) technique. SD was suggested for detection of substellar companions by Sparks & Ford (2002), and has been applied to AB Dor observations with SINFONI by Thatte et al. (2007). The latter show that the SNR of AB Dor C (a low-mass companion close to AB Dor A) can be increased by applying SD and using a priori information about the position of AB Dor C. They also

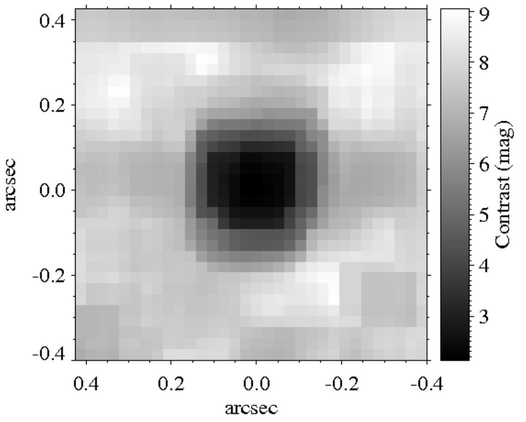

Fig. 5.2: SDI 3σ contrast map corresponding to Fig. 5.1. Each pixel corresponds to three times the standard deviation of a 5 by 5 pixel square centered on the equivalent position in the SDI image. North is up and East is to the left.

give a general radial contrast profile based on the standard deviation of the final image. Translating their quoted 1σ points into 3σ and including them in Fig. 5.1 implies that SD with SINFONI can reach almost as high contrast as NACO-SDI, if we generously assume that its SNR develops according to $t^{1/2}$. However, this contrast is only valid well outside of an angular separation quantified by Thatte et al. (2007) as the bifurcation radius. For the SINFONI "H+K" mode, the bifurcation radius is about 250 mas. Inside of this radius, a large fraction of the companion flux will inevitably be subtracted out by the SD technique (if its position is not known a priori or, equivalently, can be seen in the data already prior to applying the technique). Even outside of this radius, it is unclear whether the contrast is entirely applicable to blind searches, since a certain fraction of their flux would still be lost in the particular version of the SD technique upon which that result is based.

Of importance for high-contrast imaging purposes is not only the instrumental contrast that can be achieved, but also the spectral energy distribution of the possible companion. Here, the SDI technique has a strong advantage over the SD technique for cool companions such as low-mass brown dwarfs and exoplanets. Such objects exhibit strongly increasing absorption in the H- and K-bands with decreasing temperature. According to, e.g., the spectral models of Burrows et al. (2003), for young planets, the flux is strongly concentrated directly shortwards of the methane feature at 1.6 μm in the H-band, and practically no flux is present in the K-band. This favors the SDI technique, since the off-methane filters are located precisely at the peak of the planetary flux. At the same time, it disfavors the SD technique, since it includes a large spectral range that practically contains only noise from the primary and no signal from the companion. To give a practical example of this, we use the Baraffe et al. (2003) and Burrows et al. (2003) theoretical models to model the actual physical contrast that the SDI and SD methods will face, respectively, in the case of a 2 $M_{\rm jup}$ companion to a 0.3 $M_{\rm sun}$ star at an age of 100 Myr. The same method is used in, e.g., Janson et al. (2007b) and Apai et al. (2007). The physical contrast is subtracted from the instrumental (achieved contrast), and the results are shown in Fig. 5.6. It is clear that SD is considerably less well applicable than SDI for such cool objects, at least in its present form. Obviously, this difference is

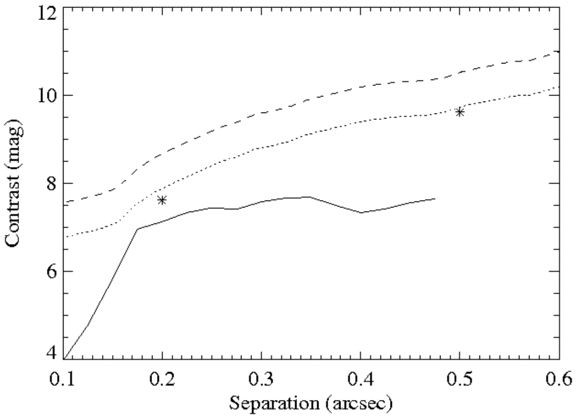

Fig. 5.3: Contrast curve for the SINFONI SDI image (solid line) compared to a corresponding NACO-SDI curve for ϵ Eri (dashed line), and the same curve normalized to the same integration time, assuming a $t^{1/2}$ SNR development (dotted line). Also plotted are two values quoted by Thatte et al. 2007 for spectral deconvolution with SINFONI, renormalized to the same integration time. See the text for discussions. See also Fig. 5.6 for a physical example.

less problematic for hotter objects. Still, high-contrast searches in general primarily aim to detect cool objects, and the SDI method is clearly preferable for such an objective. Since NACO-SDI performs better than SINFONI in this regard, this speaks in favor of the former for blind companion searches. In any case, for the SD technique to reach its full potential, it is necessary to know the position of the companion a priori. This underlines the fact that SINFONI is better suited for follow-up observations than for blind searches – a purpose for which other instruments (e.g., NACO-SDI) are more appropriate.

As a further comment concerning the comparison between SINFONI MSDI and NACO-SDI for high-contrast imaging, we note that several practical issues speak against SINFONI in this regard. The bright object constraints are tighter for SINFONI than for NACO, and SINFONI does not provide an option to use neutral density filters; therefore, some of the most interesting objects for high-contrast imaging (such as ϵ Eri), which are observable with NACO, are not observable with SINFONI. The FOV is much smaller for SINFONI than for NACO-SDI at the same pixel scale (and even then, the pixel scale for SINFONI is 2 times coarser in one direction). Finally, since the data is more memory-demanding and complex than NACO-SDI data, it is also more cumbersome to reduce and work with.

The issues adressed here are of relevance for future generations of planet-finding instruments, since they indicate that in order to achieve high-quality results for SDI with an integral field unit, they have to be carefully designed for providing high AO performance, temporal stability, optical quality and minimized non-common path aberrations. Future high-contrast instruments, such as SPHERE and GPI, include units for integral field spectroscopy that are specifically designed for planet-finding purposes (as opposed to SINFONI, which is a general-purpose instrument), and should improve the capacity for SDI significantly. Meanwhile, it is generally easier to accommodate these requirements with a differential imager, hence plausibly, a better performance in this regard can be expected for a differential imager given

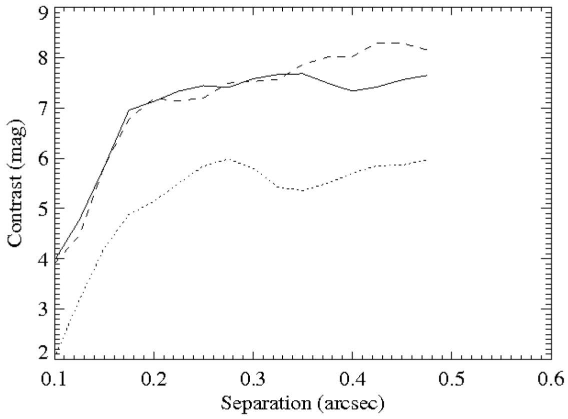

Fig. 5.4: 3σ Contrast curve for SINFONI SDI for $f_1 - f_3$ (solid line), and for $g_1 - g_3$ (dashed line). The latter is chosen only to show the instrumental performance in the K-band, and is not expected to correspond to any physically useful feature for SDI. The performance is very similar except at the outer edge. Also plotted is the contrast curve for the non-SDI f_1 image (dotted line), illustrating that a substantial improvement is gained from the differential imaging methods that we apply.

the same cost and effort constraints. Hence, units such as these have an important role also for future instruments, possibly being advantageous for blind searches. In any case, given the capacity for attaining quantitative spectral information with integral field units, they are clearly preferable for follow-up searches, and are hence undeniably relevant for future instruments.

5.5.2 Broad-band image

Two images collapsed over all wavelengths of the cubes of L 449-1 are shown in Fig. 5.7, one at 0° rotation and one at 90°. There is no convincing evidence for any low-contrast companion in those images. The PSF does look somewhat extended, and the extension rotates along with the camera, which is often indicative of a close binary. In this case, if such a secondary was real, it would be on the order of 10 % of the brightness of the primary. However, it is likely to be a PSF artefact. A real physical companion that is fainter than the primary would inevitably be cooler. Hence, in a differential spectroscopy cube, where an average spectrum is subtracted from the original cube as described in the previous section, a feature would be seen at the expected position of the companion that is significantly redder than the rest of the field. In other words, it would be darker than average at short wavelengths, and brighter than average at long wavelengths. No such trend is seen in our differential spectroscopy cube, thus we conclude that the feature seen is probably an artefact. The effect can not be attributed to differential atmospheric refraction, as the position of the star does not systematically vary with wavelength in individual slices of the cube.

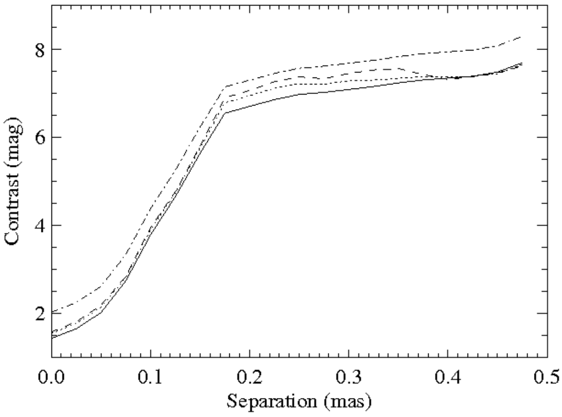

Fig. 5.5: Contrast development as a function of time after application of SDI and ADI. Solid line: average curve for one frame per angle. Dotted line: average curve for two frames per angle. Dashed line: average curve for three frames per angle. Dash-dotted line: expectation for the case of three frames per angle, if the noise had been entirely dynamic. It can be clearly seen that the development is considerably slower than in the dynamical case for almost the entire image range, hence quasi-static noise sources are significant.

5.5.3 Spectra

The H- and K-band spectra of L 449-1 were divided by a standard star spectrum in order to remove telluric features. The standard star used for this purpose was HD 55397, which is classified as a B7 giant in SIMBAD. The spectrum of the standard star was divided by a blackbody spectrum corresponding to a temperature of 13000 K, as expected from its spectral type, in order to preserve the continuum of L449-1. HD 55397 has a few spectral features of its own, which would show up as apparent emission features in the final spectrum. To remove this effect, we replaced these spectral features in the standard star spectrum with interpolation of the surrounding continuum. Local telluric information is obviously lost in these particular places, which shows up as small deviations from standard spectra in the same spectral type range.

We used the spectra to derive a spectral type, as a complement to the spectral analysis in the visual range by Scholz et al. (2005). For this purpose, we compared the H- and K-band spectra to the reference stars given in Cushing et al. (2005). The results are shown in Figs. 5.8 and 5.9. Analysis of the most prominent absorption features places L449-1 in the range between M3 and M4 – the Mg features near 1.5 μm, the K line at 1.54 μm, several FeH lines in the range of 1.6-1.7 μm, the Al doublet at 1.67-1.68 μm, the Mg line at 1.71 μm, the Ca features below 2.0 μm, the Al doublet at 2.11-2.12 μm, the Na doublet at 2.21 μm, the Ca feature at 2.27 μm and the CO bandheads at 2.3 μm and beyond are all consistently within this range. The spectral continuum is well preserved in integral field spectrographs, and also agrees well with a spectral type in the same range. Hence, we conclude that the spectral type is in the range of M3.0-M4.0, which agrees very well with the Scholz et al. (2005) characterization.

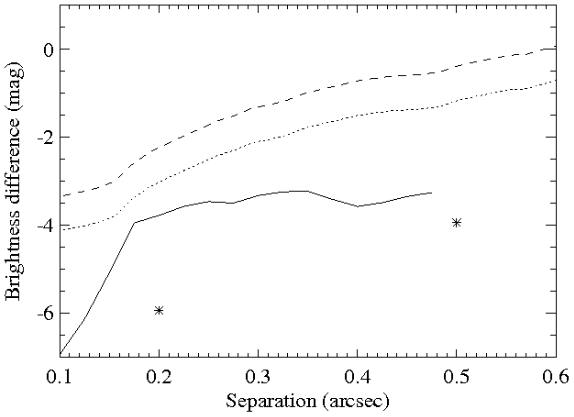

Fig. 5.6: Example comparison of physical and instrumental contrasts. The theoretical H-band contrast of a 2 $M_{\rm jup}$ companion to a 0.3 $M_{\rm sun}$ star at 100 Myr (see Baraffe et al. 1998 and Baraffe et al. 2003) has been translated into contrasts in the wavelength range of each respective instrument/method, and subtracted from the instrumental contrasts of Fig. 5.3. The planet would be detectable at any separation where an instrumental line is larger than 0 mag. NACO-SDI is clearly preferable for these cool companions (planet detectable at 0.6" and outwards). Solid line: SINFONI SDI. Dashed line: NACO-SDI. Dotted line: NACO-SDI at a common integration time. Stars: SINFONI SD.

5.6 Conclusions

We have investigated the potential of the SDI technique with SINFONI for detecting cool substellar companions to stars. It was discovered that the performance is considerably worse than for NACO-SDI under very similar circumstances. In addition, the error is partly static, leading to a poor increase of performance with increasing integration time. The quasi-static nature of the noise, along with the fact that it is constant over most of the image space, implies that non-common path aberrations and errors from the slicing and reconstruction of the image dominate the residual noise. These results, along with practical considerations, clearly lead to the suggestion that "blind" differential imaging searches for cool companions (i.e., when no a priori information is available) are presently best performed with specialized instruments such as NACO-SDI, whereas follow-up observations, where more qualitative information is desired, are better suited for integral field units such as SINFONI. The results are highly relevant for the design of the next-generation instruments for planet detection.

While the collapsed broad-band images of L 449-1 imply the existence of a low-contrast candidate companion, the absence of a clear spectral signature associated with this feature suggests that it is a PSF artefact rather than a physical object.

The spectral type of L449-1, as determined from the H- and K-band spectra, was found to be in the range of M3.0-M4.0, in close agreement with previous results (M4, Scholz et al. 2005) in the visual range.

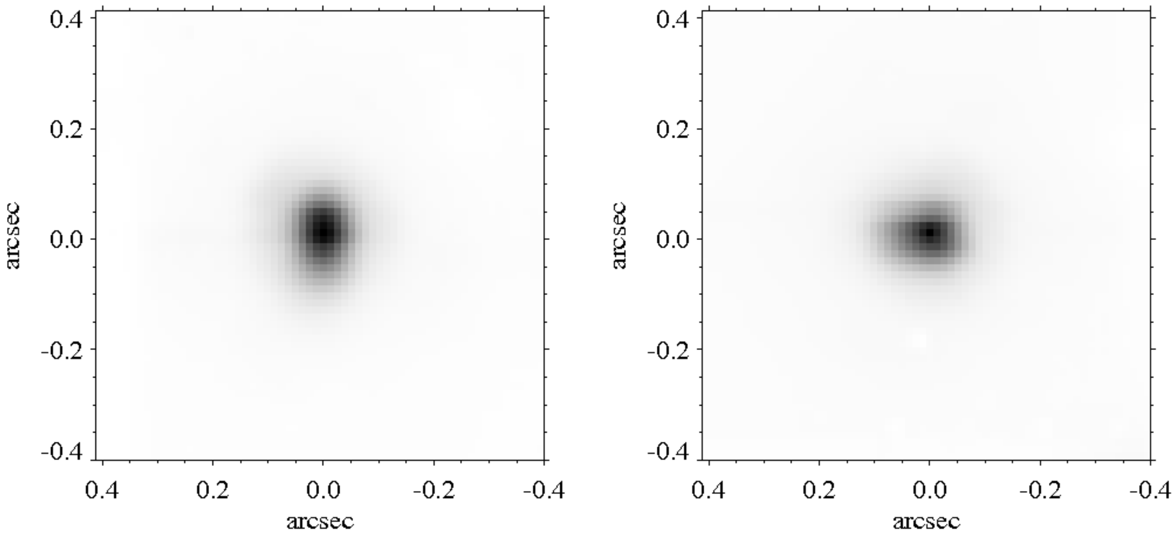

Fig. 5.7: Broad-band images covering the full wavelength range of L 449-1 at 0° (left; North is up and East is to the left) and 90° (right; North is to the right and East is up) rotation. While the images can be interpreted as suggesting the presence of a partially resolved companion, this is probably a PSF artefact.

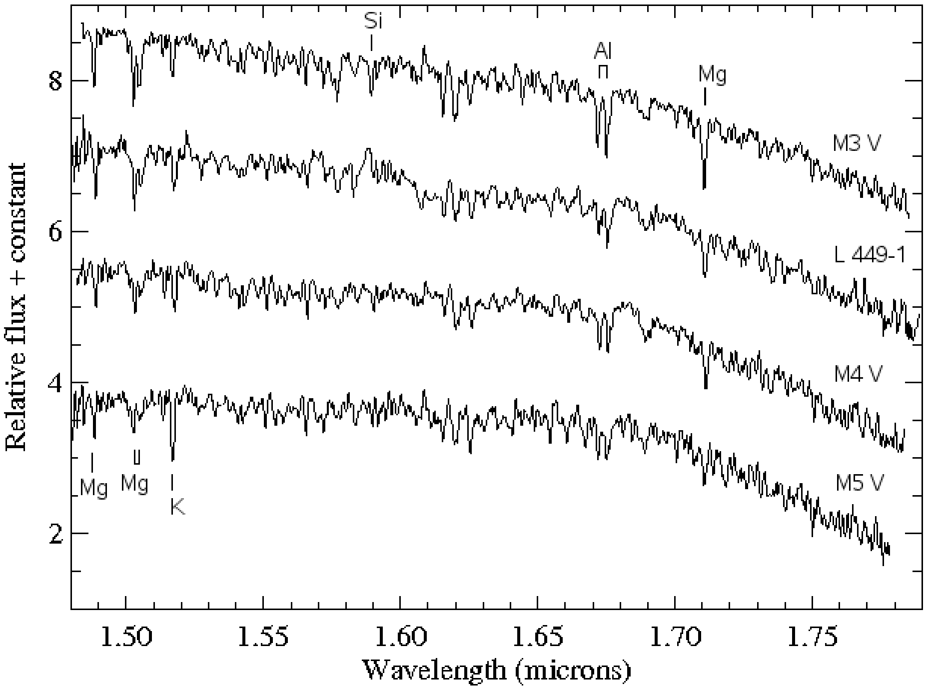

Fig. 5.8: Spectrum of L449-1 in the H-band, compared to M3, M4 and M5 standard spectra.

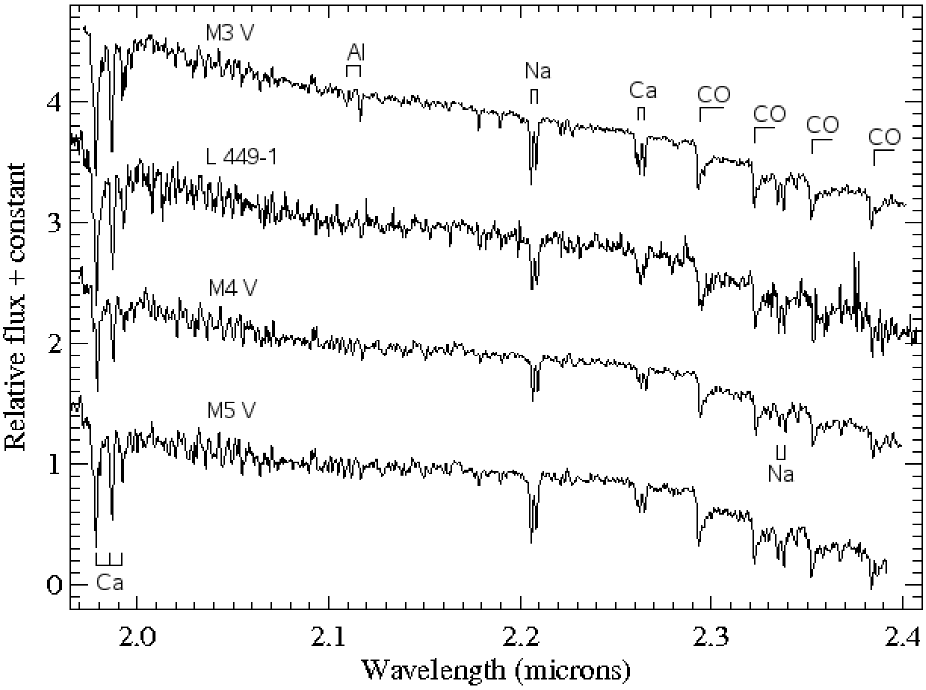

Fig. 5.9: Spectrum of L449-1 in the K-band, compared to M3, M4 and M5 standard spectra.

Tab. 5.1: Comparison of the three data sets discussed in the text.

Name	Date	Mean Seeing	Mean t_c^a [s]	Mean Strehl [1.95 μm]	$t_{\rm full}^b$ [s]	$t_{\rm eff}^c$ [s]	Correction^d
SINFONI SDI	2007 Jan 26	0.72”	37.6	34 %	1050	1050	1.00
NACO-SDI	2006 Jan 01	0.82”	12.0	48 %	4472	1050	2.06
SINFONI SD	2006 Jan 25	0.64”	–	37 %	1200	1050	1.07

[a] Correlation time t_c given by the AO system, not measured for the SINFONI SD run.

[b] The full integration time of each run.

[c] The effective comparative integration time of each run assuming SNR $\sim t^{1/2}$.

[d] The SNR correction factor given by $(t_{\rm full}/t_{\rm eff})^{1/2}$

Chapter 6

CESO: A concept for direct imaging of extrasolar Earth-like planets from the ground

From Janson (2007a): PASP 119, 214

6.1 Abstract

We present a new concept for detecting and characterizing extrasolar planets down to Earth-size or smaller through direct imaging. The NWO occulter developed by Cash and coworkers is placed in a particular geometrical setup, where fuel requirements are small, and where the occulter is used in combination with ground-based telescopes, presumably leading to an extreme cost efficiency compared to other concepts with similar science goals. We investigate the various aspects of the given geometry, such as the dynamics and radiation environment of the occulter, and construct a detailed example target list to ensure that an excellent science case can be maintained despite the limited sky coverage. It is found that more than 200 systems can be observed with 2-3 visits per system, using only a few tonnes of fuel. For each system, an Earth-sized planet with Earth albedo can be found in the habitable zone in less than 2 hours.

6.2 Introduction

Direct imaging of extrasolar planets is an area of significant scientific interest, but it is technologically challenging to achieve the necessary contrast between the planet and its parent star. While objects of a few Jupiter masses are presently detectable as companions to some stars (see e.g. Chauvin et al., 2005 and Masciadri et al., 2005), this is limited to very young and nearby systems, and rocky planets are still far from detectable by direct imaging even in such systems. There are planned projects which should have the capacity necessary for detecting Earth-like planets in the habitable zone around nearby stars. The most elaborate such projects are ESA:s Darwin (see e.g. Fridlund, 2000) and NASA:s TPF-C (see e.g. Traub et al., 2006) and TPF-I (see e.g. Beichman et al., 2006). However, these concepts are based on advanced technology under development, making their launch dates uncertain, especially considering the recent budget decrease for the TPF:s. Even regardless of these facts, it is highly interesting to investigate alternative concepts that can achieve the required accuracy at a lower cost, or generate a different scientific output that complements the output of existing or planned projects.

Whereas the thermal radiation from the planet itself at infrared wavelengths is most efficiently detected through nulling interferometry, light from the star reflected by the planet in the visual range is most efficiently detected through coronography – i.e., physically blocking out the light that originates directly from the central star, but passing through reflected light. This is indeed the basic concept of TPF-C, where the idea is to place the mask within the optical system. However, this setup requires an extreme precision of the optical system. As a means to get around this problem, a general concept that has often been proposed (see e.g. Copi & Starkman, 2000) is to put the mask (scaled up) outside of the telescope optical system, at a large separation from the telescope. There are two main challenges for such an approach: firstly, to achieve a sufficient contrast – this is severely problematic due to scattering around the edges of the occulting mask, and secondly, the geometric problem of keeping the shadow of the (necessarily space-based) occulting mask fixed with respect to the telescope during observations.

Recently, Cash (2006) have found that designing an occulter based on a certain shape that was inspired by the work of Vanderbei et al. (2003) will lead to an efficient cancellation of diffracted light such that the required Earth-to-Sun brightness contrast of about $R = 10^{-10}$ can be reached at the equivalent Earth-Sun separation for nearby stars. Thereby, the first of the problems mentioned above is solved. For the geometrical setup, Cash (2006) suggest using the occulter in combination with the James Webb Space Telescope (JWST). While this setup is appealing for many reasons, questions have been raised regarding fuel requirements for target-to-target motion, and the timescale of the concept is obviously limited by the unknown timescale of the JWST. In any case, it is clearly valuable to examine different setups for the Cash (2006) occulter concept for solutions that are even cheaper, faster, or more feasible in terms of fuel economy.

In this paper, we present such a solution, which we provisionally refer to with the self-descriptive acronym CESO (Celestial Exoplanet Survey Occulter). We use the occulter design from Cash (2006) with appropriate scaling in a particular geometrical configuration such that it can be used in combination with ground-based telescopes. We calculate the dynamics of the orbit and estimate the fuel requirements based on the various orbit alterations necessary (target-to-target motion, shadow control, orbit corrections). It is examined whether a sufficiently strong target selection can be made within the limited directability resulting from our proposed setup. Furthermore, we discuss requirements on the ground-based facility or facilities used in combination with the occulter. Finally, we place the concept in a larger scientific context and discuss how it compares with, and complements, other planet-finding concepts.

6.3 Geometry and Dynamics

The basic idea behind this concept is to place the occulter in a close to earth-leading (or earth-trailing – the result is equivalent) orbit at a distance from Earth of about $s = 1.6 * 10^9$ m, with an inclination to the Sun-Earth orbital plane of about 0.27 deg. The reasons for choosing s in such a way is described in subsequent sections – in short, it is a way of matching the motion of the occulter with the motion of Earth around its own axis, see Fig. 6.1. This is a non-equilibrium orbit, i.e. there will be a net force acting on the occulter which has to be accounted for. We will discuss this in Sect. 6.3.2. From this general orbit, the occulter will make boosts to acquire deviations within about ± 5.0 deg as seen from Earth.

The reason for this geometrical setup is that it solves two problems at once: One problem is that the occulter, regardless of orbit, will tend to move on the sky in a Keplerian manner, and so its shadow will move relative to the surface of earth. Counteracting this movement takes massive amounts of fuel. The other problem is that Earth is rotating, and so any non-polar position that a ground-based telescope has will move relative to the shadow. In the suggested setup, we largely match one movement to the other. Due to the particular choice of orbit, the velocities have approximately the same projected direction in the plane perpendicular to the line of sight, and the same size at two points of time. These points of time are separated symmetrically by a few hours from the point at which the occulter is at its closest to zenith, as seen from the ground-based telescope. Observing only within this time interval, shadow control (keeping the shadow from the star cast by the occulter at a fixed position on Earth) can be maintained during a few hours of observations with a ΔV on the order of tens of m/s, rather than hundreds of m/s as would otherwise be the case. In addition, the (corrected) orbit will approximately follow the celestial equator over the year, covering all RA:s with no additional force, and so all that has to be done for target-to-target motion is: 1) adjusting the point of time when the occulter is 'released' from shadow control so that the occulter arrival at the RA of the next target is timed with the telescope on Earth that will observe it – this takes no or an insignificant amount of extra fuel if properly planned, and 2) boosting to reach the declination of the next source. The latter maneuver obviously requires more fuel the further away from the celestial equator a given target is positioned, and so there is a trade-off between expanding the observable parameter space, and saving fuel. For reasons that will be explained in Secs 6.3.3 and 6.3.3, we use $\delta \leq \pm 5$ deg as an example throughout this text.

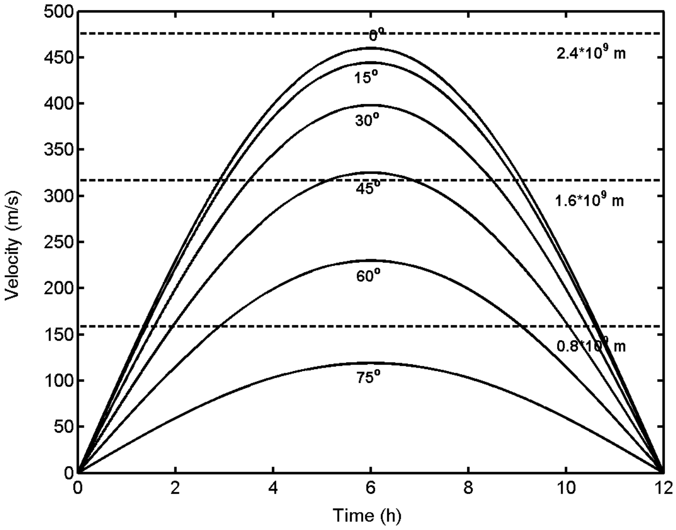

Fig. 6.1: Diagram motivating the choice of $s = 1.6 * 10^9$ m. The dashed lines are the projected velocities of the occulter at three different s, and the solid lines are the projected velocities of an observer at different latitudes. In a fuel-optimized sense, an observation of a certain target can be made between the two points where a dashed and solid line cross, and the fuel consumption is proportional to the difference between the maximum of the solid line, and the dashed line. It is readily seen that for too small s, the fuel consumption becomes unnecessarily high for observers at most latitudes (in addition, a smaller s gives a less stable orbit). For too large s, on the other hand, no observations can be made at all from any latitude. Given that most high-performance telecopes are placed within about ±30 deg latitude, $s = 1.6 * 10^9$ m provides a good balance.

6.3.1 Orbit

The orbital setup is easiest to understand by initially as a thought experiment pretending that the rotation of Earth around its axis is co-planar with the orbital motion of Earth around the Sun. We now place an occulter in an Earth-leading orbit at separation $s = 1.6 * 10^9$ m, co-planar with the Earth orbit, with the ability to make boosts such that the orbit is kept stable. How will the occulter move on the sky, as seen from Earth? The orbit is clearly co-planar with the equatorial plane of Earth, and so the occulter will always remain on the celestial equator (latitudinal dependence of an Earth-bound observer can be neglected for this part of the discussion). Since Earth and the occulter are bound to the same approximate circle around the sun, the motion of the occulter relative to Earth is a motion of constant speed along the celestial equator – after one year, the occulter is back in the same place of the sky as it started from. The angular velocity relative to Earth is thus $\Omega_\mathrm{o} = 360$ deg/yr $\approx 1.99 * 10^{-7}$ rad/s. Thus a shadow cast by the occulter from a distant star will move with a speed of $v_\mathrm{o} = \Omega_\mathrm{o} s \approx 317$ m/s relative to Earth. Projection effects from that the motion is circular rather than along a straight line are negligible over the course of a few hours. A telescope on Earth at latitude l moves with a velocity of $v_\mathrm{t} = \Omega_\mathrm{t} r_\mathrm{E} \cos(l) \sin(\theta_\mathrm{r}) \approx 460 \cos(l) \sin(\theta_\mathrm{r})$ m/s, where $r_\mathrm{E} \approx 6.37 * 10^6$ m is the equatorial radius of Earth, $\Omega_\mathrm{t} = 7.27 * 10^{-5}$ rad/s is the angular velocity of the rotation of Earth, and θ_r is the rotation angle of Earth, which is defined such that $\theta_\mathrm{r} = 90$ deg when the occulter is at its closest to zenith.

However, the rotation of Earth is not co-planar with its orbit around the sun, but tilted by about $\theta_\mathrm{t} = 23.4$ degrees. This is easily solved by proceeding like above, but giving the occulter an inclination of a small angle ϵ relative to the Sun-Earth plane as seen from the center of mass (i.e. approximately from the sun), where ϵ should be such that it maps an inclination of 23.4 degrees as seen from Earth. Since the orbit can be seen equivalently as an orbit around the sun with separation $d = 1$ AU, or an (approximate) orbit around Earth with separation s, we get that $\epsilon = \mathrm{asin}(\sin(\theta_\mathrm{t}) s/d) \approx 0.24$ deg. The occulter orbit should be such that it crosses the Sun-Earth plane at the solstices of Earth, and is at a maximum separation from the plane at the equinoxes of Earth.

In reality, there is a deviance due to the fact that an object with a constant separation from the sun, and an orbit which is inclined relative to the Earth orbit, no longer has a constant separation from Earth. To examine the extent of this effect, we formulate the spatial position vectors:

$$\vec{r}_{\mathrm{E-S}} = d \cos(\theta_\mathrm{E}) \hat{\imath} + d \sin(\theta_\mathrm{E}) \hat{\jmath} \tag{6.1}$$

$$\vec{r}_{\mathrm{o-S}} = (d^2 - z_1^2)^{1/2} \cos(\theta_\mathrm{E} + \beta) \hat{\imath} + (d^2 - z_1^2)^{1/2} \sin(\theta_\mathrm{E} + \alpha) \hat{\jmath} + z_1 \hat{k} \tag{6.2}$$

$$z_1 = d \sin(\epsilon) \cos(\theta_\mathrm{E} + \beta) \tag{6.3}$$

$$\begin{aligned} \vec{r}_{\mathrm{tel-E}} = &-((r_\mathrm{E} \cos(l))^2 - z_2^2)^{1/2} \sin(\theta_\mathrm{E}) \hat{\imath} \\ &+ ((r_\mathrm{E} \cos(l))^2 - z_2^2)^{1/2} \cos(\theta_\mathrm{E}) \hat{\jmath} + z_2 \hat{k} \end{aligned} \tag{6.4}$$

$$z_2 = r_\mathrm{E} \cos(l) \sin(\theta_\mathrm{t}) \cos(\theta_\mathrm{E}) \tag{6.5}$$

where θ_E is the orbital angle of Earth, β is the difference in orbital angle between Earth

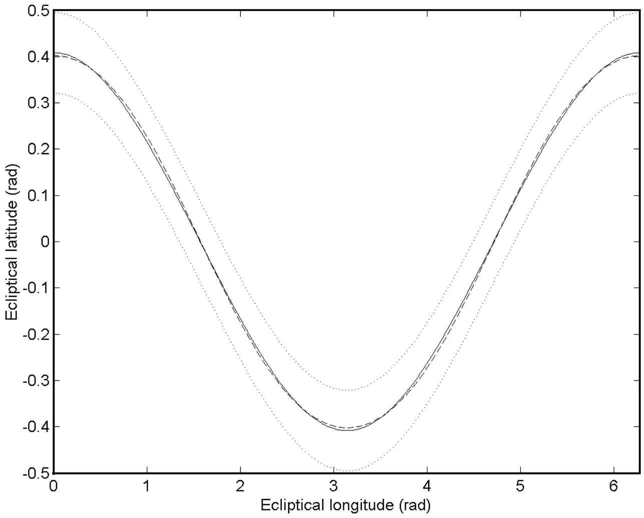

Fig. 6.2: Projected movement over one year for a ground-based telescope (solid line) and the occulter (dashed line). Also plotted are the ±5 deg limits within which the occulter will move according to our science requirements (dotted lines). The deviance in projected motion between the occulter and the telescope is clearly much smaller than the extension of the limits. This means that the deviance will be an insignificant contributor to the necessary velocity corrections.

and the occulter, $\vec{r}_{\mathrm{E-S}}$ is the vector position of Earth relative to the Sun, $\vec{r}_{\mathrm{o-S}}$ is the vector position of the occulter relative to the Sun, and $\vec{r}_{\mathrm{tel-E}}$ is the vector position of a telescope near nadir of the occulter, relative to the center of Earth. In Fig. 6.2, we plot the projected coordinates of the occulter relative to Earth ($\vec{r}_{\mathrm{o-S}} - \vec{r}_{\mathrm{E-S}}$) and a telescope ($\vec{r}_{\mathrm{tel-E}}$) in a geocentric coordinate system where α_{ES} is the angle in the Sun-Earth plane from 0 to 2π rad, and δ_{ES} is the elevation from the Sun-Earth plane from $-\pi/2$ to $\pi/2$ rad, as a function of θ_{E} over the year. We have modified ϵ somewhat to 0.27 deg, so as to spread out the deviance over the year. Also plotted are curves at ±5 deg in the δ_{ES} direction to show the size of the area over which the occulter will act. It is clear that the deviations from a perfectly co-planar orbit introduced by the non-constant separation of Earth and the occulter are much smaller that those introduced by declination alterations. Thus, the orbital corrections that must be made for the former case are negligible from a fuel economy perspective relative to the corrections that have to be made anyway for the latter case. Fuel economy issues are discussed in Sect. 6.5.

6.3.2 Dynamics

As has been mentioned, the Earth-leading (or Earth-trailing), inclined orbit is a non-equilibrium orbit which will have a net force that has to be corrected in order for the orbit to remain stable. Here we will examine the magnitude of the acceleration continuously acting on the occulter which has to be countered, and later we take this into account in the fuel economy calculations. To do this, we consider the restricted three-body problem, which has been used to e.g. derive the position of the five Lagrange Points (see e.g. Cornish, 1999), i.e. we assume that $m_{\rm o} << m_{\rm S}$ and $m_{\rm o} << m_{\rm E}$ where $m_{\rm o}$ is the mass of the occulter, $m_{\rm S}$ the mass of the Sun and $m_{\rm E}$ the mass of Earth, and consider the force field $\vec{F}_{\rm o}$ in 3D acted on the occulter.

In a frame co-rotating with the Sun-Earth system, $\vec{F}_{\rm o} = \vec{F}_{\rm g} + \vec{F}_{\rm cf} + \vec{F}_{\rm cor}$ where $\vec{F}_{\rm g}$ is the gravitational force, $\vec{F}_{\rm cf}$ the centrifugal force $\vec{F}_{\rm cor}$ the Coriolis force. They are given by:

$$\vec{F}_{\rm g} = -\tfrac{Gm_{\rm S}m_{\rm o}}{|\vec{r}_{\rm o}-\vec{r}_{\rm S}|^3}(\vec{r}_{\rm o} - \vec{r}_{\rm S}) - \tfrac{Gm_{\rm E}m_{\rm o}}{|\vec{r}_{\rm o}-\vec{r}_{\rm E}|^3}(\vec{r}_{\rm o} - \vec{r}_{\rm E}) \tag{6.6}$$

$$\vec{F}_{cf} = -m_{\rm o}\vec{\Omega}_{\rm o} \times (\vec{\Omega}_{\rm o} \times \vec{r}_{\rm o}) \tag{6.7}$$

$$\vec{F}_{cor} = -2m_{\rm o}(\vec{\Omega}_{\rm o} \times \vec{v}_{\rm o}) \tag{6.8}$$

where $m_{\rm S}$, $m_{\rm E}$ and $m_{\rm o}$ are the masses of the Sun, Earth and occulter, respectively, and $\vec{r}_{\rm S}$, $\vec{r}_{\rm E}$ and $\vec{r}_{\rm o}$ are their positions relative to the center of mass. $\vec{v}_{\rm o}$ is the velocity of the occulter. To get an explicit equation for the force as a function of position for the occulter, we put the Sun and Earth in an x-y plane along the x-axis with the rotation axis aligned with the z-axis, such that: $\vec{r}_{\rm o} = x_{\rm o}\hat{\imath} + y_{\rm o}\hat{\jmath} + z_{\rm o}\hat{k}$, $\vec{r}_{\rm S} = -\mu_{\rm E}d\hat{\imath}$, $\vec{r}_{\rm E} = \mu_{\rm S}d\hat{\imath}$ where $\mu_{\rm S} = m_{\rm S}/(m_{\rm S} + m_{\rm E})$ and $\mu_{\rm E} = m_{\rm E}/(m_{\rm S} + m_{\rm E})$, $\vec{\Omega}_{\rm o} = \Omega_{\rm o}\hat{k}$, and $\vec{v}_{\rm o} = v_x\hat{\imath} + v_y\hat{\jmath} + v_z\hat{k}$. Then, given that $|\vec{r}_{\rm o} - \vec{r}_{\rm S}| = ((x + \mu_{\rm E}d)^2 + y_{\rm o}^2 + z_{\rm o}^2)^{1/2}$ and $|\vec{r}_{\rm o} - \vec{r}_{\rm E}| = ((x - \mu_{\rm S}d)^2 + y_{\rm o}^2 + z_{\rm o}^2)^{1/2}$ and $\vec{\Omega}_{\rm o} \times \vec{r}_{\rm o} = -\Omega_{\rm o}^2 x\hat{\imath} - \Omega_{\rm o}^2 y\hat{\jmath}$ and $\vec{\Omega}_{\rm o} \times \vec{v}_{\rm o} = -\Omega_{\rm o}v_y\hat{\imath} + \Omega_{\rm o}v_x\hat{\jmath}$, and using Kepler's third law $\Omega_{\rm o}^2 d^3 = G(m_{\rm S} + m_{\rm E})$ to compactify the equation, we finally get:

$$\begin{aligned}
\vec{F}_{\rm o} = {} & m_{\rm o}\Omega_{\rm o}\left(\Omega_{\rm o}x_{\rm o} - \tfrac{\Omega_{\rm o}\mu_{\rm S}(x_{\rm o}+\mu_{\rm E}d)d^3}{((x_{\rm o}+\mu_{\rm E}d)^2+y_{\rm o}^2+z_{\rm o}^2)^{3/2}} - \tfrac{\Omega_{\rm o}\mu_{\rm E}(x_{\rm o}-\mu_{\rm S}d)d^3}{((x_{\rm o}-\mu_{\rm S}d)^2+y_{\rm o}^2+z_{\rm o}^2)^{3/2}} - 2v_y\right)\hat{\imath} \\
& +m_{\rm o}\Omega_{\rm o}\left(\Omega_{\rm o}y_{\rm o} - \tfrac{\Omega_{\rm o}\mu_{\rm S}y_{\rm o}d^3}{((x_{\rm o}+\mu_{\rm E}d)^2+y_{\rm o}^2+z_{\rm o}^2)^{3/2}} - \tfrac{\Omega_{\rm o}\mu_{\rm E}y_{\rm o}d^3}{((x_{\rm o}-\mu_{\rm S}d)^2+y_{\rm o}^2+z_{\rm o}^2)^{3/2}} - 2v_x\right)\hat{\jmath} \\
& +m_{\rm o}\Omega_{\rm o}^2\left(-\tfrac{\mu_{\rm S}z_{\rm o}d^3}{((x_{\rm o}+\mu_{\rm E}d)^2+y_{\rm o}^2+z_{\rm o}^2)^{3/2}} - \tfrac{\mu_{\rm E}z_{\rm o}d^3}{((x_{\rm o}-\mu_{\rm S}d)^2+y_{\rm o}^2+z_{\rm o}^2)^{3/2}}\right)\hat{k}
\end{aligned} \tag{6.9}$$

We can now put in various positions for the occulter to find the net force – and thus, the net acceleration $a_{\rm dyn} = F_{\rm o}/m_{\rm o}$ – at any point. We find that for $y_{\rm o} = 1.6 * 10^9$ m, $d\cos(\epsilon) < x_{\rm o} < d$ m, $0 < z_{\rm o} < d\sin(\epsilon)$ m, and assuming that $|\vec{v}_{\rm o}| < 100$ m/s (which, as we will see, is smaller than any velocity imposed on the occulter within the orbital plane) and always pointing in the least favorable direction (i.e. in the direction that maximizes the net force), the net acceleration $a_{\rm dyn} < 2 * 10^{-4}$ m/s^2. If $y_{\rm o}$ is increased, the acceleration is even lower. We discuss the corrections needed to compensate this in the following section.

6.3.3 Required ΔV

Given the reasoning in the previous sections, we can now estimate the size of the velocity corrections needed for target-to-target motion ($\Delta V_{\rm tt}$), shadow control ($\Delta V_{\rm sc}$) and orbit corrections ($\Delta V_{\rm oc}$).

Target-to-target motion

As previously mentioned, the fuel-demanding component of target-to-target motion is a boost from the declination of the previously observed target to the declination of the next one, followed by an equal boost in the opposite direction when the next target is reached. The ΔV_{tt} required for this depends on the average declination difference δ_{diff} and the average time spacing t_{diff} (recall that the occulter moves automatically along the right ascension direction) between one source and the next as $\Delta V_{\mathrm{tt}} = 2s \sin(\delta_{\mathrm{diff}})/t_{\mathrm{diff}}$. Assuming that the declinations of the targets are randomly distributed with a uniform distribution, the mean δ_{diff} is 1/3 of the width of the declination band (because the mean difference of two uniform equally distributed random variables is 1/3 of the distribution width). By clever planning, in particular if the number of interesting sources is larger than the number of sources that are going to be observed, the number 1/3 can probably be made considerably smaller, but we will keep it as it is throughout this paper.

Note that ΔV_{tt} depends quite strongly on t_{diff}, for the following reason: We assume that 200 sources will be observed, and that this can be done over a time span of 4 years (i.e. $t_{\mathrm{diff}} \approx 1$ week), or 2 years (i.e. $t_{\mathrm{diff}} \approx 0.5$ weeks). If the time span is 4 years, we can divide the declination space into 4 stripes, each of width 2.5 deg, and reside in one per year, giving $\delta_{\mathrm{diff}} \approx 0.83$ deg. If the time span is instead 2 years, we can equivalently divide the declination space into 2 stripes, that are twice as wide, doubling ΔV_{tt}. In addition, t_{diff} is halved, again doubling ΔV_{tt}. In other words, for a constant sample size, it is roughly the case that $\Delta V_{\mathrm{tt}} \sim t_{\mathrm{diff}}^{-2}$.

We consider two examples: first, we assume $\delta_{\mathrm{diff}} = 0.83$ deg, $t_{\mathrm{diff}} \approx 1$ week and $s = 1.6 * 10^9$ m, giving $\Delta V_{\mathrm{tt}} \approx 2 * 38.5$ m/s. As a second example, we use $\delta_{\mathrm{diff}} = 1.66$ deg, $t_{\mathrm{diff}} \approx 0.5$ weeks and the same s giving $\Delta V_{\mathrm{tt}} \approx 2 * 154$ m/s. While this latter case gives a velocity higher than 100 m/s, it points mainly along the rotation axis and so does not violate the condition we set in Sect. 6.3.2 for the Coriolis force.

There is also an additional effect for non-zero declinations. Just before entering shadow control, an occulter outside of $\delta = 0$ deg has to have a declinational velocity of a declination-dependent size (see the end of Sect. 6.3.3) pointed towards the celestial equator, and after exiting shadow control the occulter will have a velocity of the same size, but in the opposite direction. These velocities largely cancel out in terms of fuel economy, because half of the time the occulter will come from a lower declination towards the star, such that it has to spend extra fuel to acquire the right inital velocity, but the other half of the time, the occulter will approach the star from a higher declination, such that less fuel has to be spent to acquire the correct velocity. The same argument also holds for the velocity the occulter has when it exits shadow control, and is going either to a higher or lower declination. However, there is a small differential effect due to the fact that the targets at the highest declinations, which require the highest initial velocities for shadow control, will more often than not be approached from a lower declination. In an extreme hypothetical case where half of the stars are positioned at $\delta = +5$ deg, and the other half at $\delta = -5$ deg, the velocity correction to be added to V_{tt} would be $2 * 7$ m/s. However, the stars are randomly distributed (adding a factor 1/3 as before), and the area is divided into declination bands, so the real corrections for our examples are $2 * 7/12 \approx 2 * 0.6$ m/s for $t_{\mathrm{diff}} \approx 1$ week, and $2 * 7/6 \approx 2 * 1.2$ m/s for $t_{\mathrm{diff}} \approx 0.5$ weeks.

As a generous final estimation, we therefore set $\Delta V_{\rm tt} \approx 2*40$ m/s for $t_{\rm diff} \approx 1$ week, and $\Delta V_{\rm tt} \approx 2*160$ m/s for $t_{\rm diff} \approx 0.5$ weeks.

Shadow control

'Shadow control' means the boosts necessary for the occulter to keep the shadow from a distant star fixed with respect to a ground-based telescope during observations. Due to the orbital configuration of the occulter, this orbit control component can be kept reasonably small. The idea is illustrated in Fig. 6.3. By starting to boost when the projected velocity of a telescope on Earth becomes equal to the normal speed of the occulter, and following the telescope movement over the maximum until they again become equal, after which the occulter is 'released' back to normal movement, $\Delta V_{\rm sc}$ can be kept to a few tens of m/s per target for a few hours of observing. It is clear from the figure that $\Delta V_{\rm sc} = 2*(\max_{\theta_{\rm r}}(v_{\rm t})-v_{\rm o}) \approx 2*(460\cos(l) - 2*10^{-7}s)$. Minimization of $\Delta V_{\rm sc}$ is a trade-off versus maximization of the total integration time $t_{\rm tot}$ for the source. $t_{\rm tot} = 2(t_{\rm max} - t_{\rm cr})$, where $t_{\rm max} = 6$ h is the time of maximum speed and $t_{\rm cr}$ is the crossing time of the velocities of the occulter and telescope. Setting $\theta_{\rm cr} = \Omega_{rmt} t_{\rm cr}$, it is the case that $460\cos(l)\sin(\theta_{\rm cr}) = 2*10^{-7}s$, such that:

$$t_{\rm tot} = 2\left(t_{\rm max} - 1.38*10^4 {\rm asin}\left(\frac{2*10^{-7}s}{460\cos(l)}\right)\right) \tag{6.10}$$

It is obviously in our interest to have as high total integration time as possible, but on the other hand, a lower $\Delta V_{\rm sc}$ gives a larger amount of observable targets in total. As an example, we assume two telescopes at $l = \pm 29.5$ deg (one observing during northern winter season and one during southern winter season), and $s = 1.6*10^9$ m, giving $\Delta V_{\rm sc} \approx 2*80$ m/s, over $t_{\rm tot} \approx 4.9$ hours, of which about 2 hours or more (depending on the time of year) should be possible to use as effective integration time.

There is an additional component to velocity correction for shadow control when the declination is non-zero, given by $2*460(1-\sin(\theta_{\rm r}))\cos l \sin(\delta)$. For the extreme cases at $\delta = \pm 5$ deg, this is $2*7$ m/s in our example (see also Sect. 6.3.3 for its effect before and after shadow control). Since this is always more than 10 times smaller than, and perpendicular to, the main velocity component during shadow control, this effect is negligible here. It does, however, start to become significant if the declination limits are set even higher.

Orbit corrections

The main contribution to necessary orbit corrections is the stability correction, discussed in Sect. 6.3.2. There, we found a maximum net acceleration of $a_{\rm dyn} = 2*10^{-4}$ m/s^2. We now assume that this acceleration is constantly acting on the occulter (which is an overestimation). For a fixed number of targets, the magnitude of the corrections that have to be performed is obviously smaller the shorter the total time-span (and thus shorter time spacing $t_{\rm diff}$) of the survey. Thus minimizing the orbit corrections constitutes a trade-off versus minimizing the target-to-target corrections. $\Delta V_{\rm oc} \sim t_{\rm diff}$, and $\Delta V_{\rm tt} \sim t_{\rm diff}^{-2}$, so minimizing

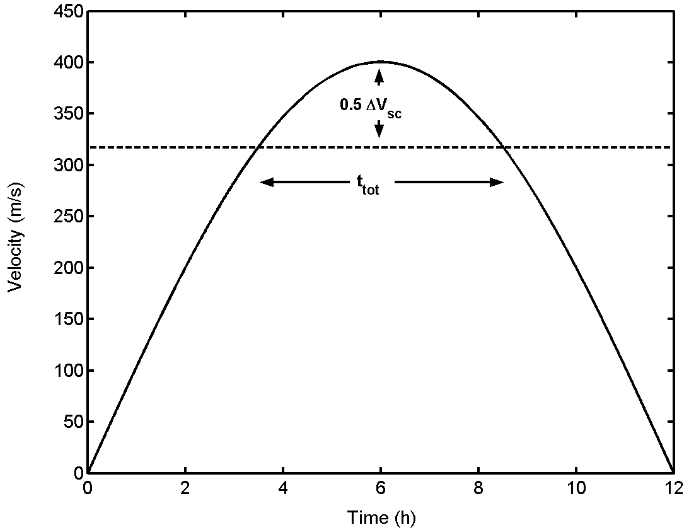

Fig. 6.3: Example of shadow control. The non-forced projected velocities of the occulter (dashed line) and a ground-based telescope (solid line) are plotted over a range of 12 hours around an observation. In the simplest case, the occulter simply starts to boost when the curves cross, first accelerating to keep up with the pace of the telescope until the point of maximum velocity, then decelerating until it reaches normal velocity, after which it is 'released' from shadow control. Observations can take place between the two crossings.

$\Delta V_{\rm tt}$ is the dominating criterion in this regard, but on the other hand, there are other reasons for keeping $t_{\rm diff}$ small, such as deterioration of mechanical and electronic components of the occulter, and the wish to benefit from the scientific output as soon as possible. Following our examples from Sect. 6.3.3, we use $t_{\rm diff} \approx 1$ week to get $\Delta V_{\rm oc} = a_{\rm dyn} t_{\rm diff} \approx 120$ m/s, and $t_{\rm diff} \approx 0.5$ weeks to get $\Delta V_{\rm oc} \approx 60$ m/s in total between one target and the next. While the total velocity in the former example exceeds 100 m/s in total, the corrections will be spread out such that it never violates the condition set in Sect. 6.3.2 for the centrifugal force.

Another source of orbital disturbance is the radiation pressure. However, even though the occulter has a very large area, this is a very minor contributor, since the occulter can remain perpendicular to the solar radiation for most of the time. Even so, using extreme 'worst case' parameters (a collecting area of 10^5 m^2, mass of only 500 kg and radiation pressure of 5 μPa), the acceleration is 10^{-4} m/s^2, which is smaller than the dynamical contribution that acts constantly. The radiation pressure component is easily fit within the generous $\Delta V_{\rm oc}$ derived from dynamical arguments.

6.4 Occulter properties

We use the same occulter design type as given in Cash (2006), and so no extensive discussion will take place here regarding details that are not different from there. To give an example of the expected occulter parameters, we use the contrast equation given by Cash (2006):

$$R = \left(\frac{n!}{r^{2n}} \left(\frac{s\lambda}{2\pi} \right)^n \right)^2 \tag{6.11}$$

and set $n = 6$ and $s = 1.6 * 10^9$ m. Requiring that $R = 10^{-10}$ at $\lambda = 0.7$ μm and $R = 10^{-8}$ at $\lambda = 1$ μm leads to $r = 60$ m, and $IWA = 15.5$ mas. Here, n is an integer set by the shape of the petals that extend from the central obscuring disk, which cancel out diffraction. R is the brightness contrast between secondary and primary, and r is the radius of the central disk, with the petals extending about equally far beyond that, i.e. the total radius of the occulter is $2r = 120$ m. We reiterate that the parameters given here are just examples to show that a feasible paramater space exists. Future work will aim at finding parameter settings that optimize CESO from an engineering perspective. The parameters can be adapted to different geometries mainly by changing s and adjusting r accordingly to fulfill R. While it is in principle also possible to loosen the constraint on λ to decrease r, attention should be paid to the fact that ground-based telescope performs better at longer wavelengths due to how the Strehl ratio varies with wavelength. We give a brief description of an aternative example in the end of section 6.9.

The occulter would probably consist of an opaque membrane on a low-weight solid skeleton, and as such the payload mass could be kept rather low despite the large surface size. For fuel budget considerations, we will assume a payload mass of $m_{\rm pl} = 500$ kg, and a total (orbit-inserted) mass of fuel plus payload of $m_{tot} = 5000$ kg. As we will see in the following section, our primary example is to use magnetoplasmadynamic (MPD) thrusters for the propulsion. This requires an external energy source with an output power of 1 MW (for the particular example used here – see Sect. 6.5). We can provide this by using the occulter surface for absorbing solar energy – assuming that the full surface ($A_{\rm cd} \approx 22600$ m^2) is used for such a purpose, that the efficiency is about $\eta = 20$ %, and given the solar constant (recall that the occulter is at roughly 1 AU separation) of $S = 1370$ W/m^2, we get $P_{\rm out} = A_{\rm cd}\eta S = 6.2$ MW. For the case of shadow control, the occulter surface can however not be in a plane perpendicular to the incoming solar radiation, because then it would be approximately edge-on as seen from Earth and thus useless for occulting the star to be observed. However, we can solve this problem with a geometrical setup illustrated in Fig. 6.4. By tilting the occulter during observations by a small angle ϕ, the occulter can receive a sufficient amount of radiation on the side that is turned away from Earth (with no sunlight being scattered towards Earth). If we assume that the full occulter surface can receive 6.2 MW, we can use a tilt such that the sun 'sees' 17 % of that surface – a condition which is fulfilled at $\phi \approx 10$ deg. Intuitively, this implies that the occulter surface needs to be extended along the tilted axis by a factor $1/\cos(\phi)$ – i.e., that the occulter needs to be elliptical with $r_{\rm minor} = 60$ m and $r_{\rm major} = 61$ m. However, Cash (2006) demonstrate that the difference in projected area towards Earth imposed by a small tilt is well within the error tolerance, hence it may be possible to keep the occulter circular.

During shadow control, it is obviously necessary for the occulter to be placed correctly in the plane of the sky such that the shadow falls on top of the telescope. We do not treat the precision aspect with any great detail, but note that the radial distance off-axis over which sufficient contrast is maintained can be quite large, depending on n (see Cash 2006). In the NWO example of Cash (2006), the tolerance is on the order of several meters, and in

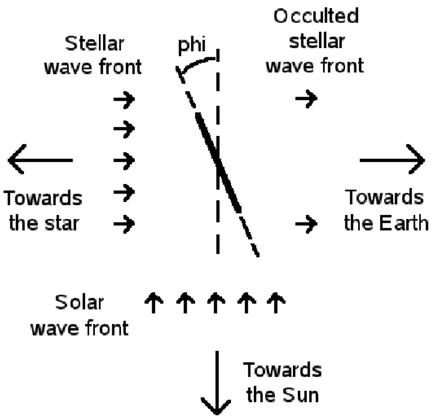

Fig. 6.4: Geometrical setup for the occulter with respect to the Earth, the sun and a distant star. The occulter receives sunlight on the far side of the occulter, such that it can power its propulsion system, yet not scatter any solar radiation towards Earth.

our case, it would be even bigger, since the shadow is larger. Thus the precision required is macroscopic, and we do not expect it to constitute a major problem.

6.5 Propulsion and fuel budget

For a minimum amount of fuel spent per target observed, it is desirable to use a propulsion system with as high exhaust velocity as possible. In addition, the system must be able to generate a sufficient thrust to be able to accelerate the occulter to a given speed in a given time. For shadow control, the maximum acceleration is just at the beginning and end. Derivation of the velocity with respect to time gives an acceleration of $1.78 * 10^{-2}$ m/s^2 in our example, and thus for $m_{\text{tot}} = 5000$ kg, the required thrust $F_{\text{req}} \approx 89$ N (see Fig. 6.5). For target-to-target motion and orbit corrections, the needed thrust is obviously smaller even though the velocities are higher on average by a factor 2-3, since they occur over $t_{\text{diff}} \approx 0.5$ to 1 weeks, rather than a few hours, as in the case of shadow control. Still, the required acceleration is sometimes considerably larger than average in the case of target-to-target motion, and so a margin to the average requirement is in order. In all, we set $F_{req} \approx 100$ N as a requirement on the propulsion system to ensure that it can handle all the necessary maneuvers.

Magnetoplasmadynamical (MPD) thrusters have been shown to be able to generate a thrust of 100 N and an exhaust velocity of $v_{\text{ex}} = 100000$ m/s using 1 MW of power (see e.g. `http://www.nasa.gov/centers/glenn/about/fs22grc.html`). As we have demonstrated, such a power is within reach. Thus, MPD thrusters are an excellent choice of propulsion for this purpose.

For finding the number of targets we can observe under the assumptions we have done so far, we use Tsiolkovsky's rocket equation iterated backwards, from the point where all the fuel is spent, up to the point of orbit insertion:

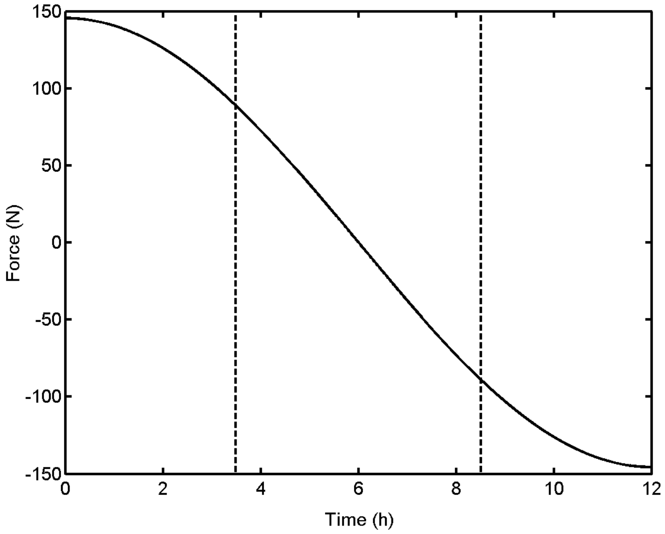

Fig. 6.5: The required thrust for forced motion as a function of time (solid line) corresponding to our example in Sect. 6.3.3, using a mass of $m_\mathrm{o} = 5000$ kg. Given the same starting and ending times as in that example (dashed lines), the maximal required thrust is about 89 N.

$$K = \mathrm{e}^{(\Delta V_\mathrm{tt} + \Delta V_\mathrm{sc} + \Delta V_\mathrm{oc})/v_\mathrm{ex}} \tag{6.12}$$

$$m_{i+1} = m_i K \tag{6.13}$$

where $m_0 = 500$ kg, and the iteration is interrupted when $m_N \geq 5000$. N is the number of visits possible, i.e. N different targets can be observed if each target is observed once, $N/2$ different targets if each target is observed twice, and so on. Following our two different examples from Secs 6.3.3 to 6.3.3, we find that if $t_\mathrm{diff} = 0.5$ weeks and the total number of *different* sources is 200, then $N = 427$, and if $t_\mathrm{diff} = 1$ week, then $N = 599$ – i.e., about 2 observations per source in the former case and about 3 per source in the latter. Note that if we set the constraint that we only observe each target once, then N for each respective t_diff is even larger, because then we can set a smaller δ_diff and thus decrease ΔV_tt. Note also that even though $t_\mathrm{diff} \approx 1$ week looks clearly preferable here with a larger N, the total timespan of the mission in that case becomes about 12 years. In the case of $t_\mathrm{diff} \approx 0.5$ weeks, the total span is only about 4 years, which is probably more realistic. In a real application, t_diff should obviously be set to fit the expected lifetime of the craft. In any case, it is obvious that a large number of sources can indeed be observed with just a few tonnes of fuel. In Sect. 6.7, we will see that an excellent target list can also be achieved within the constraints set.

6.6 Ground-based telescope properties

To reach a contrast of $\sim 10^{-10}$ with a coronagraph-equipped, ground-based telescope would be pathologically difficult, not just due to the precision required for the mask and optical system, but also due to the fact that once the light from a distant system has entered the atmosphere, the wavefront is aberrated such that part of the phase information is lost. Thus, it becomes impossible for a coronagraph to discern which part of the light originates from the star and should be blocked out, and which part comes from a fainter companion close by the star and should be let through. An adaptive optics system with an extremely high Strehl ratio would be required for a sufficient restoration of the wavefront such that this approach would be practical. In our setup, this problem is circumvented – the coronography is performed in space, so that the star is already invisible in the wavefronts that hit the atmosphere. An implementation of CESO would revolutionize the role of ground-based telescopes in planet imaging – Earth-equivalent planets could now be detected with present-day telescopes, a task which has been demonstrated to otherwise be essentially impossible even with the next-generation 'extremely large telescopes' (see Berton et al., 2006a)!

Essentially any telescope can be used in combination with the occulter, and different telescopes can be used for different targets, as long as the occulter 'knows' this prior to observing the preceding target, such that the velocity corrections can be adjusted accordingly. There are however some requirements that should be fulfilled for an optimal scientific output. As we have already seen, the telescope latitude has an effect on $\Delta V_{\rm sc}$ and $t_{\rm diff}$, but these quantities are also affected by s, so appropriate solutions exist for a wide range of latitudes. Of more importance are the telescope size and instrumentation. The telescope size is important mainly for suppressing the noise to the greatest possible extent during the limited time of observation – the noise is expected to be photon noise dominated once the central star is properly blocked out, and so the signal-to-noise ratio SNR should scale with telescope diameter $d_{\rm tel}$ roughly as $SNR \sim d_{\rm tel}$.

For instrumentation, it is first of all necessary for the telescope to be equipped with a visible adaptive optics (AO) system, so that planets in multiple systems can be resolved from each other. Due to the fact that Strehl ratio decreases with decreasing wavelength, visible AO is necessarily more challenging than infrared AO in terms of achieving high Strehl ratios. However, since we are only dealing with resolving planets from each other, we are not in a high-contrast imaging context, and so a high Strehl ratio is as such not necessary, as long as some small fraction of the light is approximately diffraction limited. The AO system should preferably be complemented with a Laser Guide Star (LGS) system, since we block out the central star during observations, and it can not be guaranteed that there is any sufficiently bright natural guide star nearby. An interesting alternative to using LGS, however, is to equip the occulter itself with a collimated light source which only emits in a wavelength region outside of the region where the scientific data is being collected. The wavefront sensing can then make use of this light, whereas the science data remains unaffected. Using such a procedure would yield a higher quality wavefront correction, since we get rid of effects such as the cone effect, which occur with LGS systems. A laser on the occulter would obviously need to be accounted for in the mass and power budgets. In any case, it would of course be useful with LGS systems on the ground either way, if not else as a redundancy factor.

While not necessary, it would be hugely beneficial to use an integral field spectroscopy unit for observations. This allows for acquiring spectral information of any object detected, without a priori knowledge of its position. As an example during this text, we will assume that the planned second generation VLT instrument MUSE is used (planned to be in operation from

2012 and onwards, see Bacon et al., 2006). The MUSE narrow-field mode, while designed primarily for extragalactic purposes, is excellently suited for our requirements. It covers a wavelength range of 465 nm to 930 nm with a Strehl ratio of 5 % (goal 10 %) at 750 nm. The spectral resolution is given as 2000 at 465 nm, and 4000 at 930 nm in Bacon et al. (2006). Presumably, observing over the whole wavelength range at once would therefore lead to a resolution of $\sim$ 1000, which is more than necessary. Obviously, it can be undersampled so as to adapt to the sensitivity reached for each individual object detected. The spatial resolution of MUSE is 42 mas at 750 nm, and the spatial sampling is 25×25 mas^2/pixel. The field of view is 7.5 arcsec by 7.5 arcsec. In 1 hour, the instrument reaches a 5σ sensitivity for a flux of $2.3 * 10^{-18}$ erg/s/cm^2 (i.e. 10σ in 1 hour for $f_{\rm lim} = 4 * 2.3 * 10^{-18}$ erg/s/cm^2, which we will use in Sect. 6.7).

Even for the faintest detectable objects, where the resolution is $\sim$ 10 or less at a sufficient accuracy, it is useful to still have that spectral information, since it helps determining (along primarily with proper motion from one epoch to the next) if the detected object is really a member of the system observed, or a background object that is there by chance. Background stars would obviously show blackbody spectra corresponding to their temperature, which is easily determined with a few data points. Note that e.g. an Earth-size planet at 1 AU reflecting roughly equally over all wavelengths (thus mimicking the blackbody spectrum of its parent star) could hardly be mixed up with a background star in the general case: a background star with the same temperature but $\sim 10^{10}$ times fainter would have to be $\sim 10^5$ times further away (unless the foreground star is a giant), i.e. at a distance of $\sim$ 1 Mpc, which is not a reasonable place to find a single star by chance. The spectral information could also assist in rejecting deep field galaxies, though simulations for the NWO (see Schindhelm et al., 2005) have shown that these are mostly extended, and sparse enough that they will not create a problem in the general case anyway.

As we have already mentioned, at least two telescopes would be needed – one on the northern, and one on the southern hemisphere – since we wish to always observe in the winter half of the year. A larger amount of telescopes with appropriate instrumentation could also be useful, opening up the possibility to optimize the latitude with respect to each source (i.e. trading integration time versus $\Delta V_{\rm sc}$), and loosening constraints on the R.A. speed. It could also be used to gain redundancy versus bad weather, though this requires a certain amount of forecasting to be effective. Once the occulter has reached a star, with its shadow covering a certain telescope site, if that site is clouded out, the system will simply not be observable at that time, and all that can be done is to move on to the next system. If the weather is known somewhat in advance, the speed of the occulter can be adjusted so as to reach a more appropriate site. To save the most amount of fuel in this regard and gain total safety from bad weather, it would be required to be able to forecast the weather over a timescale of about $t_{\rm diff}$. This is obviously another reason not to keep $t_{\rm diff}$ too large.

We do not go into details of what telescopes or sites should be used, suffice to say that either existing telescopes could be equipped with appropriate instrumentation (e.g. MUSE for VLT), or new telescopes could be built, or a combination of the two. A telescope diameter of 8 meters or more would be required for the kinds of science cases presented here.

6.7 Target sample

In this section, we show that a highly interesting target list can be achieved, even with the limited directability of the survey. Although an exact target list is premature, we have compiled a quite detailed example list to ensure that the science case is both strong and realistically attainable. As a first sample selection, we use the HIPPARCOS catalog and select all stars with $|\delta| \leq 5$ deg, and which fulfill either parallax $p > 50$ mas, or $p > 13$ mas with the additional condition that V-band magnitude $V < 10.1$ mag. This gives 3532 stars, shown in an HR-diagram in Fig. 6.6. For each of these stars, we calculate the absolute magnitude as $V_{\mathrm{abs}} = V - 5\log_{10}(d_{\mathrm{star}}) + 5$, where $d_{\mathrm{star}} = 1000/p$ in units of pc. Furthermore, we use the $B - V$ color also measured by HIPPARCOS to assign a spectral type to each star using standard absolute B- and V-band magnitudes B_{std} and V_{std} for each respective spectral type. Based on the spectral type, each star is assigned a temperature T, and brightness deviance $\Delta_{\mathrm{mag}} = V_{\mathrm{std}} - V_{\mathrm{abs}}$. Based on this and the standard luminosity L_{std} for each spectral type, we calculate the luminosity as $L = L_{\mathrm{std}} * 10^{\Delta_{\mathrm{mag}}/2.5}$ and subsequentially the radius (assuming perfect blackbodies) from the Stefan-Bolzmann law $R_{\mathrm{star}} = (L/(4\pi\sigma_{\mathrm{s}}T^4))^{1/2}$. The flux within the wavelength regime that we can observe (465 to 930 nm) sent out by an Earth equivalent (same radius, albedo and separation from the sun as Earth) on average is then given by $f_{\mathrm{EE}} = q f_{\mathrm{vis}} R_{\mathrm{star}}^2 / d_{\mathrm{star}}^2$, where $q \approx 3.34 * 10^{-10}$ is the flux ratio between an Earth equivalent at half-lumination and its parent star, and f_{vis} is the blackbody spectrum $B(\lambda, T)$ for the star integrated from 465 to 930 nm. Using units of erg/s/cm^2 for f_{EE}, the integration time t_{int} in hours for a 10σ detection of an Earth equivalent for each star is thus given by $t_{\mathrm{int}} = f_{\mathrm{EE}}/f_{\mathrm{lim}}$. Note that in our example occulter parameters, a contrast of 10^{-10} is not provided for the full available spectral range, but only for half of it. In the worst case, this leads to that t_{int} corresponds to a $10\sigma/\sqrt{2} \approx 7\sigma$ detection. We will conservatively use this number for the rest of the section. However, note that this problem becomes smaller as we move radially outwards from the IWA, as the residual stellar flux decreases in this manner.

In our selection of appropriate targets, we wish to give merit to systems in which terrestrial planets can be detected in the vicinity of the habitable zone. For this purpose, we use a loose definition of the habitable zone where the logarithmic center is at a stellar separation of $r_{\mathrm{hz}} = (L/L_{\mathrm{sun}})^{1/2}$ in units of AU, and the inner and outer edges are given by $r_{\mathrm{hz,in}} = 0.5 r_{\mathrm{hz}}$ and $r_{\mathrm{hz,out}} = 2.0 r_{\mathrm{hz}}$, respectively. Constantly assuming that a given planet has the same radius and albedo as Earth, we now calculate the integration time t_{hz} needed for a 7σ detection of such a planet that resides in the habitable zone, and yet is at least just far enough separated from its star that it does not fall inside of the IWA. In other words, if $r_{\mathrm{hz,in}}/d_{\mathrm{star}} > IWA$, then $t_{\mathrm{hz}} = t_{\mathrm{int}}(r_{\mathrm{hz,in}}/1\ \mathrm{AU})^2$. If $r_{\mathrm{hz,out}}/d_{\mathrm{star}} > IWA > r_{\mathrm{hz,in}}/d_{\mathrm{star}}$, then $t_{\mathrm{hz}} = t_{\mathrm{int}}(IWA d_{\mathrm{star}}/1\ \mathrm{AU})^2$. If $IWA > r_{\mathrm{hz,out}}/d_{\mathrm{star}}$, then planets are obviously not observable in the habitable zone at all, and thus t_{hz} is set to infinity in those cases.

After de-selecting known binaries with inappropriate separations from the sample (see discussion below), we use the criterion of minimizing t_{hz} for selection of our sample. Since we gave a minimum effective integration time per source of 2 hours in Sect. 6.3.3, we can for instance simply set the requirement that a planet with Earth radius and albedo has to be detectable within the habitable zone at 7σ in less than 2 hours, i.e. $t_{\mathrm{hz}} < 2$ hours. This gives a final sample of 407 stars, see Fig. 6.7. A subset of this would constitute an excellent

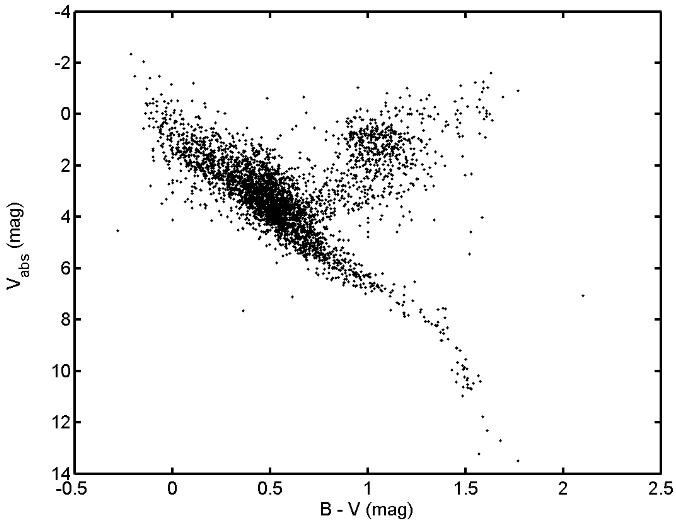

Fig. 6.6: An HR-diagram of a distance- and (partly) brightness-limited sample of HIPPARCOS stars between -5 and +5 degrees declination.

sample for our example survey in Sect. 6.5 with about 200 target stars, each visited about 2-3 times. The sample is also easily extended by e.g. loosening the constraint somewhat on $t_{\rm hz}$, or by including sources that are interesting for other reasons than having a low $t_{\rm hz}$. In addition, since HIPPARCOS is incomplete from about $V = 9$ mag and below (see Perryman et al., 1997), there are nearby cool stars that were not included in the HIPPARCOS catalog, but that nonetheless have a low $t_{\rm hz}$. One known such example is G 99-49, an M3.5-star with $V = 11.31$ mag and $p = 190.9$ mas according to RECONS (see Henry, 2006), which we find to have a $t_{\rm hz}$ of much less than 2 hours due to its proximity and late type.

The $t_{\rm hz}$ condition is a physically appealing criterion for finding habitable planets. It also automatically exploits the fact that the technique of detecting reflected light from planets in the habitable zone is in fact well suited for a large range of stellar masses, which is due to the following reason: lower-mass stars are intrinsically fainter, and thus a reflecting planet at a given distance is fainter as well. On the other hand, for lower-mass stars the habitable zone is located further in towards the star, and thus a larger fraction of the stellar light is reflected. In addition, lower-mass stars are more common, such that the number density is large enough that a significant number of sources are close enough to us that the habitable zone is outside of the IWA, despite the small physically separation. Equivalently, higher-mass stars are intrinsically brighter, meaning that planets in the habitable zone are sufficiently bright in a significant number of systems to be detected even though the zone is further out. Meanwhile, the larger physical separation and higher brightness mean that the systems can be observed at greater distances from Earth, such that a significant number of systems exist despite the smaller number density. This effect is clearly seen in Fig. 6.9.

An effect that is not included in the $t_{\rm hz}$ criterion is the fact that as the habitable zone moves outwards, the brightness contrast for a planet in the habitable zone to the star decreases, such that for the most massive stars in the sample (and the giants), a contrast of 10^{-10} may not

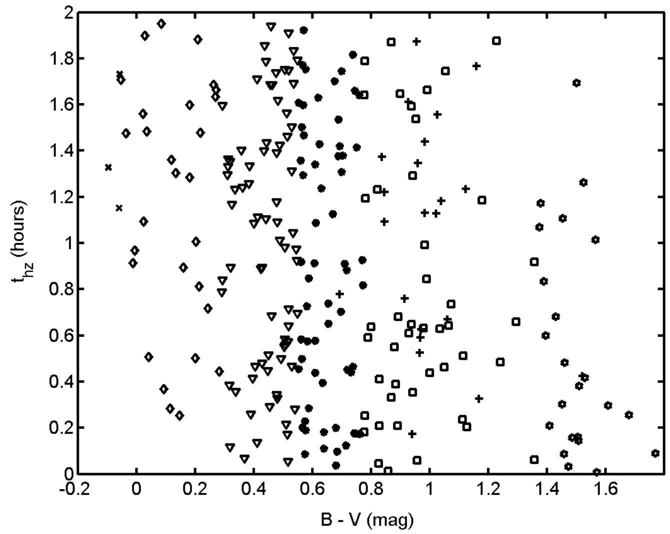

Fig. 6.7: t_{hz} versus the $B-V$ colors for the stars in our final example sample. The distribution of stars clearly peaks at the late-F/early-G boundary. For easier recognition of different classes of stars in this and other figures dealing with this sample, we use the following symbolics: B-stars are marked with 'x' marks, A-stars with diamonds, F-stars with triangles, G-stars with asterisks, K-stars with boxes, M-stars with hexagrams, and giants with '+' marks. Giant stars are defined as having $\Delta_{\mathrm{mag}} > 3$ mag, see Fig. 6.8.

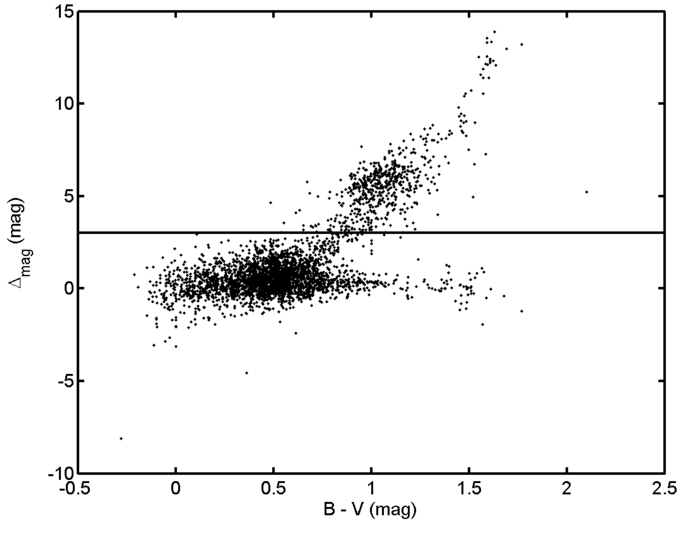

Fig. 6.8: Demonstration of how we define 'giants'. The definition is obviously arbitrary, and just serves as a classification issue. The solid line at $\Delta_{\mathrm{mag}} = 3$ marks where, based on the full sample, we draw a distinction between 'normal' (quasi-main-sequence) stars and giants.

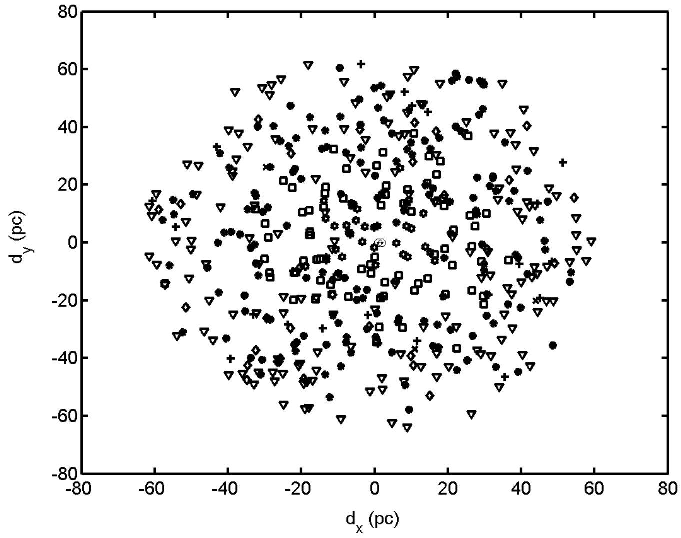

Fig. 6.9: The distribution of the final sample of stars, projected on the plane of the celestial equator. Since all the stars have a declination of less than ±5 deg, the plot gives a relevant view of their actual spatial distribution. Note, however, that the parameter space is larger at larger distances. Thus the reason that e.g. A-stars do not occur within a certain radius is not that they are de-selected there (at least not primarily), but that the parameter space is only wide enough outside of that radius to allow for a significant number of A-stars to be present. The outer radii are however set by selection – e.g., a K-star at 50 pc is generally not bright enough that an Earth-like planet can be detected in a sufficiently short time. For easier recognition of different classes of stars in this and other figures dealing with this sample, we use the following symbolics: B-stars are marked with 'x' marks, A-stars with diamonds, F-stars with triangles, G-stars with asterisks, K-stars with boxes, M-stars with hexagrams, and giants with '+' marks.

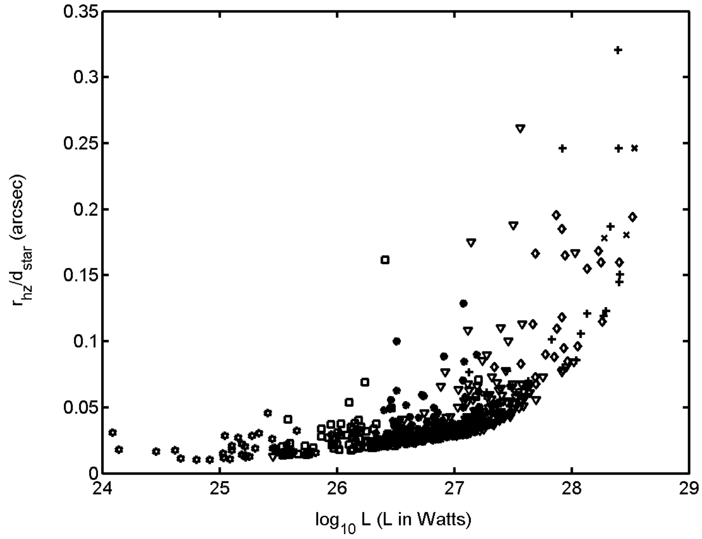

Fig. 6.10: Angular radius for the center of the habitable zone versus logarithmic luminosity. There is a sharp increase of angular scale for the very bright stars. Since the angular scale for the habitable zone is roughly proportional to the angular distance between planets near the habitable zone, less spatial resolution is required for those cases (see the text for discussion). For easier recognition of different classes of stars in this and other figures dealing with this sample, we use the following symbolics: B-stars are marked with 'x' marks, A-stars with diamonds, F-stars with triangles, G-stars with asterisks, K-stars with boxes, M-stars with hexagrams, and giants with '+' marks.

be sufficient for such an Earth-size planet. However, the contrast achieved by the occulter drops extremely fast with decreasing wavelength (see Sect. 6.4). Thus even in the worst case of our sample, where $r_{\rm hz,in} = 4.7$ AU, a sufficient contrast is still achievable for about 32 % of the wavelength range, thus by applying a corresponding penalty factor of 3.1 to the integration time (to make up for the lost photons), we get $t_{\rm hz} = 4.0$ hours for that case, i.e. not sufficient by our initial selection criterion, but still detectable by 5σ. Note that not using the longest wavelengths for the faintest planets around the intrinsically brightest stars leads to a decreased ability to resolve those particular planets from each other, for AO-related reasons (see Sect. 6.4). However, the intrinsically brightest stars also have the largest angular scales of their habitable zones (see Fig. 6.10), thus the requirements on spatial resolution is also less strict for those systems.

It may be argued that the most massive stars in this example sample (the A-stars and the few B-stars) are inappropriate targets, due to their inhospitable environments and short lifetimes that plausibly make the existance of planets in the habitable zone irrelevant from an astrobiological point of view. However, we would argue that a survey such as the one presented here should include a high-mass sample. This is mainly due to the reason that planets around massive stars are severely difficult to detect by any other means of observation. A survey like this one presents an excellent opportunity to study for the first time the presence, distribution and properties of planets as a function of stellar mass, for a wide range of masses. For the case of giants, an interesting range is covered. It has been suggested (see e.g. Lopez et al.,

2005) that the red giant phase for a roughly solar-mass star lasts long enough for a secondary genesis to occur, such that e.g. in an exact equivalent to the solar system in a red giant phase, life could occur on the Jupiter equivalent's moons. In our example survey, not only could such a Jupiter be detected (but obviously not its moons), but indeed we would be sensitive down to an Earth-sized planet in the secondary habitable zone, should it exist there.

For known binary systems, we de-select all binaries with inappropriate orbits, and keep the remaining ones in the sample. An orbit is deemed inappropriate if it has a separation of $\rho_{\rm low} = 10$ mas to $\rho_{\rm high} = 10$ arcsec for equal-brightness binaries. The upper limit is based on the following reasoning: we assume that we are completely seeing-limited, and that the seeing is 1.2 as (which is far worse than average for the best telescope sites). We require that the flux from the non-occulted component should be 10^{-10} of the flux from the occulted component, at the position of a given planet. If the binary components are equally bright, this is fulfilled at an angular distance of 6.56 arcsec from the non-occulted component, for a Gaussian PSF with a FWHM of 1.2 arcsec. Since we want to search an area of about 3 arcsec around the occulted component, it follows that we need a binary separation of about $\rho_{\rm high} = 10$ arcsec or larger to fulfill our requirements. If the non-occulted component is fainter than the occulted one, a smaller separation is acceptable, whereas if the opposite is true, a larger separation is required (note that in general, only the primary component is interesting). In multiple systems, the requirement naturally has to apply to all non-occulted components. For the lower limit of $\rho_{\rm low} = 10$ mas, we simply wish to ensure that both components are well within the IWA of about 15.5 mas. The binary separations were determined from the CCDM catalog (Dommanget & Nys, 2002) or, when not available there, from the US Naval speckle interferometry surveys (e.g. Douglass et al., 2000 and Mason et al., 2002). If no separation could be found at all, the binary was de-selected for being on the safe side.

Not all binaries are known, and so it is safe to say that there are most likely binaries with inappropriate separations left in our sample. It is interesting to make a rough estimation of how many such sources there are. In order to do this, we first adopt a binary fraction of 57 % as given in Duquennoy & Mayor (1991, henceforth DM91). Indeed, DM91 estimate a larger fraction when including brown dwarfs. However, as is noted in Lada (2006), the number of brown dwarfs in multiple systems are less than expected by DM91. Lada (2006) concludes that 57 % is probably correct for the types of stars used in DM91 (late F, early G), but also notes that the binary fraction is dependent on the primary mass (higher mass gives higher fraction, lower mass gives lower fraction). Since our average sample is roughly the same as in DM91, we simply adopt 57 % for this rough estimation. To estimate the fraction of inappropriate binaries, we assume that the average system mass is $(1+q)M_{\rm sun}$, where $q = 0.23$ is the average secondary-to-primary mass fraction. We also adopt the period distribution given in DM 91:

$$f(P_{\rm lg}) = Cst\exp\left(\frac{-(P_{\rm lg}-\bar{P}_{\rm lg})^2}{2\sigma^2_{P_{\rm lg}}}\right) \tag{6.14}$$

where $\bar{P}_{\rm lg} = 4.8$, $\sigma_{P_{\rm lg}} = 2.3$, and $P_{\rm lg} = \log_{10} P$ where P is the period in days. Using the average distance of the stars in the sample, $\bar{d}_{\rm star} \approx 32$ pc, we now translate our acceptance limits in angular separation into limits on semi-major axes, $s_{\rm bin,low} = \bar{d}_{\rm star}\rho_{\rm low}/\sqrt{2}$, and

$s_{\mathrm{bin,high}} = \bar{d}_{\mathrm{star}}\rho_{\mathrm{high}}/\sqrt{2}$. The factor $\sqrt{2}$ is introduced to take into account the fact that the systems are generally closer to edge-on than face-on. Since $q = 0.23$, binaries are generally not of equal brightness, but differ by several magnitudes. For this reason, we have adjusted ρ_{high} to 9 arcsec here. Translating semi-major axes into periods with Kepler's third law, $P = (4\pi^2 s_{\mathrm{bin}}^3/GM_{\mathrm{sun}}(1+q))^{1/2}$ and taking the logarithm, we get $P_{\mathrm{lg,low}} = 1.55$ and $P_{\mathrm{lg,high}} = 5.98$. The integral between these limits over the full integral of the period distribution function gives a fraction of 62 %. Given that 57 % of all systems are binaries, and about 62 % of those have inappropriate separations, it follows that 35 % of all systems are inappropriate for our purposes. For our example survey of 486 stars (before de-selecting any binaries at all), this corresponds to about 170 stars. Since 79 binaries with such separations are already known and have been removed, this leaves about 91 binaries that should ideally be removed in addition. Note, however, that the estimation is generous as it assumes bad seeing conditions compared to what is achieved on average at the best sites. In any case, it would be valuable to make dedicated binary searches around final sample candidates in order to remove as many troublesome systems as possible.

A final note on the target sample concerns stars with known planetary candidates from radial velocity surveys. Cross-checking with available lists (Schneider, 2008 and Butler et al., 2006a) shows that there are (as of mid-2006) 21 planetary candidates in 18 systems within -5 to 5 deg declination. Of these, 10 planets are outside of the IWA of CESO. 6 of the systems with such planets (HIP 14954, HIP 24205, HIP 27253, HIP 52409, HIP 64457 and HIP 113421) have $t_{\mathrm{hz}} < 2.0$ hours, and are thus already included in our example list. The others are of course also highly interesting targets that are worth considering including in a final list.

6.8 Why not L2?

The distance to the occulter from Earth in our setup is on the same order as the distance to the L2 dynamical equilibrium point. So why not place the occulter there? The reason for this is that in L2, the occulter 'sees' the Earth and sun in about the same direction. Thus when the occulter is face-on (or close to face-on) with respect to the Earth, as it has to be during observations, it is also face-on with respect to the sun. Thus sunlight will be scattered by the surface of the occulter towards Earth. The flux is approximately given by:

$$f_{\mathrm{scat}} = a_{\mathrm{occ}} f_{\mathrm{sun}} \left(\frac{R_{\mathrm{sun}} r}{ds} \right)^2 \tag{6.15}$$

where f_{sun} is the flux of the sun between 465 and 930 nm, and a_{occ} is the albedo of the occulter. We can make the surface as black as possible to minimize scattered light. However, even if we use the darkest materials presently available with albedo in the range of 10^{-3}, we get $f_{\mathrm{scat}} \approx 1 * 10^{-12}$ erg/s/cm^2, which is still a factor $2 * 10^5$ larger than the $\sim 5 * 10^{-18}$ erg/s/cm^2 we would need to easily discern the faintest objects we're aiming for. Note that in our proposed geometrical setup, no light is scattered from the sun, and the biggest source of scatter is instead light scattered from the sun against the Earth, then against the occulter back to the Earth. This adds about a factor $a_{\mathrm{E}}\frac{1}{4}(\frac{R_{\mathrm{E}}}{s})^2 \approx 1.4 * 10^{-6}$, such that the scattered light can be suppressed below the required limit. Going back to the L2 case, an alternative attempt to solve the scattered light issue, rather than trying to 'eat up' as much of the incoming radiation, would be to tilt the occulter somewhat with respect to the face-on plane towards the sun, and make the occulter surface flat enough such that the radiation is directed away from Earth through specular reflection. This would however introduce constraints on the occulter surface material – a membrane surface would hardly be sufficient to achieve this – which may introduce complications such as increased occulter mass etc. These problems are certainly worth considering to solve, since there is a lot to gain in an L2 orbit – ΔV_{oc} becomes significantly smaller, and the occulter is always at midnight, leading to longer possible integration times per visit regardless of the time of year. Still, since the Earth-leading (or Earth-trailing) orbit has a known, self-consistent solution space, we tentatively prefer that option.

6.9 Discussion

Planets plausibly constitute one of the most common types of compact objects in the universe – and certainly, the most important class of objects for astrobiology, due to their close association with life as we know it. Yet, it is also one of the astronomical objects we know the very least about, in a quantitative sense. This is obviously due to the fact that they are notoriously difficult to detect, largely dominated as they are by the parent star in terms of both mass and brightness. Dedicated missions must be deployed to acquire a decent knowledge base about these objects. Radial velocity, astrometry, transits, gravitational microlensing and direct imaging surveys in different wavelength bands all have potential for contributing with various aspects in this regard.

The concept we have presented here forms its own niche among planetary surveys as a potentially very low-cost mission with the ability to directly image Earth-size planets in the habitable zone, as well as a multitude of other kinds of planets, around stars with a wide range properties. Using only presently available technology, with a relatively low-tech component sent into space, and with ground-based observing facilities (which are orders of magnitude cheaper than space-based counterparts for the same capacity), it quite possibly constitutes the cheapest possible way to detect Earth equivalents through direct imaging.

CESO offers the possibility to perform a quite bias-free survey for extrasolar planets with respect to stellar mass, age, metallicity, rotation and so on. It therefore makes it possible to draw profound statistical conclusions of extrasolar planet presence and distribution as a function of stellar parameters for both terrestrial and giant planets.

The survey examples we have given here, with 2 or possibly 3 visits per source, are not sufficient to give complete orbits of the objects observed. Also, the spectral resolution that can be reached at a sufficient accuracy obviously depends on the brightness of the object, such that the faintest detectable objects can only yield very low-resolution spectra during the limited time of observation. Aside from the fact that follow-up observations could be made with any directable planet-finding facility that may eventually be launched, we note that CESO also offers an interesting option in this regard. Once the occulter is out of fuel and all scientific data have been collected and analyzed, a sample of the, say, 100 most interesting systems for follow-up are chosen. Another occulter, similar or identical to the previous one, is then launched, and each of the stars is observed an additional ~ 4 times (alternatively, two occulters could be launched of which one in Earth-leading and one in Earth-trailing orbit, for ~ 8 additional visits with a denser spacing). The orbits would then be much more well-defined. This is useful not only for determining the orbits in themselves, but also, the data could be applied to dynamical measurements of the system such that only a fit for the mass needs to be applied. This would yield much more stringent masses or mass limits than would otherwise be the case, when a full set of unknown Keplerian parameters must be fitted. Also, the spectra of each object at each visit could be averaged with each other to increase the SNR. In addition, by the time that the second generation occulters would be launched, it is plausible that the next-generation ground-based telescopes with diameters of about 20-50 m would be in operation. Thus, a much higher SNR could be provided for each visit. In this manner, CESO could act as a science driver for ELT:s on the ground, since the problem of detecting fainter objects and getting larger spectral resolutions with CESO is largely a case of collecting as many photons as possible – a case in which bigger is always better.

For practical reasons, it is interesting to keep the occulter as small as possible. We will therefore perform a short discussion about whether it is possible to decrease the size without compromising the science case. There are two ways of decreasing the physical size of the occulter while maintaining $R = 10^{-10}$. One is, as has already been mentioned, to decrease the longest wavelength at which $R = 10^{-10}$ is fulfilled. There are however several problems with this approach – the wavelength range decreases, and the AO performance decreases – and the gain in terms of occulter size is very modest for any reasonable choice of maximal wavelength. A more interesting approach is to decrease the observer-occulter separation s. As an example, we will consider the decrease of s by a factor 4 such that $s = 0.4 * 10^9$ m. For constant R, n and λ, it is the case that $r \sim s^{1/2}$. Hence, $r \approx 30$ m in this example. There are several disadvantages with this setup, but also many advantages: IWA increases by a factor of 2, but $t_{\mathrm{hz}} < 2$ hours can still be maintained for about 200 targets. The necessary instability corrections increase by about a factor 10, but the target-to-target motion decreases by a factor 4, hence by setting a smaller t_{diff}, the increase in total ΔV for a given sample size can be kept quite modest. The attainable solar power decreases by a factor 4, which is not a problem in the case of target-to target motion or orbit corrections, but for shadow control, the angle ϕ would have to be about 4 times larger, leading to a significant extension along one dimension of the occulter, unless a less power-requiring propulsion system is used. It would not be practical to use the occulter in combination with telescopes at latitudes of, say, 30 degrees, due to the very large ΔV_{sc}. On the other hand, with a telescope at around 75 degrees latitude, all targets could be observed for a very long time during the winter, at a very modest requirement for ΔV_{sc} (see Fig. 6.1). If, e.g., the proposed construction of an ELT at Dome C in Antarctica (75 deg south) would become a reality, such a setup would be highly interesting indeed.

An alternative interesting option when setting s would be to use an air-based telescope – i.e., on an airplane, like the SOFIA project which is currently under development. By adapting the speed and latitude of the airplane, the occulter shadow can be matched rather independently of s. In particular, the projection effect of a ground-based telescope could potentially be strongly decreased, leading to a much smaller ΔV_{sc}. This is very valuable, as the shadow control is the most critical velocity correction from a power budget perspective (as mentioned, shadow control is the only phase during which the occulter can not be turned face-on towards the sun). The telescope would presumably have to be considerably smaller than, e.g., a VLT (SOFIA has a diameter of about 2.5 meters), but on the other hand, the integration time per target could be larger, since the aircraft could be flown on the nightside of Earth, and the projection effects for the occulter to correct for would be small.

6.10 Conclusions

In this paper, we have pursued a novel idea for detecting extrasolar planets down to Earth-size or lower by direct imaging. We have introduced the concept of combining a space-based occulter of similar design to the NWO (see Cash 2006) with the best available ground-based telescopes and instrumentation, in a particular geometrical setup which minimizes the propulsion requirements for the occulter. With this setup, a very strong science case can be maintained using just a few tonnes of fuel. As an example, it was demonstrated that about 200 systems can be observed between 2 and 3 times if the engineering requirements can be fulfilled, and for each case, it is possible to detect Earth equivalents (same radius and albedo as Earth) in the habitable zone within 2 hours of integration time. The concept is quite possibly the safest and cheapest possible way to image an extrasolar terrestrial planet altogether – the occulter is based on known technology, and the fact that the observation facilities are ground-based leads to a cost- and photon-efficiency per unit integration time that can not even be approached by space-based counterparts. It also means that they can be easily maintained and upgraded during the extent of the mission if necessary. In addition, the mission could be launched faster than any other mission with the capacity to image extrasolar Earths, since it is not dependent on any major technological advances, or launches of any other spacecrafts.

CESO forms its own niche within exoplanet research with its capacity to planets down to Earth-size or smaller in (as well as outside of) the habitable zone of stars with a wide range of masses and other properties. In this way, it complements other exoplanet survey missions, including other direct imaging concepts, for forming a strong knowledge basis of extrasolar planets. In a vital but underfunded research area, CESO offers the option of a low-cost, low-risk solution with an enormous potential scientific output.

Tab. 6.1: Appropriate preliminary CESO target list for observations from the ground.

HIP number	Dist. (pc)	$B - V$ (mag)	t_{hz} (h)
159	59.1	0.29	1.71
870	54.9	0.50	1.60
1663	21.4	0.36	1.29
2787	55.6	0.44	1.43
3086	45.8	0.63	1.04
3535	22.0	0.98	0.30
3540	41.2	0.53	0.77
3645	27.9	0.82	0.38
4747	40.3	0.54	0.74
4979	56.6	0.27	1.60
5141	45.7	0.38	0.99
5144	44.0	0.48	0.88
5315	46.4	0.84	1.00
5647	32.1	0.93	1.35
5833	43.8	0.42	0.89
5985	29.6	0.56	0.40
6130	27.6	0.78	0.55
6653	39.4	0.67	0.70
6679	51.1	0.44	1.21
6762	29.7	0.73	0.56
7357	36.6	0.53	0.61
7860	42.1	0.73	1.27
8051	11.2	1.52	0.39
8798	37.6	0.63	0.76
8833	58.4	0.92	1.61
9353	31.0	0.61	0.43
9576	48.4	0.66	1.06
9911	36.9	0.62	0.62
10279	10.3	1.43	0.21
10305	46.0	0.54	0.97
10416	22.8	1.05	0.54
10723	24.9	0.58	0.28
10818	39.2	0.74	1.58
11028	39.6	0.72	1.31
11218	53.8	0.51	1.32
12048	35.9	0.67	0.58
12158	24.3	0.94	0.40
12493	22.3	1.18	1.20
12862	51.2	0.31	1.29
13717	57.8	0.08	1.94
14445	14.7	1.35	0.28

Tab. 6.1: Continued.

15247	49.9	0.53	1.29
15442	24.6	0.65	0.27
15457	9.1	0.68	0.03
16852	13.7	0.57	0.08
17147	24.3	0.55	0.27
17183	44.8	0.95	0.97
17207	25.0	1.36	1.35
17695	16.2	1.51	1.50
17743	17.3	1.49	1.24
17801	52.6	0.77	1.31
17888	33.3	0.82	1.38
17895	54.9	0.58	1.37
17988	65.1	0.39	1.96
18261	45.1	0.63	1.81
18388	48.6	0.50	1.08
18512	15.7	1.11	0.15
18859	19.2	0.51	0.16
18993	34.6	0.50	0.54
19024	45.9	0.76	1.87
19070	62.3	0.75	1.76
19434	62.6	0.44	1.81
19788	33.3	0.94	1.40
19832	20.4	1.20	0.89
19925	40.3	0.66	1.38
20218	35.8	0.67	0.88
20373	62.0	0.57	1.75
21307	61.6	0.71	1.72
21383	37.8	0.63	1.16
21534	59.9	0.56	1.82
21537	62.6	0.57	1.97
21547	29.7	0.28	0.44
22175	32.1	0.67	0.69
22296	57.8	0.45	1.83
22319	47.5	0.84	1.04
22919	35.9	0.56	0.59
22940	39.2	0.83	1.51
23105	33.5	0.70	0.50
23200	26.6	1.39	1.67
23287	42.8	-0.05	1.18
23296	49.5	0.29	1.20
23941	25.0	0.45	0.28
24130	48.4	0.98	1.13
24162	38.4	0.46	0.68
24205	28.6	0.58	0.37
24336	46.8	0.63	1.69

Tab. 6.1: Continued.

24493	45.9	0.40	0.97
24817	60.7	0.41	1.70
24864	37.4	0.53	0.64
25282	52.8	0.96	1.34
25623	12.9	1.11	0.08
25878	5.6	1.47	0.02
25905	38.1	0.69	1.61
26081	16.8	1.57	1.33
26624	41.3	0.29	0.84
26762	51.3	0.31	1.29
26907	31.3	0.88	1.11
27118	50.5	0.32	1.25
27253	42.4	0.77	0.81
27435	15.5	0.63	0.11
27918	26.6	1.01	0.96
27980	46.7	0.62	1.44
28428	53.5	0.63	1.58
29573	61.8	0.99	1.84
29716	35.6	0.50	0.58
30030	49.7	0.58	1.90
30243	41.1	0.68	0.95
30419	39.3	0.21	0.81
30422	24.3	0.45	0.27
30513	48.5	0.50	1.08
30545	33.0	0.56	0.49
31083	27.9	0.71	0.35
31326	56.2	0.39	1.46
31480	61.2	0.57	1.92
32617	40.0	0.29	0.78
33382	32.1	0.69	0.47
34239	64.1	0.51	1.88
34341	26.7	1.27	1.89
35173	34.1	1.01	1.83
35209	41.1	0.60	0.83
36071	35.6	0.56	0.57
36310	46.8	0.77	1.66
36338	12.5	1.48	0.96
36723	42.6	0.32	0.89
36976	35.4	0.56	0.57
36985	14.3	1.45	0.34
37088	62.0	0.44	1.78
37288	14.8	1.37	0.36
37349	14.1	0.89	0.09
37645	52.7	0.58	1.26
38138	61.5	0.35	1.96

Tab. 6.1: Continued.

39017	61.7	0.29	1.86
40501	9.1	1.51	0.11
40613	48.8	0.58	1.51
40774	23.3	0.90	0.51
40858	40.8	0.60	0.75
41214	64.6	0.46	1.93
41307	38.3	-0.01	0.91
41375	53.1	0.21	1.47
41573	44.9	0.52	0.96
42030	51.3	0.61	1.46
42074	21.7	0.79	0.21
42634	33.5	0.76	0.51
43297	29.8	0.68	0.42
43790	20.0	1.37	0.89
44379	55.6	0.44	1.65
44584	47.9	0.48	1.92
44953	38.6	0.76	1.75
45336	39.4	-0.06	1.15
45621	32.7	0.86	0.58
45737	29.3	0.86	0.65
46509	17.0	0.41	0.13
46543	54.3	0.83	1.37
46655	9.6	1.58	0.51
46690	47.5	0.51	1.03
48025	47.4	0.59	1.39
48273	45.9	0.47	0.97
48411	20.9	1.23	0.58
48477	15.6	1.50	0.52
48768	45.1	0.47	0.94
49329	54.9	0.39	1.39
49544	22.3	1.34	1.46
49694	57.9	0.36	1.60
49756	37.0	0.64	0.72
49969	12.3	1.56	0.31
49986	7.8	1.48	0.04
50139	36.1	0.60	0.94
51317	7.2	1.50	0.04
51386	31.5	0.56	0.45
51784	35.2	0.50	0.56
52316	34.3	0.88	0.54
52409	32.3	0.69	0.47
52574	51.3	0.49	1.20
52610	52.3	0.72	1.77
52705	36.5	0.68	1.01
53532	61.8	0.42	1.77

Tab. 6.1: Continued.

54027	54.6	0.26	1.48
54155	24.6	0.77	0.28
54541	30.5	0.77	0.50
54810	17.9	1.17	0.36
54857	62.7	0.39	1.82
55084	59.9	0.21	1.88
55288	55.6	0.57	1.40
55791	61.4	0.34	1.80
55846	17.6	0.77	0.14
55848	17.9	1.00	0.15
55982	52.0	0.50	1.24
56445	26.5	0.48	0.32
56647	54.6	0.98	1.43
56738	39.3	0.56	0.87
56955	41.2	0.76	1.77
57083	36.8	0.61	0.63
57370	28.9	0.83	0.65
57629	34.1	0.51	0.53
57757	10.9	0.51	0.05
58268	49.9	0.48	1.14
58368	54.3	0.41	1.36
58558	42.8	0.75	1.49
58949	32.7	0.75	0.81
59422	50.2	0.45	1.17
59984	61.7	0.36	1.82
60942	59.8	0.40	1.66
61173	56.6	0.64	1.54
61578	46.5	0.48	0.99
62016	30.5	0.79	0.70
62039	46.4	0.67	1.47
62607	33.2	0.68	0.99
62687	10.7	1.40	0.06
63070	58.9	0.79	1.59
63099	52.1	0.47	1.73
63235	59.0	0.45	1.61
64457	20.4	0.93	0.19
64984	33.8	0.67	0.68
65121	30.4	0.93	0.97
65352	16.0	0.78	0.11
65355	16.7	0.86	0.13
65708	45.8	0.65	1.00
66200	56.2	0.02	1.89
66222	20.5	1.38	0.90
66249	22.4	0.11	0.28
66367	49.3	0.53	1.11

Tab. 6.1: Continued.

66675	14.5	1.37	0.33
66840	23.7	1.28	1.38
66886	24.2	1.18	1.10
67412	39.8	0.73	1.62
68469	10.1	1.46	0.15
68619	60.8	0.59	1.94
68707	62.8	0.40	1.83
69340	45.9	0.47	0.97
69414	22.2	0.73	0.22
69493	55.7	0.48	1.42
70319	17.5	0.63	0.14
70741	31.1	0.53	1.02
70782	40.5	0.54	0.75
70906	55.7	0.40	1.43
72220	39.4	-0.00	0.96
72223	39.2	0.56	0.70
72312	19.6	0.89	0.21
72339	29.7	0.78	0.66
72703	38.9	0.65	1.68
73165	27.9	0.31	0.38
73309	34.8	0.50	0.55
73620	56.2	1.02	1.55
74190	14.4	1.51	1.06
74689	49.5	0.18	1.28
74702	15.5	0.83	0.11
74948	52.2	0.55	1.24
75101	36.9	1.06	0.67
75201	18.8	1.31	0.66
75266	25.4	0.99	0.51
75342	54.9	0.26	1.53
75521	57.9	0.42	1.55
75761	37.4	0.24	0.71
76031	50.8	0.64	1.20
76291	58.9	0.28	1.73
76635	55.1	0.54	1.60
76963	55.2	0.60	1.42
77094	59.1	0.41	1.62
77335	48.2	0.51	1.06
77408	21.3	0.80	0.20
77464	49.1	0.12	1.36
77516	47.7	-0.03	1.47
77622	21.5	0.14	0.25
77749	41.5	0.67	1.19
77810	40.5	0.62	1.61
77816	52.7	0.47	1.40

Tab. 6.1: Continued.

78399	43.4	0.64	1.79
78513	55.1	0.39	1.45
78742	51.9	0.45	1.25
79730	46.5	0.52	0.99
79781	47.6	0.32	1.08
80179	27.3	0.33	0.35
80218	27.6	0.71	0.34
80398	61.3	0.43	1.74
80837	41.0	0.54	0.77
81062	52.5	0.53	1.26
81279	51.7	0.52	1.22
81300	9.7	0.82	0.04
81421	37.6	0.76	0.98
81681	29.5	0.63	0.39
81734	50.7	0.33	1.23
82142	60.6	0.35	1.75
82405	59.8	0.40	1.65
82588	16.9	0.74	0.13
82688	47.6	0.59	1.54
83601	20.3	0.57	0.18
83770	33.6	0.73	0.64
83863	54.9	0.62	1.37
83906	35.3	0.69	0.56
84082	43.8	0.56	0.87
84696	36.5	0.53	0.61
84905	38.6	0.57	0.68
85042	19.4	0.68	0.17
85295	7.7	1.35	0.03
85307	61.7	0.45	1.76
86400	10.7	0.95	0.05
86742	25.1	1.16	0.32
86765	29.9	0.67	0.52
87108	29.0	0.04	0.50
87678	51.4	0.51	1.21
87937	1.8	1.57	0.00
88175	23.1	0.39	0.25
88324	32.6	0.74	0.51
88481	34.4	0.79	0.95
88574	7.7	1.50	0.04
88622	24.3	0.61	0.27
88684	34.9	0.96	0.58
88961	29.1	1.02	1.25
89601	62.5	0.31	1.92
89825	19.3	1.35	0.83
89962	18.9	0.94	0.17

Tab. 6.1: Continued.

90656	18.7	1.07	0.22
90810	64.5	0.38	1.99
91281	58.5	0.56	1.56
91337	48.7	0.37	1.13
91645	39.3	0.50	0.70
92200	14.1	1.29	0.20
92569	28.2	0.70	0.40
92946	40.4	0.16	0.89
92951	43.7	0.20	1.00
92984	27.0	0.58	0.33
93195	30.4	0.82	0.96
93580	55.1	0.18	1.59
93743	44.8	0.35	0.95
93805	38.3	-0.09	1.32
95055	49.4	0.43	1.13
95501	15.3	0.31	0.11
96285	14.4	1.39	0.25
96351	42.0	0.41	0.81
96392	65.0	0.50	1.93
96556	32.1	0.42	0.47
96834	47.4	0.53	1.22
96948	40.3	0.66	0.93
97255	30.2	0.61	0.41
97384	49.4	0.61	1.11
98698	13.1	1.12	0.08
98878	33.1	0.70	0.66
98964	43.0	0.77	1.86
99100	48.0	0.73	1.93
99171	47.8	1.02	1.12
99711	19.8	0.93	0.20
100072	36.6	0.56	0.61
100895	46.5	0.52	1.12
100896	48.3	0.51	1.06
101022	31.9	0.54	0.46
101059	36.8	0.51	0.62
101101	58.5	1.16	1.76
101136	54.2	0.55	1.68
101620	50.5	0.48	1.24
101852	41.8	0.59	1.15
102393	59.3	0.65	1.85
103571	60.2	0.45	1.68
103682	26.4	0.63	0.31
103931	48.3	0.42	1.08
103987	56.0	0.54	1.44
105066	42.8	0.73	1.30

Tab. 6.1: Continued.

105152	19.2	0.99	0.26
105483	39.6	0.76	1.06
105864	47.8	0.48	1.04
106601	60.2	0.57	1.65
106825	36.7	0.84	1.58
107895	35.1	0.84	1.42
107941	31.2	0.88	0.77
108473	42.2	0.57	0.81
108506	36.0	0.97	0.62
108525	35.5	0.75	1.26
108761	45.7	0.68	1.66
108782	10.3	1.45	0.09
109144	50.5	0.53	1.17
109388	8.7	1.53	0.12
110091	41.4	0.44	0.79
110395	48.3	-0.05	1.73
110753	51.0	0.46	1.21
110882	49.0	1.03	1.18
111571	17.5	1.41	0.67
111888	22.6	0.93	0.49
112229	42.2	0.51	0.86
113355	44.6	0.54	1.29
113699	43.0	0.58	0.84
113718	16.9	0.94	0.13
113834	54.9	0.57	1.97
113896	30.7	0.58	0.43
113980	45.5	0.47	0.96
114233	15.6	1.49	0.88
114322	29.9	1.01	0.96
114971	40.1	0.91	0.75
115220	47.7	0.52	1.04
115381	37.1	0.85	1.52
115738	49.7	0.03	1.48
115951	39.4	0.62	0.70
115953	48.9	1.12	1.23
116069	53.6	0.44	1.33
116106	26.2	0.53	0.31
116317	13.9	1.45	1.07
116384	19.3	1.32	0.78
116402	58.1	0.41	1.56
116410	38.7	0.72	1.46
116495	30.9	0.44	0.44
116928	30.8	0.20	0.49
117367	46.6	0.62	1.49
117445	55.2	0.46	1.41

Tab. 6.1: Continued.

117463	26.6	0.92	0.68
117473	5.9	1.46	0.02
117953	29.3	0.75	0.43
G99-49	5.2	1.68	0.07
GJ285	5.9	1.61	0.09
GJ447	3.3	1.77	0.02

Chapter 7

A double-differential scheme for spectroscopy of transiting planets from the ground

Unpublished

7.1 Introduction

Detections of transiting extrasolar planets have allowed for the first time studies of the physics of such objects. A detection of a transit in combination with radial velocity data gives the density of the planet, and can therefore give clues about its interior structure (see e.g. Seager et al. 2007). Furthermore, the atmospheric properties can be constrained for these types of planets. Transmission spectroscopy during the transit of HD 209458 has led to the detection of compounds such as NaI and HI (see Charbonneau et al. 2002; Vidal-Madjar et al. 2003). Monitoring of the infrared excess from HD 189733 over half an orbit allowed for the determination of a one-dimensional temperature map of its surface (see Knutson et al. 2007). In addition, differential spectroscopy during (and around) the secondary eclipses of HD 209458 and HD 189733 has been used to extract low-SNR spectra of the transiting planets (Richardson 2007; Grillmair et al. 2007; Swain et al. 2008).

Most of the progress so far in this area has been made with space-based telescopes, in particular the Spitzer space telescope. From the ground, sensitivity tends to be limited by systematics, dominated by variations in the atmospheric transmission over the duration of an eclipse. However, if these systematics can be overcome, ground-based observations would be preferable due to the larger apertures, better instruments, and in general higher cost efficiency. The issue is particularly interesting in light of the fact that Spitzer has a very short remaining duration of its full potential, as it will run out of coolant shortly, thus greatly limiting its operability (only imaging observations in the near infrared with IRAC can continue with good performance).

In this chapter, we discuss a method with the potential to overcome the difficulties of a varying atmosphere during observations of a secondary eclipse, thus opening up the possibility to study the thermal spectral properties of transiting exoplanets. In the following, we discuss the motivation and application of this method, and show results from a test performed to confirm its validity, executed with SINFONI at the VLT.

7.2 Spectral- and time-differential spectroscopy

As mentioned above, exoplanet spectroscopy during secondary eclipses is limited from the ground by the systematic effects of the atmosphere. As we have also seen over and over in this thesis, a generally efficient methodology to reduce the impact of systematic noise is the use of differential methods, where some feature which is common-mode for the dominant systematic but not for the planet (or vice versa) is used for the purpose of canceling out the contribution of the dominant systematic whilst retaining the planetary signal. Usage of the secondary eclipse is by itself a differential (or potentially differential) method which takes advantage of the fact that the observed stellar flux is constant over time during an eclipse, but the planetary flux is not. In short, it is a time-differential method.

However, the mean atmospheric transmission varies with time, and the transmission and variation of the transmission is different for different wavelengths, and neither of these effects is accounted for with such a method. What can be used instead, in combination with the time differencing, is spectral differencing. Over sufficiently small wavelength ranges, atmospheric systematics are almost common-mode, but the spectrum of the planet may vary over the same range. Hence, by differencing spectral channels with an appropriate algorithm, atmospheric effects are mostly canceled out, whereas the derivative of the planet spectrum is conserved over small scales. We will discuss the issue of appropriate algorithms in Sect. 7.4. Sharp features are most easily detected with this method, such as the onset of methane absorption at 1.6 μm expected for sufficiently cool atmospheres.

7.3 Observations

For testing the method we used SINFONI AO data of HD 189733 that was meant to be taken before, during, and after primary and secondary eclipse, spanning 4 hours for each of the two events. While one set of data covered the primary eclipse, the other set of data was incorrectly timed and covered nothing with respect to the eclipse events (i.e., was scientifically useless, at least for the purpose of determining planetary properties). Here we will only discuss the data set covering the primary eclipse, which was taken on Jul 30, 2006 at 03:00-07:00 UT.

The atmospheric conditions during observations were poor, with a mean seeing of 1.5” according to the atmospheric site monitor, leading naturally to a poor achieved mean Strehl ratio of 7 % according to the measurements given by the adaptive optics system itself (the observational windows for transiting planets are few enough that the execution of the observations can not be adapted to the weather, and hence the conditions are purely a matter of chance). The airmass was chosen to be about as good as it gets on Paranal for this northern sky target, and varied between 1.47 and 2.20 during the observations.

The SINFONI data were taken in the 'H+K' setting, giving a spectral coverage from about 1.4 to 2.5 μm at a spectral resolution of about $R = 1500$. The smallest pixel scale of 12.5×25 mas was used, giving a field of view of 0.8" × 0.8". A dithering scheme was used where one sky frame was taken for about every 12 object frames. In total, 46 object frames were taken, of which roughly half corresponded to the eclipse and ingress/egress, and the other half to the non-eclipse continuum.

7.4 Data reduction

For generating cubes from the raw data, the standard ESO data reduction pipeline was used, taking care also of the basic standard reduction steps such as flat fielding, bad pixel removal, distortion corrections etc. For extracting appropriate spectra, we used routines specifically designed for this purpose in IDL. The procedure was to select a circular aperture with a radius of 18 pixels, centered on the star. The centering was determined individually for each frame with Gaussian centroiding. This was done in order to account for the effect of differential atmospheric refraction, which otherwise moves the photocenter of the image as a function of wavelength. The flux inside the aperture was summed up for each wavelength, thus producing a spectrum individually for each time step. The flux as a function of wavelength and time was stored in a matrix for further analysis purposes.

One of the major problems with the final data was that due to the poor Strehl ratio, a significant fraction of the stellar flux ended up outside of the small FOV of SINFONI. Additionally, the fraction of flux lost from each frame was dependent on the seeing and Strehl ratio achieved for that particular frame, simply due to the different fractions of light concentrated in the halo, and the different widths of the halo. Since the measured Strehl ratio is a very approximate number, this effect turned out to be very difficult to model, and our attempt to account for this effect by correcting for a model PSF with given values of seeing and Strehl turned out to only make the quality worse, hence we did not include such a correction.

Digital observables were produced for the purpose of spectral differencing in the following way: We denote the flux in a given spectral channel i as f_i. The width of the channel is adaptive (can consist of any number of adjacent wavelength samples depending on the scientific purpose). The flux in the nearest adjacent spectral channel j is denoted f_j. The differential observable can be based on the difference $f_i - f_j$ or the quotient f_i/f_j. Which one is most appropriate must be chosen on a case-to-case basis, and among other things depends on whether the dominating systematic noise is additive or multiplicative. In our case, tests for the output contrast showed that the best observable among those tested was $(f_i - f_j)/(f_i + f_j)$, where the normalizer $f_i + f_j$ corrects for fluctuations in mean transmission, something that is automatically corrected for also by f_i/f_j.

7.5 Results and discussion

A lightcurve for the differential feature in- and and outside of methane absorption at 1.6 μm is shown in Fig. 7.1. The channel width in this case was 30 spectral slices (where each

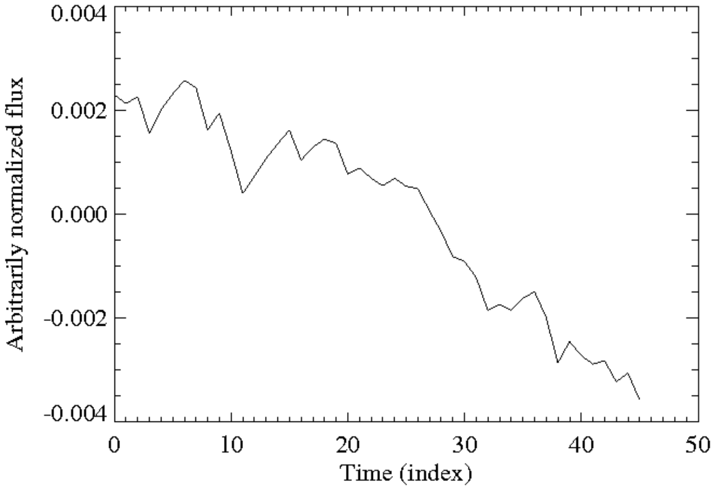

Fig. 7.1: Lightcurve for the CH_4 differential feature for 15 Å channels. Systematics are seen to dominate the data, which are anti-correlated with the airmass and correlated with the Strehl ratio.

slice corresponds to a frequency range of 5 Å). The Strehl and airmass for each of the time steps are shown in Fig. 7.2. There is a clear correlation with both Strehl ratio and airmass in the lightcurve. This means that the error is dominated by systematic noise originating from variations in these quantities. The airmass impact is smooth, and could in principle be modeled out using, e.g., a parabolic fit. However, such a procedure is risky for this data set, because the number of time samples is small, and any transit occurring in such a case could thus affect the fit. In particular, if the transit should occur near the beginning or end of observations due to uncertainties in the orbit, this would strongly bias the fit towards subtraction of the real event along with the airmass correction.

Since the systematic errors are due to chromatic effects, they decrease rapidly with decreasing channel width. This is seen clearly in the case where the channels are represented by a few or even single spectral slices (see Fig. 7.3). The systematic effects have strongly decreased in these cases, making the lightcurves dominated by mostly uncorrelated noise at some wavelengths. The relative impact of photon noise obviously increases as channel width decreases, but still, small channel widths in fact lead to the best overall contrasts (not accounting for corrections of the systematic trends). A whole double-differential (spectral- and time-differential) spectrum at a channel width of 3 slices is shown in Fig. 7.4, and the corresponding inverse standard deviations are shown in Fig. 7.5. It can be seen that a contrast of over 1:8000 can be reached in the very best cases, though more commonly 1:5000 is reached in the H-band, lower in the K-band. Lower contrasts naturally occur near the strong atmospheric absorption features where very few photons make it past in the first place, and differential systematic effects are larger.

While some features appear to stand out in the double-differential spectrum, individual checks of these features reveal them to be outliers, in that they do not display the type of temporal behaviour that would be expected to result from an eclipse (see Fig. 7.6).

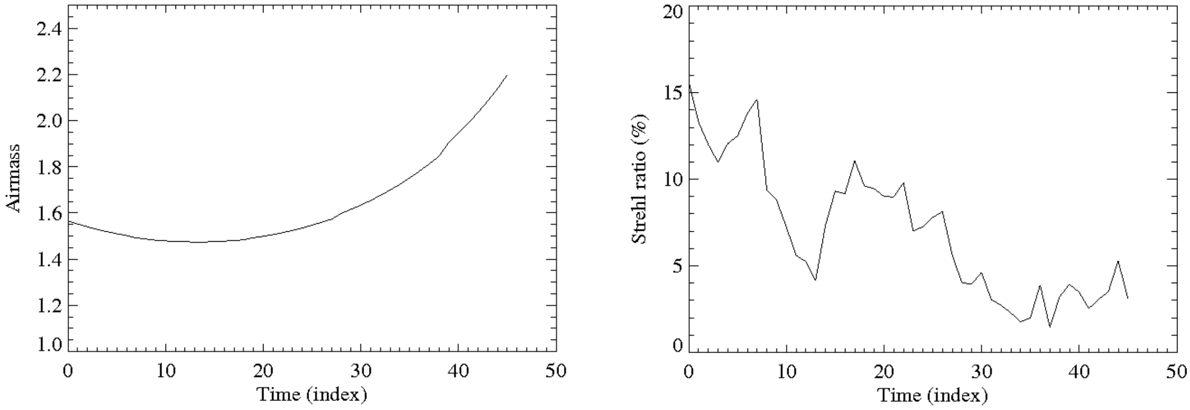

Fig. 7.2: Variations of observational conditions over the duration of the observations. Left: Airmass. Right: Strehl ratio.

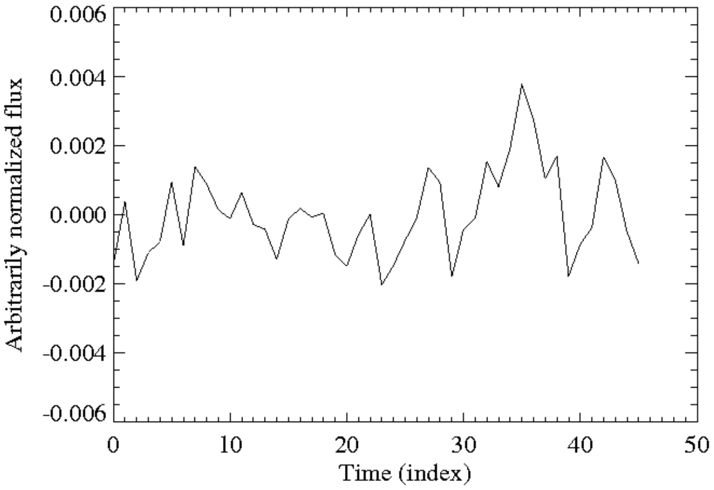

Fig. 7.3: Another lightcurve for the CH_4 differential feature, this time with the smallest possible channel width. The systematic influence on the data is much smaller for this case.

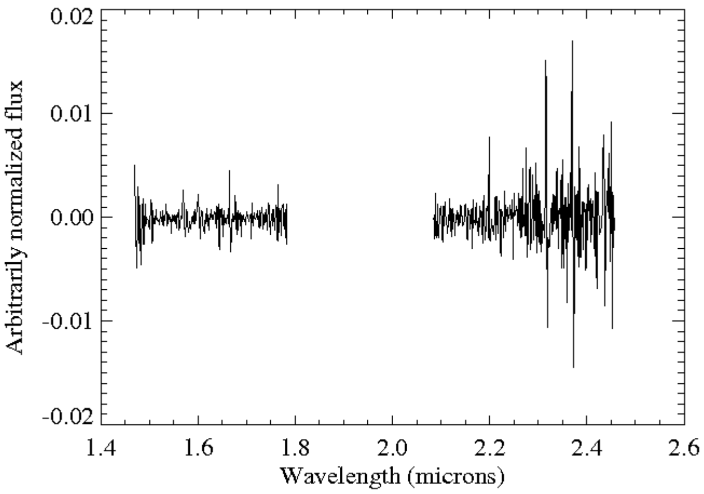

Fig. 7.4: Double-differential spectrum in H- and K-band. The range between the bands has been removed here, due to the large errors following from the poor transmission in that telluric absorption band.

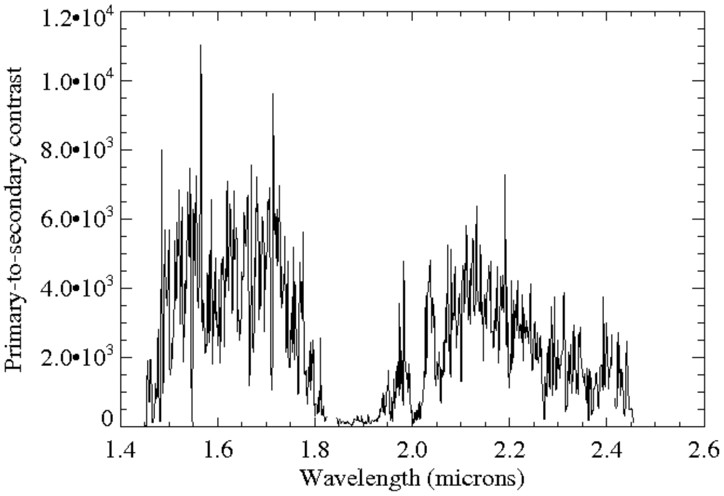

Fig. 7.5: Sensitivity for spectral features of the companion, in terms of primary-to-secondary contrast ratio.

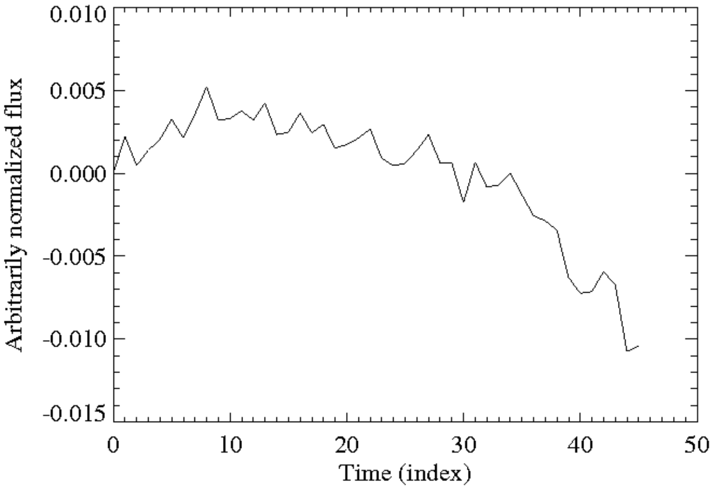

Fig. 7.6: Lightcurve for an apparent feature at 1.665 μm in the double-differential spectrum. It is clearly seen that the curve looks nothing like transit dip, as would be expected if the feature corresponded to a real planetary event. Hence, the point can be easily discarded as an outlier.

7.6 Conclusions

We have seen that by applying a double-differential scheme, factors that limit the achievable contrast due to systematic effects imposed by the atmosphere can be strongly mitigated. However, the method is limited to finding narrow features in the spectra, and could not be used to make any conclusions with regards to the continuum emission. The small field of view of SINFONI and a non-optimal observation procedure ultimately limits the performance. Usage of different instruments better suited for the observations with a larger field of view, better AO capacity, or better dynamic range could improve the results substantially. The residual systematic errors are chromatic, and decrease strongly with decreasing channel width. Hence, a higher spectral resolution could also improve the results, though two aspects must be considered in that regard: 1) the sensitivity limit increases with decreasing channel width, and 2) the sought-after features must be sharper the smaller the channel width, in order for anything to be gained in terms of performance relative to wider channel widths.

CHAPTER 8

SUMMARY AND OUTLOOK

In this thesis, I have examined various approaches for direct detection and characterization of substellar companions to stars. As we have seen, an important characteristic for planets and brown dwarfs is the mass, but this can be hard to determine. For instance, it is desirable for survey non-detections in direct imaging to translate the brightness detection limit into a mass detection limit, in order to constrain formation models. For this purpose it is necessary to know the mass-luminosity relationship, but this is poorly calibrated for young, low-mass objects. This problem was approached in this thesis by examining the object GQ Lup B, where it was shown how difficult it is to acquire the mass from the brightness of such an object without properly constrained theoretical models. Since the semi-major axis of the GQ Lup system is on the order of 100 AU, and the total mass is smaller than that of the sun, the dynamical mass of GQ Lup B will not be determinable in the foreseeable future. One object with excellent prospects for becoming a high-quality calibration point for the models in question is AB Dor C, but the age of the object needs to be well-constrained for this purpose. We used AB Dor Ba/Bb for constraining the age of the whole system, finding an age range of 50-100 Myr. The work lays the ground also for future work, which can constrain the age even well beyond this point, in turn putting very strong constraints on theoretical models. The age of course also feeds back into the age of the whole AB Dor moving group, since it is approximately coeval. In fact, even the degree of coevality can be stringently tested by monitoring other close binaries in the group in the same way. Such work has already been started, see e.g. Hormuth et al. (2007). The method of monitoring close young binaries astrometrically and photometrically in other co-moving associations furthermore has the potential of constraining relative (and, by extension, absolute) ages for the different groups, which is of high importance when judging the relative merit of potential targets for future high-contrast imaging surveys. Nearby young moving groups have been a prime source for selecting young targets in the past, and will certainly continue to be so in the future.

Systematic noise sources dominate in ground-based high-contrast imaging, and differential methods are necessary to mitigate these effects. If nothing else, the results on GQ Lup clearly demonstrate this. We have used various combinations of differential techniques, in particular SDI and ADI. In the case of NACO-SDI for ϵ Eri, this was shown to reach unprecedented brightness contrast of $\Delta H = 15$ mag at 1.5", thus setting an improved upper limit of the planetary companion ϵ Eri b. The SNR was shown to scale linearly with the Strehl ratio achieved by the AO system, and scaled surprisingly close to the $t^{1/2}$ limit for the integration time, implying that even better results may be reached by simply integrating longer. In comparison, the performance of SINFONI for SDI purposes was shown to be rather poor, reaching a significantly lower image contrast than NACO-SDI, and with a slower integration time development. The result underlines the importance of explicitly comparative tests for future instruments specialized for planet detection such as the differential imager versus integral field unit of SPHERE. In all, the high contrast reached already with the present-day instrumentation points to a bright future for exoplanet imaging with instruments such as SPHERE or GPI, despite the many null-results reached in large-scale surveys so far.

In the near-term future, particular focus should be placed on examining sample ranges that have so far not been covered in high-contrast surveys. This is particularly relevant for massive main-sequence stars, as both theory (e.g. Kennedy & Kenyon 2008) and observations (e.g. Johnson et al., 2007) imply that very massive planets should be more common in such systems. Under the assumption that planetary mass scales linearly with stellar mass, the brightness contrast between star and planet should be roughly independent of the stellar mass judged by the models of e.g. Baraffe et al. (1998, 2003), at ages around 100 Myr. Observations can be done at relatively long wavelengths (at around 3.5 μm), a concept proven useful in Kasper et al. (2007), or with NACO-SDI+, the new improved implementation of NACO-SDI. Additionally, similar high-contrast imaging instruments such as NICI at Gemini and HiCiao at Subaru will come online in the near future, which are excellently suited for this purpose.

Another way of solving the high-contrast problem in observations from the ground is to synchronize the telescope with a free-flying occulter in space. With such a setup, the zero-phase wavefront can be canceled out before it is distorted by the atmosphere, and a sufficient contrast to even detect Earth-equivalent planets can be reached. The concept is cheap (in relative terms) and has a high technological readiness, but more work should be done for the purpose of decreasing mass of the occulter – most favourably by decreasing its size, as this also improves the inner working angle.

Just like in the case of direct imaging searches for extrasolar planets, eclipse spectroscopy of such objects is also limited by systematics imposed by the atmosphere – variations in the atmospheric transmission during the extent of the observations causes a variation that dominates the photometric and spectroscopic dips that occur during secondary eclipse. Multiple differential methods again prove useful for mitigating such noise sources. By using spectral- and time-differential spectroscopy, we reach a planet-to-star contrast of one in several thousands with SINFONI across the whole H- and K-band spectral range. Much like for the case of SDI, the shortcomings of SINFONI ultimately limits the achievable contrast. Future work should be made with other instruments, such as NACO-SDI+, NICI, or CRIRES, with a different observing strategy to minimize systematic influences, in order to reach even deeper contrasts.

BIBLIOGRAPHY

[2004] Aime, C., & Soummer, R. 2004, ApJ 612, L85

[2005] Alibert, Y., Mordasini, C., Benz, W., & Winnisdoerffer, C. 2005, A&A 434, 343

[1997] Allard, F., Hauschildt, P., Alexander, D., Starrfield, S. 1997, ARA&A 35, 137

[2001] Allard, F., Hauschildt, P.H., Alexander, D.R., Tamanai, A., Scweitzer, A. 2001, ApJ 556, 357

[2007] Apai, D., Janson, M., Moro-Martin, A. et al. 2008, ApJ 672, 1196

[2006] Bacon, R., Bauer, S., Boehm, P. et al. 2006, SPIE 6269, 17

[1995] Baliunas, S.L., Donahue, R.A., Soon, W.H. et al. 1995, ApJ 438, 269

[1998] Baraffe, I., Chabrier, G., Allard, F., Hauschildt, P. 1998, A&A 337, 403

[2002] Baraffe, I., Chabrier, G., Allard, F., Hauschildt, P.H. 2002, A&A 382, 563

[2003] Baraffe, I., Chabrier, G., Barman, T.S., Allard, F., Hauschildt, P.H. 2003, A&A 402, 701

[2004] Barrado y Navascués, D., Stauffer, J.R., Jayawardhana, R., Cuillandre, J.-C. 2004, ApJ 610, 1064

[2005] Basri, G., Borucki, W.J., & Koch, D. 2005, New AR 49, 478

[2000] Bastian, T.S., Dulk, G.A. & Leblanc, Y. 2000, ApJ 545, 1058

[1979] Bastian, U., Mundt, R. 1979, A&AS 36, 57

[2006] Beaulieu, J.-P., Bennett, D.P., Fouque, P. et al. 2006, Nature, 439, 437

[2006] Beichman, C., Lawson, P., Lay, O. et al. 2006, SPIE 6268, 25

[2002] Benedict, F., McArthur, B., Forvelle, T. et al. 2002, ApJ 581, L115

[2006] Benedict, F., McArthur, B., Gatewood, G. et al. 2006, AJ 132, 2206

[2007] Bennett, D.P., Anderson, J.-P., Beaulieu, I. et al. 2007, NASA/NSF ExoPlanet Task Force White Paper, astro-ph/0502382

[2006a] Berton, A., Feldt, M., Gratton, R.G., Henning, Th. 2006, *The Scientific Requirements for Extremely Large Telscopes*, Whitelock, P.A., Dennefeld, M., Leibundgut, B. (eds.), Proc. of the IAUS 232, 339

[2006b] Berton, A., Gratton, R.G., Feldt, M. et al. 2006, PASP 118, 1144

[2004] Biller, B.A., Close, L.M., Lenzen, R. et al. 2004, SPIE 5490, 389

[2006] Biller, B.A., Kasper, M., Close, L.M., Brandner, W., & Kellner, S. 2006, ApJ 641, L141

[2007] Biller, B., Close, L., Masciadri, E. et al. 2007, ApJS 173, 143

[2003] Blanc, A., Fusco, T., Hartung, M. et al. 2003, A&A 399, 373

[2000] Bodenheimer, P., Hubickyj, O., & Lissauer, J.J. 2000, Icarus 143, 2

[2004] Bond, I.A., Udalski, A., Jaroszynski, M. et al. 2004, ApJ 606, L155

[2004] Bonnet, H., Abuter, R., Baker, A. et al. 2004, The ESO Messenger 117, 17

[2003] Borde, P.J., Rouan, D., & Leger, A. 2003, A&A 405, 1137

[1998] Boss, A. 1998, ApJ 503, 923

[2003] Bouy, H., Brandner, W., Martín, E.L. et al. 2003, AJ 126, 1526

[1995] Brandner, W., Bouvier, J., Grebel, E. et al. 1995, A&A 298, 818

[1997] Brandner, W., Alcalá, J.M., Frink, S., Kunkel, M. 1997, ESO – The Messenger 89, 37

[2000] Brandner, W., Zinnecker, H., Alcalá, J.M. et al. 2000, AJ 120, 950

[2004] Brandner, W. et al. 2004, CONICA SDI Comissioning report, Doc. No. VLT-TRE-ESO-14200 (Garching: ESO)

[1584] Bruno, G. 1584, *De l'Infinito Universo et Mondi*

[2004] Burgasser, A.J., Kirkpatrick, J.D., McGovern, M.R. et al. 2004, ApJ 604, 827

[1997] Burrows, A., Marley, M., Hubbard, W. et al. 1997, ApJ 491, 856

[2003] Burrows, A., Sudarsky, & D., Lunine, J.I. 2003, ApJ 596, 587

[2006a] Butler, R.P., Wright, J.T., Marcy, G.W. et al. 2006, ApJ 646, 505

[2006b] Butler, P.R., Johnson, J.A., Marcy, G.W. 2006, PASP 118, 1685

[2007] Caballero, J.A., Bejar, V.J.S, Rebolo, R. et al. 2007, A&A 470, 903

[2006] Cash, W. 2006, Nature 442, 51

[2000] Chabrier, G., Baraffe, I., Allard, F., & Hauschildt, P.H. 2000, ApJ 542, L119

[2005] Chabrier, G., Baraffe, I., Allard, F., & Hauschildt, P.H. 2005, *Review on low-mass stars and brown dwarfs*, in: ASP Conference Proceedings, eds D. Valls-Gabaud & M. Chavez

[2007] Chabrier, G., Baraffe, I., Selsis, F. et al. 2007, *Gaseous planets, protostars, and young brown dwarfs: Birth and fate*, in: PPV Conference Proceedings, eds B. Reipurth, D. Jewitt, & K. Keil

[2000] Charbonneau, D., Brown, T.M., Latham, D.W., & Mayor, M. 2000, ApJ 529, 45

[2002] Charbonneau, D., Brown, T.M., Noyes, R.W., & Gilliland, R.L. 2002, ApJ 568, 377

[2005] Charbonneau, D., Allen, L.E., Megeath, S.T. et al. 2005, ApJ 626, 523

[2004] Chauvin, G., Lagrange, A.-M., Dumas, C. et al. 2004, A&A 425, L29

[2005] Chauvin, G., Lagrange, A.-M., Dumas, C. et al. 2005, A&A 438, L25

[2005] Close, L.M., Lenzen, R., Guirado, J.C. et al. 2005, Nature 433, 286

[2007] Close, L.M., Zuckerman, B., Song, I. et al. 2007, ApJ 660, 1492

[1999] Collier Cameron, A., Walter, F.M., Vilhu, O. et al. 1999, MNRAS 308, 493

[2000] Copi, C.J., Starkman, G.D. 2000, ApJ 532, 581

[1999] Cornish, N.J. 1999, *The Lagrange Points*, `http://www.physics.montana.edu/faculty/cornish/lagrange.pdf`

[2005] Cushing, M.C., Rayner, J.T., & Vacca, W.D. 2005, ApJ 623, 1115

[2001] Cutispoto, G., Messina, S., Rodonò, M. 2001, A&A 367, 910

[1997a] D'Antona, F., Mazzitelli, I.: http://www.mporzio.astro.it/ dantona/prems.html

[1997b] D'Antona, F., Mazzitelli, I. 1997, *Evolution of low mass stars*, in: Cool stars in clusters and associations, eds R. Pallavicini & G. Micela, Mem.S.A.It, 68, n.4

[2003] Decin, G., Dominik, C., Waters, L.B.F.M., & Waelkens, C. 2003, ApJ 598, 636

[2006] Deming, D., Harrington, J., Seager, S., & Richardson, L.J. 2006, ApJ 644, 560

[2004] Di Folco, E., Thevenin, F., Kervella, P. et al. 2004, A&A 426, 601

[2001] Devillard, N. 2001, ESO C Library for an Image Processing Software Environment (eclipse), in ADASS X, ASP Conf.Ser.Vol.238, eds. F.R. Harnden, F.A. Primini, H.E. Payne, p. 525

[2006] Dohlen, K., Beuzit, J.-L., Feldt, M. et al. 2006, SPIE 6269, 24

[2002] Dommanget, J., Nys, O. 2002, Observations et Travaux 54, 5

[2000] Douglass, G.G., Mason, B.D., Rafferty, T.J., Holdenried, E.R., Germain, M.E. 2000, AJ 119, 3071

[1991] Duquennoy, A., Mayor, M. 1991, A&A 248, 485

[2003] Eisenhauer, F., Abuter, R., Bickert, K. et al. 2003, SPIE 4841, 1548

[2005] Fischer, D.A., & Valenti, J.A. 2005, ApJ 622, 1102

[2006] Fitzgerald, M.P., & Graham, J.R. 2006, ApJ 637, 541

[2005] Fortney, J.J., Marley, M.S., Hubickyj, O., Bodenheimer, P., Lissauer, J.J. 2005, Astron. Nachr. 326, 925

[1990] Franco, G.A.P. 1990, A&A 227, 499

[2000] Fridlund, M. 2000, *Darwin - The Infrared Space Interferometry Mission* ESA Bulletin 103, 20-25

[2003] Fuhrmann, K. 2003, Astron. Nachr. 325, 3

[2004] Fusco, T., Ageorges, N., Rousset, G. et al. 2004, SPIE 5490, 118

[2005] Fusco, T., Rousset, G., & Blanc, A. 2005, Science with Adaptive Optics, ed. W. Brandner & M. Kasper (Berlin: Springer), 103

[1987] Gatewood, G.D. 1987, AJ 94, 213

[2007] George, S.J., & Stevens, I.R. 2007, MNRAS 382, 455

[1975] Goodman, J.W. 1975, in Laser Speckle and Related Phenomena, ed. J.C. Dainty (Berlin: Springer), 9

[1992] Gould, A., & Loeb, A. 1992, ApJ 396, 104

[1998] Greaves, J.S., Holland, W.S., Moriarty-Schieven, G. et al. 1998, ApJ 506, L133

[2007] Grießmeier, J.-M., Zarka, P., & Spreeuw, H. 2007, A&A 475, 359

[2007] Grillmair, C.J., Charbonneau, D., Burrows, A. et al. 2007, ApJ 658, L115

[1997] Guirado, J.C., Reynolds, J.E., Lestrade, J.-F. et al. 1997, ApJ 490, 835

[2006] Guirado, J.C., Martií-Vidal, I., Marcaide, J.M. et al. 2006, A&A 446, 733

[2001] Haisch, K.E, Lada, C.J, & Lada. E.A. 2001, ApJ 533, 153

[2003] Hartung, M., Blanc, A., Fusco, T. et al. 2003, A&A 399, 385

[2000] Hatzes, A., Cochran, W., McArthur, B. et al. 2000, ApJ 544, L145

[2006] Henry, T. 2006 *The One Hundred Nearest Stellar Systems*, `http://www.chara.gsu.edu/RECONS/`

[2004] Hillenbrand, L.A., White, R.J. 2004, ApJ 604, 741

[2007] Hormuth, F., Brandner, W., Hippler, S., Janson, M. & Henning, Th. 2007, A&A 463, 707

[1999] Herbst, W., Shevchenko, V.S. 1999, AJ 118, 1043

[2008] Ida, S., & Lin, D.N.C. 2008, ApJ 673, 487

[1986] Innis, J.L., Thompson, K., Coates, D.W. 1986, MNRAS 223, 183

[1988] Innis, J.L., Thompson, K., Coates, D.W., Evans, T.L. 1988, MNRAS 235, 1411

[2006] Janson, M., Brandner, W., Lenzen, R. et al. 2006, A&A 453, 609

[2007a] Janson, M. 2007, PASP 119, 214

[2007b] Janson, M., Brandner, W., Henning, Th. et al. 2007, AJ 133, 2442

[2007c] Janson, M., Brandner, W., Lenzen, R. et al. 2007, A&A 462, 615

[2008] Janson, M., Brandner, W., & Henning, Th. 2007, A&A 478, 597

[2006] Jayawardhana, R., Ivanov, V.D. 2006, Science 313, 1279

[2007] Johnson, J.A., Butler, R.P., Marcy, G.W. ApJ 670, 833

[1963] Jeffers, H.M., van den Bos, W.H., Greeby, F.M. 1963, Index Catalogue of Visual Double Stars, Lick Observatory

[2007] Kasper, M., Apai, D., Janson, M., & Brandner, W. 2007, A&A 472, 321

[2005] Kellner, S. 2005, PhD thesis, Novel Adaptive Optics concepts: wavefront sensing with sodium laser guide stars at Extremely Large Telescopes and simultaneous differential imaging (Heidelberg: Combined Faculties for the Natural Sciences and for Mathematics of the University of Heidelberg)

[2008] Kennedy, G.M., & Kenyon, S.J. 2008, ApJ 673, 502

[1995] Kenyon, S.J., Hartman, L. 1995, ApJS 101, 117

[1998] Knude, J., Hog, E. 1998, A&A 338, 897

[2007] Knutson, H.A., Charbonneau, D., Allen, L.E. et al. 2007, Nature 447, 183

[2002] Konacki, M., Torres, G., Sasselov, D., & Jha, S. 2002, Nature 421, 507

[1997] Kürster, M., Schmitt, J.H.M.M., Cutispoto, G., Dennerl, K. 1997, A&A 320, 831

[2006] Lada, C. 2006, ApJ 640, L63

[2003] Lenzen, R. Hartung, M., Brandner, W. et al. 2003, SPIE 4841, 944

[2004] Lenzen, R., Close, L., Brandner, W., Biller, B., Hartung, M. 2004, SPIE 5492, 970

[1994] Lim, J., White, S.M., Nelson, G.J., Benz. A.O. 1994, ApJ 430, 332

[2005] Lopez, B., Schneider, J., Danchi, W.C. 2005, ApJ 627, 974

[2006] López-Santiago, J., Montes, D., Crespo-Chacón, I., Fernández-Figueroa, M.J. 2006, ApJ 643, 1160

[2005] Luhman, K.L., Stauffer, J.R., Mamajek, J.J. 2005, ApJ 628, L69

[2006] Luhman, K.L., Potter, D. 2006, ApJ 638, 887

[2003] Macintosh, B., Becklin, E.E., Kaisler, D., Konopacky, Q., & Zuckerman, B. 2003, ApJ 594, 538

[2006] Macintosh, B., Graham, J., Palmer, D. et al. 2006, SPIE 6272, 18

[2006] Marengo, M., Megeath, S.T., Fazio, G.G. et al. 2006, ApJ 647, 1437

[2006] Marley, M.S., Fortney, J.J., Hubickyj, O., Bodenheimer, P., & Lissauer, J.J. 2007, ApJ 655, 541

[2000] Marois, C., Doyon, R., Racine, R., & Nadeau, D. 2000, PASP 112, 91

[2005] Marois, C., Macintosh, B., Song, I., Barman, T. astro-ph/0502382

[2006] Marois, C., Lafreniere, D., Doyon, R., Macintosh, B., & Nadeau, D. 2006, ApJ 641, 556

[2008] Marois, C., Lafreniere, D., Macintosh, B., & Doyon, R. 2008, ApJ 673, 647

[1995] Martín, E.L., Brandner, W. 1995, A&A 294, 744

[2005] Masciadri, E., Mundt, R., Henning, Th., Alvarez, C., Barrado y Navascués, D. 2005, ApJ 625, 1004

[2002] Mason, B.D., Hartkopf, W.I., Urban, S.E. et al. 2002, AJ 124, 2254

[1995] Mayor, M., & Queloz, D. 1995, Nature 378, 355

[2007] McElwain, M.W., Metchev, S.A., Larkin, J.E. et al. 2007, ApJ 656, 505

[1998] Meyer, M.R., Edwards, S., Hinkle, K.H., & Strom, S.E. 1998, AAS 193, 3515

[2004] Mohanty, S., Jayawardhana, R., Basri, G. 2004, ApJ 609, 885

[2007] Mohanty, S., Jayawardhana, R., Huelamo, N., Mamajek, E. 2007, ApJ 657, 1064

[1987] Mueller, M., & Weigelt, G. 1987, A&A 175, 312

[2005] Mugrauer, M., Neuhäuser, R. 2005, Astron. Nachr. 326, 701

[1980] Mundt, R., Bastian, U. 1980, A&AS 39, 245

[1986] Murphy, D.C., Cohen, R., May, J. 1986, A&A 167, 234

[2007] Narita, N., Enya, K., Sato, B. et al. 2007, PASJ 59, 763

[2005a] Neuhäuser, R., Guenther, E., Wuchterl, G. et al. 2005a, A&A 435, L13 (N1)

[2005b] Neuhäuser, R., Guenther, E., Hauschildt, P.H. 2005b, *Direct detection of exo-planets: GQ Lupi* in: Richichi A. & Paresce F. (eds.) ESO Workshop The power of optical/IR interferometry, astro-ph/0506011

[2005] Nielsen, E.L., Close, L.M., Guirado, J.C. 2005, Astron. Nachr. 326, 1033

[2004] Nordström, B., Mayor, M., Andersen, J. et al. 2004, A&A 418, 989

[1995] Oppenheimer, B.R., Kulkarni, S.R., Matthews, K., & Nakajima, T. 1995, Science 270, 1478

[2002] Padoan, P., Nordlund, Å. 2002, ApJ 576, 870

[2004] Padoan, P., Nordlund, Å. 2004, ApJ 617, 559

[1981] Pakull, M.W. 1981, A&A 104, 33

[1997] Perryman, M.A.C, Lindegreen, L., Kovalevsky, J. et al. 1997, A&A 323, L49

[2001] Perryman, M.A.C, de Boer, K., Gilmore, G. et al. 2001, A&A 369, 339

[1996] Pollack, J.B., Hubickyj, O., Bodenheimer, P. et al. 1996, Icarus 124, 62

[2007] Pont, F., Moutou, R.L., Gilliland, C. et al. 2007, A&A 476, 1347

[2000a] Queloz, D., Eggenberger, A., Mayor, M. et al. 2000, A&A 359, L13

[2000b] Queloz, D., Mayor, M., Weber, L. et al. 2000, A&A 354, 99

[2006] Quillen, A.C. 2006, MNRAS 372, 14

[1999] Racine, R., Walker, G.H., Nadeau, D., Doyon, R., Marois, C. 1999, PASP 111, 587

[2005] Rafikov, R.R. 2005, ApJ 621, L69

[2006a] Reffert, S., Quirrenbach, A., Mitchell, D.S. et al. 2006, ApJ 652, 661

[2006b] Reffert, S., Segrasan, D., Launhardt, R. et al. 2006, SPIE 6268, 132

[2007] Richardson, L.J., Deming, D., Horning, K., Seager, S., & Harrington, J. 2007, Nature 445, 892

[2005] Rivera, E.J., Lissauer, J.J., Butler, R.P. et al. 2005, ApJ 634, 625

[1996] Rosenthal, E.D., Gurwell, M.A. & Ho, P.T.P. 1996, Nature 384, 243

[1955] Rossiter, R.A. 1955, Catalogue of Southern Double Stars, Pub. of the Obs. of the Univ. of Michigan

[2000] Rouan, D., Riaud, D., Boccaletti, A., Clenet, Y., & Labeyrie, A. 2000, PASP 112, 1479

[2003] Rousset, G., Lacombe, F., Puget, P. et al. 2003, SPIE 4839, 140

[1983] Rucinski, S.M. 1983, A&AS 52, 281

[1985] Rucinski, S.M. 1985, MNRAS 215, 591

[2005] Saffe, C., Gomez, M., & Chavero, C. 2005, A&A 443, 609

[2003] Sanz-Forcada, J., Maggio, A., Micela, G. 2003, A&A 408, 1087

[2005] Schindhelm, E., Cash, W., Seager, S. 2005, SPIE 5905, 455

[1998] Schmitt, J.H.M.M., Cutispoto, G., Krautter, J. 1998, ApJ 500, L25

[2008] Schneider, J. 2008, *The Extrasolar Planets Encyclopaedia*, `http://exoplanet.eu`

[2006] Scholz, A., Jayawardhana, R., & Wood, K. 2006, ApJ 645, 1498

[2005] Scholz, R.-D., LoCurto, G., Mendez, R.A. et al. 2005, A&A 439, 1127

[2007] Seager, S., Kuchner, M., Hier-Majumder, C.A., & Militzer, B. 2007, ApJ 669, 1279

[2007] Seifahrt, A., Neuhäuser, R., Hauschildt, P.H. 2007, A&A 463, 309

[2008] Setiawan, J., Henning, Th., Launhardt, R. et al. 2008, Nature 451, 38

[2000] Siess, L., Dufour, E., Forestini, M. 2000, A&A 358, 593

[2007] Silvotti, R., Schuh, S., Janulis, R. et al. 2007, Nature 449, 189

[2002] Sivaramakrishnan, A., Lloyd, J.P., Hodge, P.E., & Macintosh, B.A. 2002, ApJ 581, L59

[2000] Song, I., Caillault, J.-P., Barrado y Navascues, D., Stauffer, J.R., Randich, S. 2000, ApJ 533, L41

[2002] Sparks, W., & Ford, H.C. 2002, ApJ 578, 543

[1995] Steele, I.A., Jameson, R.F. 1995, MNRAS 272, 630

[1998] Stauffer, J.R., Schild, R., Barrado y Navascués, D. et al. 1998, ApJ 504, 805

[2008] Swain, M., Akeson, R.L., Bouwman, J., Lawler, S., & Beichman, C. 2008, ApJ accepted

[1996] Tachihara, K., Dobashi, K., Mizuno, A., Ogawa, H., Fukui, Y. 1996, PASJ 48, 489

[2001] Takeuchi, T., & Artymowicz, P. 2001, ApJ 557, 990

[1994] Tessier, E., Bouvier, J., Beuzit, J.-L., Brandner, W. 1994, ESO - The Messenger 78, 35

[2007] Thatte, N., Abuter, R., Tecza, M. et al. 2007, MNRAS 378, 1229

[2007] Thies, I., & Kroupa, P. 2007, ApJ 671, 767

[2007] Tinetti, G., Vidal-Madjar, A., Liang, M.-C. et al. 2007, Nature, 448, 169

[2001] Tinney, C.G., Butler, R.P., Marcy, G.W. et al. 2001, ApJ 551, 507

[2006] Traub, W., Levine, M., Shaklan, S. et al. 2006, SPIE 6268, 26

[2007] Trauger, J., & Traub, W. 2007, Nature 446, 771

[2005] Udalski, A., Jaroszynski, M., Paczynksi, B. et al. 2005, ApJ 628, 109

[2007] Udry, S., Bonfils, X., Delfosse, X. et al. 2007, A&A 469, 43

[2005] Umbreit, S., Burkert, A., Henning, Th., Mikkola, S., & Spurzem, R. 2005, ApJ 623, 940

[2008] Unwin, S.C., Shao, M., Tanner, A.M. et al. 2008, PASP submitted

[2003] Vanderbei, R.J., Spergel, D.N., Kasdin, N.J. 2003, ApJ 599, 686

[2007] Vanderbei, R.J., Cady, E., Kasdin, N.J. 2007, ApJ 665, 794

[1993] van Dessel, E., Sinachopoulos, D. 1993, A&AS 100, 517

[2003] Vidal-Madjar, A., Lecavelier des Etangs, A., Desert, J.-M. 2003, Nature 422, 143

[1987] Vilhu, O., Gustafsson, B., Edvardsson, B. 1987, ApJ 320, 850

[2004] Walkowicz, L.M., Hawley, S.L., West, A.A. 2004, PASP 116, 1105

[1998] Wichmann, R., Bastian, U., Krautter, J., Jankovics, I., Rucinski, S.M. 1998, MNRAS 301, L39

[1999] Wielen, R., Dettbarn, C., Jahreiß, H., Lenhardt, H., & Schwan, H. 1999, A&A 346, 675

[2007] Wolf, S., Moro-Martin, A., & D'Angelo, G. 2007, P&SS 55, 569

[1992] Wolsczcan, A., & Frail, D.A. 1992, Nature 355, 145

[2003] Wuchterl, G., Tscharnuter, W.M. 2003, A&A 398, 1081

[2007] Zarka, P. 2007, P&SS 55, 598

[2004] Zuckerman, B., Song, I., Bessell, M.S. 2004, ApJ 613, L65